



MSc Environmental Pathways for Sustainable Energy Systems - SELECT

MSc Thesis

Numerical simulation of two dimensional incompressible laminar flow over square cylinder

Author: Khalid Mohamed Mohamed Bahgat Elserfy

Supervisors: Assensi Oliva

Session: August 2015



Escola d'Enginyeria de Terrassa

UNIVERSITAT POLITÈCNICA DE CATALUNYA

MSc SELECT is a cooperation between

KTH-Royal Institute of Technology, Sweden | Aalto University, Finland | Universitat Politècnica de Catalunya, Spain |
Eindhoven University of Technology, Netherlands | Politecnico di Torino, Italy | AGH University of Science and Technology,
Poland | Instituto Superior Técnico, Portugal

Abstract

The aim of the current work is to simulate the laminar flow over square cylinder by developing numerical code using C++ programing language. The findings of this simulation are streamlines and isotherm pattern and global quantities like; lift force coefficient, Drag force coefficient, recirculation length, and Nusselt number. Flow over square cylinder is an important research topic in many engineering fields due to its numerous applications such as building aerodynamics, cooling of electronic component and compact heat exchangers. The thesis is divided into 6 chapters. The objectives and scope of the work is explained in chapter1. In chapter 2, the governing equation and the assumption used to simplify these equations are discussed. Discretization of the domain and the governing equation will be carried out in chapter 3. In chapter 4, the algorithm for pressure velocity coupling (fractional step Method), linear solver used for solving system of linear equations and different boundary conditions are discussed. The developed numerical code is verified in chapter 5 using Method of Manufactured Solution (MMS) and comparing code solution to high accurate Benchmark solution of the Driven cavity and differential heated square cavity. Finally in chapter 6, the simulation of laminar flow over square cylinder is explained, in which the effect of Reynolds number and effect of blockage ratio are investigated. Also tandem arrangement for two square cylinder and effect of adding gravity term using Boussinesq approximation for this arrangement are studied. It is concluded that, flow patterns, drag, lift coefficient, and strouhal number are affected by changing Reynolds number and blockage number. In case of tandem arrangement, downstream cylinder has different drag, lift, and Nusselt number from upstream cylinder. Moreover adding buoyancy affect different calculated parameter especially lift coefficient.

Acknowledgement

I would like to express my appreciation to my supervisor prof. Dr Assensi Oliva for his supervision and giving me the opportunity to conduct my master thesis in Heat and Mass Transfer Technological Center (CTTC). Also I would like to thank prof. Dr Carlos Segarra for his support in learning the basics of computational fluid dynamics and his guidance throughout my thesis. Thanks to Dr Xavi Trias for his session for discussing CFD. I want also to thank Dr Hamdi Kessentini for his support. Special thanks to Jorge Chiva for his great efforts in teaching me C++ programming language and helping me in solving programing errors. Thanks to Jordi Muela for his guidance.

I would to express my gratefulness to Erasmus Mundus cooperation for awarding me SELECT master scholarship. Also I would like to thank program coordinators; Thomas Nordgreen in KTH university, Dione Noort in TU/e and Cesar Valderrama in UPC for their efforts in organizing the program and seminar sessions.

I would like to thank the teaching staff at Mechanical department at Alexandria faculty of Engineering for their support during my undergraduate studies.

Finally, I would like thank my family for their encouragement and support during my entire life.

Contents

1	Introduction.....	1
1.1	Objective.....	1
1.2	Scope	1
1.3	Justification.....	1
2	Governing equation	3
2.1	Introduction.....	3
2.2	Hypotheses.....	3
2.3	Mass conservation equation	3
2.4	Conservation of linear momentum	4
2.5	Conservation of Energy equation	6
2.6	General transport equation	8
3	Finite Volume Method Discretization.....	9
3.1	Domain discretization.....	9
3.1.1	Mesh.....	9
3.1.2	Grid arrangement.....	10
3.1.3	Staggered grid	11
3.2	Discretization of transport equation	12
3.2.1	Surface Integrals and Volume Integrals approximation	12
3.2.2	Discretization of diffusion term	13

3.2.3	Discretization of convective term	14
3.2.4	Discretization of source term	18
3.2.5	Temporal discretization	19
4	Algorithm for pressure velocity coupling (fractional step method).....	21
4.1	Derivation	21
4.2	Solvers for discretized equations	24
4.2.1	Gauss-Sedial	24
4.2.2	Tri-diagonal matrix algorithm	24
4.2.3	Line by line TDMA in 2D dimensional problem	25
4.3	Boundary conditions.....	27
4.3.1	Types of boundary conditions.....	28
4.4	Determination of time step.....	29
4.5	Solving Algorithm	30
5	Software verification.....	34
5.1	Method of Manufactured Solution.....	35
5.1.1	Verification of coupling of the steady continuity and momentum equation, with staggered mesh and unknown field by MMS.....	36
5.2	Reference cases	40
5.2.1	Driven square cavity.....	40
5.2.2	Differentially heated square cavity.....	49
6	Case study: laminar flow around square cylinder	59

6.1	The effect of changing Reynolds number for fixed blockage ratio	60
6.1.1	Geometry of the computational domain and mesh	60
6.1.2	Boundary conditions	62
6.1.3	Results.....	63
6.2	The effect of blockage ratio on dimensionless force coefficient and heat transfer .	75
6.2.1	Computation domain and boundary conditions	75
6.2.2	Results.....	76
6.3	Dimensionless force coefficient and heat transfer for two square cylinder placed in tandem arrangement	85
6.3.1	Computational domain and boundary conditions.....	85
6.3.2	Results.....	86
6.4	Comparison between the effects of mixed convection compared to forced convection on heat transfer and dimensionless force coefficient for two square cylinder in tandem arrangement.	91
6.4.1	Computational domain and boundary conditions.....	91
6.4.2	Results.....	91
7	Conclusion.....	100
	Reference	101
	Appendix.....	103
A.1	Streamlines for different Reynolds number for square cylinder with blockage ratio of 12.5%	103
	A.2 Result for effect of blockage ratio using coarser mesh	107

List of figures

Figure 3.1: uniform and nonuniform structured mesh	10
Figure 3.2: unstructured three-noded triangle mesh[3]	10
Figure 3.3: collocated grid[5]	11
Figure 3.4: staggered mesh.....	11
Figure 3.5: control volumes for staggered grid for mass conservation, momentum equation in x-direction and momentum equation in y-direction	12
Figure 3.6: Control volume for transported quantity \emptyset	14
Figure 3.7 : u control volume for momentum equation in x-direction[6].....	15
Figure 3.8: Central scheme	16
Figure 3.9: Upwind scheme for $F>0$ and $F<0$	16
Figure 3.10: Normalized variables[7]	18
Figure 3.11: control volume for momentum equation in x-direction.....	19
Figure 4.1: predictor velocity decomposition [10]	21
Figure 4.2: pressure control volume.	23
Figure 4.3: TDMA line by line[8]	26
Figure 4.4: Gauss-Sedial Algorithm.....	27
Figure 4.5: Solver algorithm	33
Figure 5.1:Difference between model verification and validation[16].....	34
Figure 5.2: verification process.....	35

Figure 5.3: Driven cavity problem description.....	41
Figure 5.4: Comparison of u velocity with Benchmark solution for Re=400 using different numerical scheme on mesh 50*50	42
Figure 5.5: Comparison of v velocity with Benchmark solution for Re=400 using different numerical scheme on mesh 50*50	42
Figure 5.6: Comparison of u velocity with Benchmark solution for Re=100 (mesh 50*50) ...	43
Figure 5.7: Comparison of v velocity with Benchmark solution for Re=100 (mesh 50*50) ...	43
Figure 5.8: Comparison of u velocity with Benchmark solution for Re=3200(mesh 100*100)	44
Figure 5.9: Comparison of v velocity with Benchmark solution for Re=3200(mesh 100*100)	44
Figure 5.10: Comparison of u velocity with Benchmark solution for Re=5000(mesh 160*160)	45
Figure 5.11: Comparison of v velocity with Benchmark solution for Re=5000(mesh 160*160)	45
Figure 5.12: Comparison of u velocity with Benchmark solution for Re=7500(mesh 160*160)	46
Figure 5.13: Comparison of v velocity with Benchmark solution for Re=7500(mesh 160*160)	46
Figure 5.14: Streamlines for Re=100(mesh 50*50)	47
Figure 5.15: Streamlines for Re=400(mesh 50*50)	47
Figure 5.16: Streamlines for Re=3200(mesh 100*100)	48
Figure 5.17: Streamlines for Re=5000(mesh160*160)	48
Figure 5.18: Streamlines for Re=7500(mesh160*160)	49

Figure 5.19: Problem description.....	50
Figure 5.20: contours of (a) temperature, (b) streamline function, (c) u velocity,(d) v velocity at $\text{Ra}=10^3$	52
Figure 5.21:contours of (a) temperature, (b) streamline function, (c) u velocity,(d) v velocity at $\text{Ra}=10^4$	54
Figure 5.22:contours of (a) temperature, (b) streamline function, (c) u velocity,(d) v velocity at $\text{Ra}=10^5$	55
Figure 5.23:contours of (a) temperature, (b) streamline function, (c) u velocity,(d) v velocity at $\text{Ra}=10^6$	56
Figure 6.1: Laminar flow over square cylinder	59
Figure 6.2: Geometry of computational domain[19]	60
Figure 6.3: Mesh used in square cylinder case.....	61
Figure 6.4: Definition of the recirculation length[20]	64
Figure 6.5: Velocity in x-direction contour for; (a) $\text{Re}=1$, and (b) $\text{Re}=30$	66
Figure 6.6: Velocity in y-direction contour for; (a) $\text{Re}=1$, and (b) $\text{Re}=30$	66
Figure 6.7: Pressure contours for; (a) $\text{Re}=1$, and (b) $\text{Re}=30$	66
Figure 6.8: Streamlines around square cylinder for (a) $\text{Re}=1$; (b) $\text{Re}=30$	67
Figure 6.9: Streamlines around square cylinder for (a) $\text{Re}=1$; (b) $\text{Re}=30$ presented by Breuer [19].....	68
Figure 6.10: comparison of calculated recirculation length with previous work[19].....	68
Figure 6.11: Drag coefficient: (a) calculated in present work (b) calculated by Breuer [19] ..	69
Figure 6.12:Velocity in x-direction contour for; (a) $\text{Re}=65$, and (b) $\text{Re}=200$	70
Figure 6.13: Velocity in y-direction contour for ;(a) $\text{Re}=65$, and (b) $\text{Re}=200$	70

Figure 6.14: Pressure contours for; (a) Re=65, and (b) Re=200.....	70
Figure 6.15: Streamlines around square cylinder for Re=65.....	71
Figure 6.16: Streamlines around square cylinder for Re=200 (a) present solution (b)Breuer [19]	71
Figure 6.17: Time averaged drag coefficient for different Reynolds number.....	72
Figure 6.18: Variation of the drag coefficient $\max(C_d) - \min(C_d)$	73
Figure 6.19: Variation of the lift coefficient $\max(Cl) - \min(Cl)$	73
Figure 6.20: Strouhal number for different Reynolds number for unsteady regime	74
Figure 6.21: Computational domain [23].....	76
Figure 6.22: Streamlines for blockage ratio (10%-30%) for different Reynolds number (50, 100, and 150)	77
Figure 6.23: Streamlines for blockage ratio (40%, 30%) for different Reynolds number (50, 100, and 150)	78
Figure 6.24: Isotherm contours for Re=150 for different blockage ratio a) 10% (b) 20% (c) 30%	79
Figure 6.25: Isotherm contours for Re=150 for different blockage ratio a) 40% (b) 50%.....	80
Figure 6.26: Drag coefficient versus blockage ratio at Re=50,100,150	81
Figure 6.27:Strouhal number versus blockage ratio at Re=50,100,150	81
Figure 6.28: Nusselt number for front side of square versus blockage ratio for Re=50, 100, and150	82
Figure 6.29: Nusselt number for rear side of square versus blockage ratio for Re=50, 100, and150	83
Figure 6.30: Nusselt number for top/bottom side of square versus blockage ratio for Re=50, 100, and150.....	83

Figure 6.31: Square cylinder average Nusselt number versus blockage ratio for Re=50, 100, and150.....	84
Figure 6.32: Computational domain[24].....	85
Figure 6.33:Streamlines for two square in tandem arrangement for : (a) Re=5, (b) Re=10,(c) Re=15 ,(d) Re=20 , (e) Re=25 ,and (f) Re=30	86
Figure 6.34: Temperature contours for two square in tandem arrangement for: (a) Re=5, (b) Re=10, (c) Re=15, (d) Re=20, (e) Re=25, and (f) Re=30	87
Figure 6.35: Drag coefficient for upstream and downstream square cylinder versus Reynolds number.....	88
Figure 6.36: Recirculation length for upstream and downstream square cylinder versus Reynolds number.....	89
Figure 6.37: Average Nusselt for upstream and downstream square cylinder versus Reynolds number.....	89
Figure 6.38: Computational domain[25].....	91
Figure 6.39: Streamlines for Reynolds number Re= 1, 10, 20, and30 for forced convection (Ri=0) and mixed convection (Ri=1)	92
Figure 6.40: Drag coefficient for upstream and downstream cylinder versus Reynolds number for forced convection (Ri=0) and mixed convection (Ri=1)	93
Figure 6.41: Temperature contours for Reynolds number Re= 1, 10, 20, and30 for forced convection (Ri=0) and mixed convection (Ri=1)	94
Figure 6.42: lift coefficient for upstream and downstream cylinder versus Reynolds number for forced convection (Ri=0) and mixed convection (Ri=1)	95
Figure 6.43: Average Nusselt number for upstream and downstream cylinder versus Reynolds number for forced convection (Ri=0) and mixed convection (Ri=1)	96
Figure 6.44: Front face Nusselt number for upstream and downstream cylinder versus Reynolds number for forced convection (Ri=0) and mixed convection (Ri=1)..	97

Figure 6.45: Rear face Nusselt number for upstream and downstream cylinder versus Reynolds number for forced convection ($Ri=0$) and mixed convection ($Ri=1$) .97

Figure 6.46: Top face Nusselt number for upstream and downstream cylinder versus Reynolds number for forced convection ($Ri=0$) and mixed convection ($Ri=1$)98

Figure 6.47: Bottom face Nusselt number for upstream and downstream cylinder versus Reynolds number for forced convection ($Ri=0$) and mixed convection ($Ri=1$) .98

List of Tables

Table 2.1: Parameters to be replace in transport equation in order to reproduce governing equation[2].....	8
Table 5.1: Table of the error convergence for u	38
Table 5.2: Table of the error convergence for v	38
Table 5.3: Table of the error convergence for u and v	39
Table 5.4: comparison between Benchmark solution and code solution at $Ra=10^3$	51
Table 5.5: Comparison between Benchmark solution and code solution at $Ra=10^4$	53
Table 5.6: Comparison between Benchmark solution and code solution at $Ra=10^5$	53
Table 5.7: Comparison between Benchmark solution and code solution at $Ra=10^6$	57

1 Introduction

1.1 Objective

The objective of this project is to develop numerical code using C++ programming language to simulate laminar flow of incompressible fluid over square cylinder placed in a channel. Flow over bluff body is an important research topic in many engineering fields due to its numerous applications such as building aerodynamics, cooling of electronic component and compact heat exchangers. Flow over bluff body is flow in which flow separates from large section of the body surface under normal circumstances, creating wake region downstream. Simulation of such flow determines the forces acting on square cylinder, vortex shedding frequency and heat transfer rates.

1.2 Scope

The study will take the following consideration

- The Navier stokes equation will be solved using some simplifying hypothesis.
- The flow is incompressible.
- The flow has constant physical properties.
- Newtonian fluids are considered in this study.
- The domain and geometries are 2D.
- Code is verified with reference cases (driven cavity and differentially heated cavity).
- Final case of laminar flow over square cylinder is implemented.

1.3 Justification

The implementation of computational fluid dynamics code are nowadays essential in many industrial application like automotive industry and aircraft industry , in which this tool is used to simulate the flow over car or aircraft ,so that the final design is optimized to have the least drag and lowest energy consumption. CFD is powerful tool that enables companies to test their product with low expenses compared to the experimental testing that consumes a lot of time and money. Moreover, nowadays with the growing computational power of computers, using of CFD in companies becomes more viable and more cost effective. Also from

Chapter 1|Introduction

educational point of view, implementation of self-built CFD code gives better understanding of Navier-stokes equation and different physical phenomena.

2 Governing equation

2.1 Introduction

This chapter presents the governing equation that will be used to describe the fluid flow and the heat transfer in mathematical form. These governing equations are the conservation of mass, conservation of linear momentum (Newton's second law) and conservation of energy (first law of thermodynamics). Some hypothesis will be used to simplify these equations .After implementing these hypotheses these equation will be discretized in the next chapter.

2.2 Hypotheses

The following hypotheses are used to simplify the governing equation:

- Incompressible fluid.
- Two dimensional.
- Newtonian fluid.
- Constant physical properties (density, specific heat, conductivity and viscosity).
- Boussinesq approximation to model natural convection.
- Radiation is neglected.

2.3 Mass conservation equation

The mass conservation equation is derived by equating the rate of increase of mass inside fluid element by the net rate of flow of mass into fluid element which is presented as follow.

$$\frac{\partial \rho}{\partial t} + \nabla \cdot (\rho \mathbf{u}) = 0 \quad (2.1)$$

Where;

ρ : Fluid density

\mathbf{u} : Velocity vector

Eq.(2.1) is the unsteady, three dimensional conservation of mass equation at appoint in incompressible fluid. The first term represent the rate of change in time of mass per unit volume. The second term represents the mass flux across fluid element boundaries (convective term).

For two dimensional incompressible flows, Eq.(2.1) is further simplified as shown in Eq.(2.2).

$$\nabla \cdot \mathbf{u} = \frac{du}{dx} + \frac{\partial v}{\partial y} = 0 \quad (2.2)$$

In integral form the continuity equation will be as follow;

$$\int_S \mathbf{u} \cdot \mathbf{n} \, ds = 0 \quad (2.3)$$

2.4 Conservation of linear momentum

Conservation of momentum states that the rate of change of linear momentum must be equal to the net forces acting on fluid particle as shown in Eq.(2.4) . Forces acting on the fluid particle are divided into body forces and surface force. Body force includes centrifugal, gravity and buoyancy force. Surface force includes viscous and pressure force.

$$\frac{D(\rho \mathbf{u})}{Dt} = \rho \mathbf{g} + \nabla \cdot \boldsymbol{\sigma} \quad (2.4)$$

Where

$\boldsymbol{\sigma}$: stress tensor.

\mathbf{g} : Gravity

The stress tensor is often resolved into an isotropic part (independent of direction) and a deviatoric part. In a Newtonian fluid the viscous stresses are proportional to the rates of deformation. The two-dimensional form of Newton's law of viscosity involves constant of proportionality, which is (dynamic) viscosity (μ).

$$\boldsymbol{\sigma} = -P \mathbf{I} + \boldsymbol{\tau} \quad (2.5)$$

$$\boldsymbol{\sigma} = \begin{pmatrix} -p + \tau_{xx} & \tau_{xy} \\ \tau_{yx} & -p + \tau_{yy} \end{pmatrix} = \begin{pmatrix} -p + 2\mu \frac{\partial u}{\partial x} & \mu \left(\frac{\partial u}{\partial y} + \frac{\partial v}{\partial x} \right) \\ \mu \left(\frac{\partial u}{\partial y} + \frac{\partial v}{\partial x} \right) & -p + 2\mu \frac{\partial v}{\partial y} \end{pmatrix} \quad (2.6)$$

Where

P: pressure.

I: identity matrix.

Chapter 2|Governing equation

τ : Shear stress tensor.

μ : Dynamic viscosity

After substituting the stress tensor in Eq.(2.4) and using Boussinesq term for the body force in y-direction as shown in Eq.(2.7). The momentum equation is as follow.

$$\rho = \rho_0(1 + \beta(T - T_0)) \quad (2.7)$$

$$\rho \frac{\partial u}{\partial t} + \nabla(\rho uu) = -\frac{\partial p}{\partial x} + \frac{\partial}{\partial x} \left(2\mu \frac{\partial u}{\partial x} \right) + \frac{\partial}{\partial y} \left(\mu \left(\frac{\partial u}{\partial y} + \frac{\partial v}{\partial x} \right) \right) \quad (2.8)$$

$$\rho \frac{\partial u}{\partial t} + \nabla(\rho uu) = -\frac{\partial p}{\partial x} + \mu \frac{\partial}{\partial x} \left(\frac{\partial u}{\partial x} \right) + \mu \frac{\partial}{\partial y} \left(\frac{\partial u}{\partial y} \right) + \mu \frac{d}{dx} \left(\frac{\partial u}{\partial x} + \frac{\partial v}{\partial y} \right) \quad (2.9)$$

For incompressible flow, $\frac{\partial u}{\partial x} + \frac{\partial v}{\partial y} = 0$, The momentum equation x and y-direction will be as follows

$$\rho \frac{\partial u}{\partial t} + \nabla(\rho uu) = -\frac{\partial p}{\partial x} + \mu \frac{\partial^2 u}{\partial x^2} + \mu \frac{\partial^2 u}{\partial y^2} \quad (2.10)$$

$$\rho \frac{\partial v}{\partial t} + \nabla(\rho uv) = -\frac{\partial p}{\partial y} + \mu \frac{\partial^2 v}{\partial x^2} + \mu \frac{\partial^2 v}{\partial y^2} + \rho_0 \beta(T - T_0) g_y \quad (2.11)$$

Where;

u: Velocity vector.

u : Velocity component in x-direction

v : Velocity component in y-direction

T_0 : Reference Temperature

ρ_0 : Density at reference temperature

g_y : Gravity at y-direction

β : Thermal expansion coefficient.

Momentum equation in integral form is as follows;

$$\int_V \rho \frac{\partial u}{\partial t} dV + \int_S (\rho \mathbf{u} \cdot \mathbf{n}) \cdot \mathbf{n} ds = - \int_S p n_x ds + \int_S \mu \frac{\partial u}{\partial x} n_x ds + \int_S \mu \left(\frac{\partial u}{\partial y} \right) n_y ds \quad (2.12)$$

$$\begin{aligned} \int_V \rho \frac{\partial v}{\partial t} dV + \int_S (\rho \mathbf{u} \cdot \mathbf{n}) \cdot \mathbf{n} ds &= \\ - \int_S p n_y ds + \int_S \mu \left(\frac{\partial v}{\partial x} \right) n_x ds + \int_S \mu \frac{\partial v}{\partial y} n_y ds + \rho_0 B(T-T_0) g_y & \end{aligned} \quad (2.13)$$

2.5 Conservation of Energy equation

The energy equation is derived from the first law of thermodynamics, which states that the rate of change of energy of a fluid particle is equal to the rate of heat addition to the fluid particle plus the rate of work done on the particle.

The rate of work done on the fluid particle in the element by a surface force is equal to the product of the force and velocity component in the direction of the force.

$$Rate of work done on particle = -\nabla \cdot (p \mathbf{u}) + \nabla \cdot (\mathbf{u} \cdot \boldsymbol{\tau}) \quad (2.14)$$

The total rate of heat added to the fluid particle per unit volume due to heat flow across its boundaries. In which Fourier law of heat conduction relates the heat flux to the local temperature gradient as follows.

$$Rate of heat added to fluid particle = -\nabla \cdot q = -\nabla \cdot (-k \nabla T) \quad (2.15)$$

The energy of a fluid is defined as the sum of internal (thermal) energy i , kinetic energy $\frac{1}{2}(u^2+v^2)$ and gravitational potential energy. This definition takes the view that the fluid element is storing gravitational potential energy.

$$Rate of change energy of fluid (E) = \rho \frac{DE}{dt} = \rho \frac{D(i + 1/2(u^2 + v^2))}{Dt} \quad (2.16)$$

Energy equation will be as follow,

Chapter 2|Governing equation

$$\rho \frac{D(i + 1/2(u^2 + v^2))}{Dt} = -\nabla \cdot (p \mathbf{u}) + \nabla \cdot (\mathbf{u} \cdot \boldsymbol{\tau}) - \nabla \cdot (-k \nabla T) \quad (2.17)$$

Where

$$\nabla \cdot (\mathbf{u} \cdot \boldsymbol{\tau}) = \frac{\partial}{\partial x_j} (u_i \tau_{ij}) \quad (2.18)$$

The kinetic energy of fluid particle can be found by multiplication of the momentum equation in x-direction by velocity component u and momentum equation in y-direction by velocity component v as shown in Eq. (2.19).

$$\rho \frac{D(1/2(u^2 + v^2))}{Dt} = -\mathbf{u} \cdot \nabla p + \mathbf{u} \cdot (\nabla \cdot \boldsymbol{\tau}) \quad (2.19)$$

Where

$$\mathbf{u} \cdot (\nabla \cdot \boldsymbol{\tau}) = u_i \left(\frac{\partial \tau_{ij}}{\partial x_j} \right) \quad (2.20)$$

By subtracting Eq.(2.19) from Eq.(2.17), yields the internal energy equation[1].

$$\rho \frac{Di}{Dt} = -p (\nabla \cdot \mathbf{u}) + \nabla \mathbf{u} : \boldsymbol{\tau} + \nabla(k \nabla T) \quad (2.21)$$

Where

$\nabla \mathbf{u}$: Velocity gradient tensor

$$\nabla \mathbf{u} : \boldsymbol{\tau} = \nabla \cdot (\mathbf{u} \cdot \boldsymbol{\tau}) - \mathbf{u} \cdot (\nabla \cdot \boldsymbol{\tau}) \quad (2.22)$$

$$\nabla \mathbf{u} : \boldsymbol{\tau} = \left(\frac{\partial u_i}{\partial x_j} \right) \tau_{ij} \quad (2.23)$$

For incompressible flow ($\nabla \cdot \mathbf{u} = 0$), and the viscous heating term ($\nabla \mathbf{u} : \boldsymbol{\tau}$) is neglected. The internal energy of fluid (i) can be substituted by ($i = C T$), where C is the specific heat of fluid. These substitutions yield the temperature equation.

$$\rho C \frac{\partial T}{\partial t} + \rho C \nabla \cdot (\mathbf{u} T) = \nabla(k \nabla T) \quad (2.24)$$

In integral form the energy equation;

$$\int_V \rho C \frac{\partial T}{\partial t} dV + \int_s (\rho C \mathbf{u} \cdot \nabla T) \cdot n ds = \int_s (k \nabla T) \cdot n ds \quad (2.25)$$

2.6 General transport equation

In this section, the mass, momentum and energy equation will be summarized in convection-diffusion general transport equation, in which general variable ϕ is introduced which stands for scalar property such as: T or u. Different fluid conservation equations can be written in the following form:

$$\frac{\partial(\rho\phi)}{\partial t} + \nabla \cdot (\rho\phi\mathbf{u}) = \nabla \cdot (\Gamma \nabla \phi) + S_\phi \quad (2.26)$$

The transport equation of property ϕ clearly highlights the various transport processes: the rate of change term ($\frac{\partial(\rho\phi)}{\partial t}$), which express rate of change of the total amount of fluid property ϕ in the control volume, the convective term ($\nabla \cdot (\rho\phi\mathbf{u})$) which, expresses the flux component of property ϕ due to fluid flow, the diffusive term ($\nabla \cdot (\Gamma \nabla \phi)$) which represent net rate of increase of fluid property ϕ of the fluid element due to diffusion and the source tem (S_ϕ) which gives the rate of increase of property ϕ as a result of sources inside the fluid element. This transport equation can be expressed in integral form as follows.

$$\int_V \frac{\partial \rho\phi}{\partial t} dV + \int_s (\rho\phi\mathbf{u}) \cdot n ds = \int_s (\Gamma \nabla \phi) \cdot n ds + \int_V S_\phi dV \quad (2.27)$$

Different governing equation can be obtained by replacing fluid property ϕ , diffusion coefficient and source term $S\phi$ as shown in Table 2.1.

Equation	ϕ	Γ	S
Continuity	1	0	0
Momentum in x-direction	u	μ	$-\frac{\partial p}{\partial x}$
Momentum in y-direction	v	μ	$-\frac{\partial p}{\partial y} + \rho g \beta (T - T_0)$
Energy (constant C)	T	k/C	φ/C

Table 2.1: Parameters to be replace in transport equation in order to reproduce governing equation[2]

3 Finite Volume Method Discretization

In this chapter the discretization of the domain and the governing equation will be carried out. The purpose of any discretization is to transform a set of partial differential equations (PDEs) into a corresponding system of discrete algebraic equations (DAEs). The discretization process can be divided into two steps, namely; the discretization of the solution domain and the discretization of the governing equation.

The discretization of the solution domain produces a numerical description of the computational domain, in which space is divided into many control volumes (CVs) or cells. The governing equations discretization with the domain discretization, produces an appropriate transformation of the terms of the governing equations into a system of discrete algebraic equations that can be solved using any direct or iterative method.

3.1 Domain discretization

3.1.1 Mesh

The discretization of the computational domain is a process that divides the computational domain into many control volumes. The control volumes do not overlap, have a positive finite volume and completely fill the computational domain. There are basically two types of meshes: structured and unstructured mesh.

Structured mesh is the mesh which consists of horizontal and vertical lines that are orthogonal to each other. The intersection of these lines produce regular shapes element with four nodal corners in 2D or hexahedral shape element with eight nodal corners in 3D. If the nodal spacing is the same in each direction ($\Delta x = \Delta y = \text{constant}$), then the mesh is considered to be uniform. Mesh is nonuniform, when Δx and Δy is not the same across different nodes. Nonuniform meshes are used to create smaller grid spacing near wall or surfaces to capture steep gradients in the boundary layer [3] as shown in Figure 3.1.

In unstructured mesh, 2D domain is discretized by placing randomly placed nodes that are connected together by triangular or quadrilaterally shaped elements. The most common types of unstructured mesh are three-nodded triangles as shown in Figure 3.2 and four-nodded quadrilaterals. Generation of structured mesh requires more effort compared to structured meshes

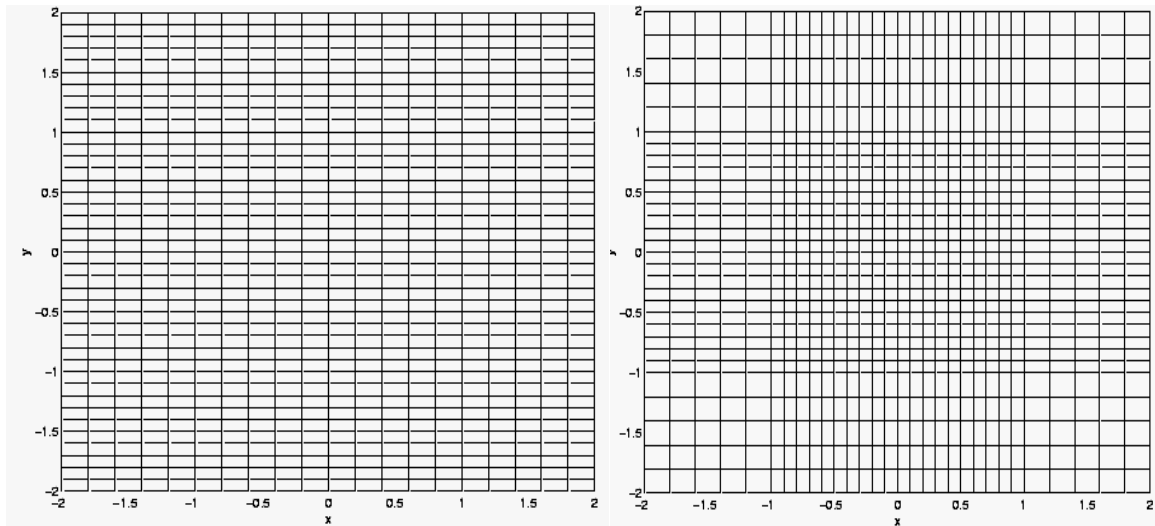


Figure 3.1: uniform and nonuniform structured mesh

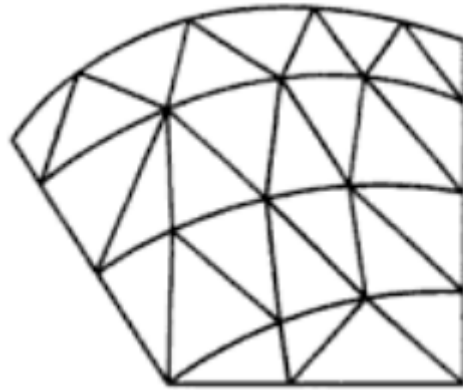


Figure 3.2: unstructured three-noded triangle mesh[3]

3.1.2 Grid arrangement

Navier-Stokes equations are coupled equations for vector fields; several variants of the arrangement of the computational nodes are possible. There are two types of grid used in CFD, a collocated grid and a staggered grid.

3.1.2.1 Collocated grid

In collocated grid, all the flow-field variables including the velocities are stored at the same set of nodal points as shown in Figure 3.3. The collocated mesh offer significant advantages as mentioned in [4]: all variables share the same location; hence there is only one set of control volumes, the convection contribution to the coefficients in the discretized equations is the

same for all variables and the collocated grids offer much simpler CFD code implementation than the staggered counterparts when the domain geometry is complex. Its disadvantages are: collocated mesh does not ensure p-u coupling which may lead to the appearance of nonphysical checkerboard pressure field.

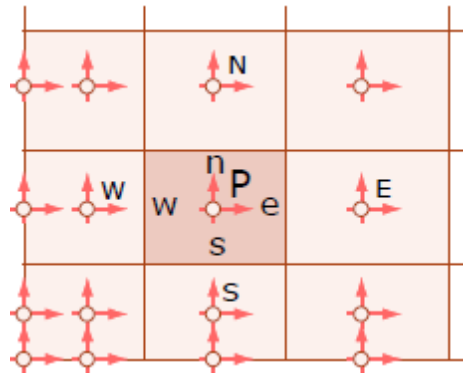


Figure 3.3: collocated grid[5]

3.1.3 Staggered grid

In staggered mesh the velocity components are stored at the control volume faces, while the rest of the variables governing the flow field such as pressure, temperature, viscosity and density are stored in the center of the control volume as shown in Figure 3.4. Advantages of staggered grid are: several terms that require interpolation in collocated mesh can be evaluated with second order accuracy without interpolation like pressure gradient term in the momentum equation and the diffusion term at the control surface of the x-momentum control volume. In staggered mesh, three control volumes are used; mass conservation and scalar quantities CV, momentum equation in x-direction CV and momentum equation in y-direction CV as shown in Figure 3.5.

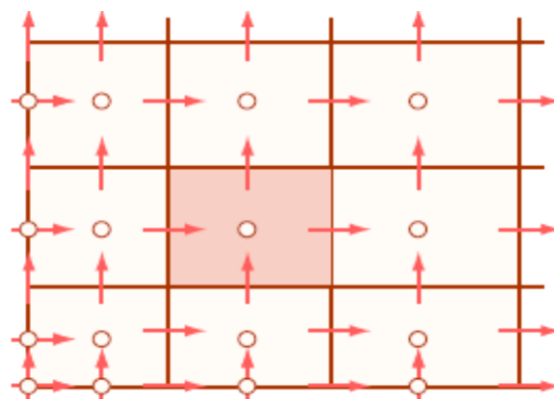


Figure 3.4: staggered mesh

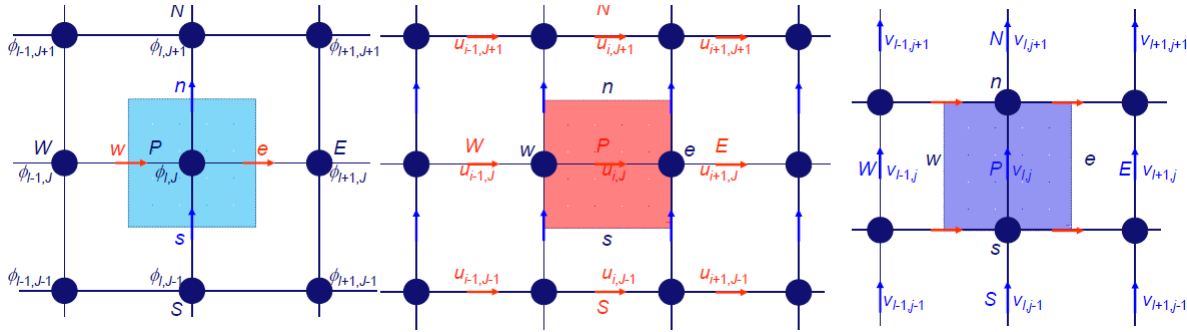


Figure 3.5: control volumes for staggered grid for mass conservation, momentum equation in x-direction and momentum equation in y-direction

3.2 Discretization of transport equation

In this section, the discretization of different term of the governing equations will be discussed in details such as; discretization's of diffusion term, convective term a, pressure term and time term. Φ is the transported quantity which can be velocity or temperature.

$$\int_V \underbrace{\frac{\partial}{\partial t} (\rho\phi) dV}_{\text{temporal term}} + \int_V \underbrace{\nabla \cdot (\rho\phi \mathbf{u}) dV}_{\text{convective term}} = \int_V \underbrace{\nabla \cdot (\Gamma \nabla \phi) dV}_{\text{diffusion term}} + \int_V \underbrace{S_\phi dV}_{\text{source term}} \quad (3.1)$$

Gauss theorem is used to decrease volume integrals to surface integral as shown in Eq.(3.2). It states that volume integral of the divergence of a vector in a region inside the volume is equal to surface integral of the outward flux normal to the surface that bounds that volume.

$$\int_V \nabla \cdot a dV = \int_S a \cdot n dS \quad (3.2)$$

By using Gauss theorem, Eq.(3.3) can be written as follows.

$$\int_V \frac{\partial \rho\phi}{\partial t} dV + \int_S (\rho\phi \mathbf{u}) \cdot n ds = \int_S (\Gamma \nabla \phi) \cdot n ds + \int_V S_\phi dV \quad (3.3)$$

3.2.1 Surface Integrals and Volume Integrals approximation

For evaluation of the surface integral, the convective ($\rho\phi\mathbf{u}$) or the diffusive flux ($\Gamma\nabla\phi$) are required everywhere on the surface, but this information is not available on the surface and

needed to be approximated in term of nodal values on the surface. To obtain approximate values for surface integral, two levels of approximation are used: approximation of the surface integral in term of variable values at one or more location at cell face, or approximation of the cell face values in term of control volume nodal values.

Different methods are used to obtain surface integral such as; midpoint, trapezoid, or Simpson's rule, the simplest rule is the midpoint which yields the following equation.

$$\int_s (\rho\phi\mathbf{u}) \cdot \mathbf{n} dS = \sum_f \int_f (\rho\mathbf{u}\phi)_f \cdot \mathbf{n} dS \approx \sum_f (\overline{\rho\mathbf{u}\phi})_f \mathbf{n}_f S_f = \sum_f (\rho\mathbf{u}\phi)_f \mathbf{n}_f S_f \quad (3.4)$$

$$\int_s (\Gamma\nabla\phi) \cdot \mathbf{n} dS = \sum_f \int_f (\Gamma\nabla\phi)_f \cdot \mathbf{n} dS \approx \sum_f (\overline{\Gamma\nabla\phi})_f \mathbf{n}_f S_f = \sum_f (\Gamma\nabla\phi)_f \mathbf{n}_f S_f \quad (3.5)$$

Similarly for obtaining the volume integral, the midpoint rule is used, which yields the following expression. Where S_p is the source term at nodal point at the center of control volume.

$$\int_V S_\phi dV = \overline{S_p} V = S_p V \quad (3.6)$$

3.2.2 Discretization of diffusion term

The discretization of the convective term in Eq.(3.3) is obtained as in Eq.(3.7).

$$\int_s (\Gamma\nabla\phi) \cdot \mathbf{n} ds = (\Gamma\nabla\phi)_e A_e - (\Gamma\nabla\phi)_w A_w + (\Gamma\nabla\phi)_n A_n - (\Gamma\nabla\phi)_s A_s \quad (3.7)$$

The gradient term $\nabla\phi$ is evaluated at the faces using central difference scheme as shown in Eq.(3.8).

$$(\nabla\phi)_e = \frac{\phi_E - \phi_p}{d_{Ep}} \quad (3.8)$$

The diffusion coefficient Γ at the control volume is found by using the harmonic mean if the diffusion coefficient is not stored in this node.

$$\Gamma_e = \frac{\Delta_{PE}}{\frac{d_{eE}}{\Gamma_e} + \frac{d_{pe}}{\Gamma_p}} \quad (3.9)$$

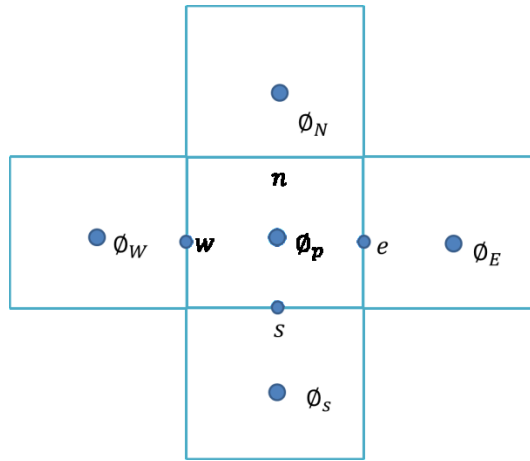


Figure 3.6: Control volume for transported quantity ϕ

3.2.3 Discretization of convective term

The discretization of the convective term in Eq.(3.3) is obtained as in Eq.(3.10).

$$\int_s (\rho \phi \mathbf{u}) \cdot \mathbf{n} ds = \sum_f (\rho \mathbf{u})_f \phi_f = (\rho \mathbf{u})_e \phi_e A_e - (\rho \mathbf{u})_w \phi_w A_w + (\rho \mathbf{u})_n \phi_n A_n - (\rho \mathbf{u})_s \phi_s A_s \quad (3.10)$$

Where, the mass flux term per unit area $(\rho \mathbf{u})_f$ is calculated as shown in the following expression for x-momentum equation in Eq.(3.11) and Eq.(3.12) . Similarly for the momentum equation in y-direction. For the energy equation no interpolation is needed for the flux term because the velocities are located on the midpoint of the faces. In order to obtain the face value of the transported quantity ϕ_f interpolation schemes are used which will be presented in the following section.

$$F_n = (\rho v)_n = \frac{(\rho v)_A A_{An} + (\rho v)_B A_{Bn}}{A_n} \quad (3.11)$$

$$F_e = (\rho u)_e = \frac{(\rho u)_E + (\rho v)_P}{2} \quad (3.12)$$

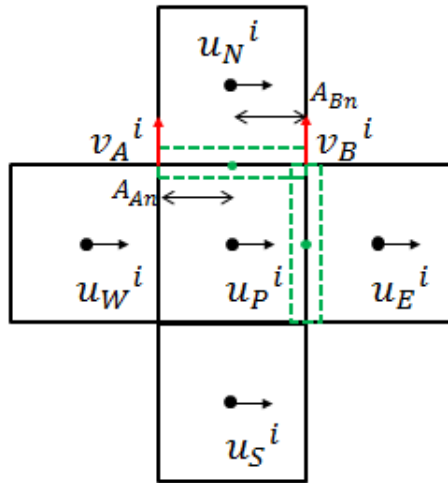


Figure 3.7 : u control volume for momentum equation in x -direction[6]

3.2.3.1 Numerical schemes

In this section different numerical schemes will be presented, which are used to determine the value of the transported quantity ϕ_f on the faces of the control volume. The values ϕ in the neighboring control volume are used to find the value of ϕ_f .

- Central scheme

In central scheme, variables are assumed to vary linearly. ϕ_f is obtained by weighted linear interpolation between the values of neighboring control volumes P and N as shown in Figure 3.8.

$$\phi_f = \phi_p \left(\frac{x_N - x_f}{x_N - x_p} \right) + \phi_N \left(\frac{x_f - x_p}{x_N - x_p} \right) \quad (3.13)$$

A special case arises in case of uniform mesh; the central scheme becomes the arithmetic average of neighboring point.

$$\phi_f = \frac{\phi_p + \phi_N}{2} \quad (3.14)$$

Central scheme is second order accuracy, but it may cause non-physical oscillations in the solution for convection dominated problems (Peclet number >2), leading to violation of the boundedness of the solution.

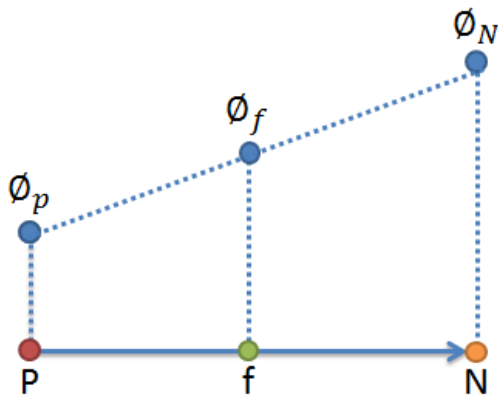


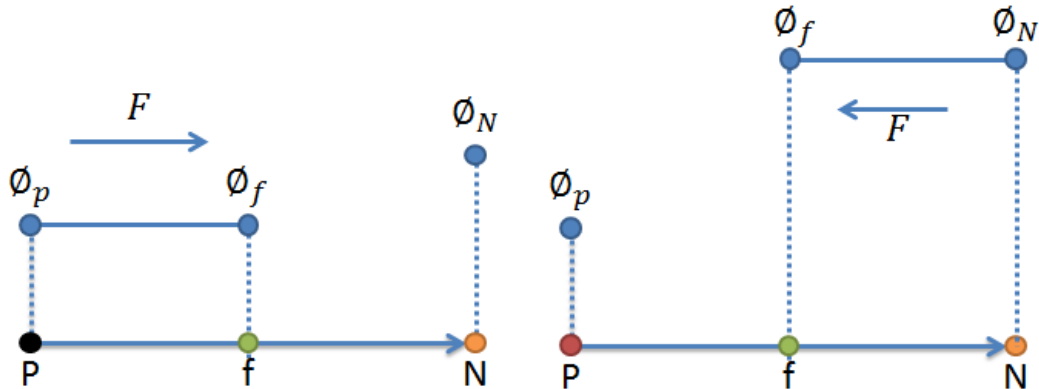
Figure 3.8: Central scheme

- Upwind scheme

Another scheme is the upwind scheme, in which the face value of transport quantity (ϕ_f) is determined according to the direction of the flux term (F) as shown in Figure 3.9 .

$$\phi_f = \begin{cases} \phi_p & \text{for } F \geq 0 \\ \phi_N & \text{for } F < 0 \end{cases} \quad (3.15)$$

This scheme satisfies the boundedness, but it may introduce false diffusion problem because it is first order accuracy scheme.


 Figure 3.9: Upwind scheme for $F>0$ and $F<0$

- Hybrid scheme

The hybrid scheme is based on the combination of central and upwind scheme. The central difference scheme, which is second order accuracy, is used for small peclet number (peclet number<2). While upwind scheme, which is first order accuracy but accounts for transportiveness is used for large peclet number (peclet number ≥ 2).

- Quick scheme

Quick scheme is upstream quadratic interpolation scheme which uses three point weighted quadratic interpolation to obtain cell face value; the face value $\bar{\phi}_f$ is obtained from quadratic function passing through two bounding nodes and one node upstream. The expression for determining $\bar{\phi}_f$ using normalized variable is shown in Eq.(3.16). Normalized variables profile is shown in Figure 3.10.

$$\bar{\phi}_f = \bar{x}_f + \frac{\bar{x}_f(\bar{x}_f - 1)}{\bar{x}_c(\bar{x}_c - 1)} (\bar{\phi}_c - \bar{x}_c) \quad (3.16)$$

$$\bar{x} = \frac{x - x_U}{x_D - x_U} \quad (3.17)$$

$$\bar{\phi}_f = \frac{\bar{\phi}_f - \bar{\phi}_U}{\bar{\phi}_D - \bar{\phi}_U} \quad (3.18)$$

Where;

$\bar{\phi}_D$: Value of ϕ at the nearest grid point on the downstream side of the face.

$\bar{\phi}_U$: Value of ϕ at the grid point above $\bar{\phi}_c$.

$\bar{\phi}_c$: Value of ϕ at the nearest grid point on the upstream side of the face.

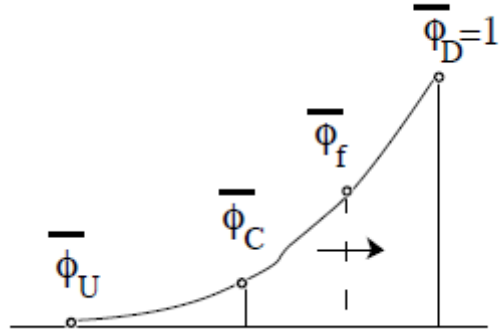


Figure 3.10: Normalized variables[7]

The quick scheme is third order accuracy, which retain transportiveness. But drawback of this scheme is instability problem which may cause minor undershoot or overshoot, so the resulting solution is not bounded[8].

- Smart scheme

To solve instability problem in the quick scheme, smart scheme was introduced. It is second to fourth order accuracy. It is composed by quick straight line, a portion of the downwind line close to ($\bar{\phi}_f = 1$), and a straight line with slope 3 connecting to ($\bar{\phi}_f = 0$) [9].

$$\bar{\phi}_f = \begin{cases} \frac{\bar{x}_f(1 - 3\bar{x}_c + 2\bar{x}_f)}{\bar{x}_c(1 - \bar{x}_c)} \bar{\phi}_c & , 0 < \bar{\phi}_c \leq \frac{\bar{x}_c}{3} \\ \bar{x}_f + \frac{\bar{x}_f(\bar{x}_f - 1)}{\bar{x}_c(\bar{x}_c - 1)} (\bar{\phi}_c - \bar{x}_c), & \frac{\bar{x}_c}{3} < \bar{\phi}_c \leq \frac{(1 + \bar{x}_f - \bar{x}_c)\bar{x}_c}{\bar{x}_f} \\ 1 & \frac{\bar{x}_c}{3} < \bar{\phi}_c \leq \frac{(1 + \bar{x}_f - \bar{x}_c)\bar{x}_c}{\bar{x}_f} \\ \bar{\phi}_c & otherwise \end{cases} \quad (3.19)$$

3.2.4 Discretization of source term

The source term in the momentum equation consists of the pressure gradient term and the Boussinesq term in the momentum in y-direction. Central scheme is used in the pressure gradient term. Linear interpolation is used in the Boussinesq term to obtain the temperature at the center of the control volume T_p .

$$\int_s p n_x ds = (p_e - p_w) A_e \quad (3.20)$$

$$T_p = T_e \frac{A_{An}}{A_{AB}} + T_w \frac{A_{Bn}}{A_{AB}} \quad (3.21)$$

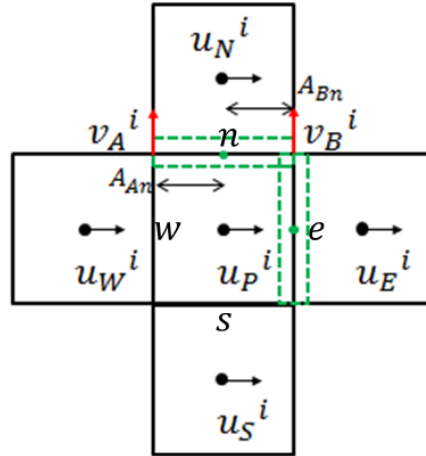


Figure 3.11: control volume for momentum equation in x-direction

3.2.5 Temporal discretization

In the previous sections, the discretization of the spatial terms was presented. Let us now consider the temporal derivative of the general transport equation. In order to simplify the notation, general transport equations can be rewritten as

$$\rho \frac{\partial \phi}{\partial t} = R(\phi) + S \quad (3.22)$$

Where the source term is equal to the pressure gradient in momentum equation ($S = \nabla p$). In the energy equation the source term is zero ($S = 0$). $R(u)$ stands for the convective and diffusive terms.

$$R(\phi) = -\rho(\nabla \cdot u)\phi + \nabla(\Gamma \nabla \phi) \quad (3.23)$$

For the temporal discretization, a central difference scheme is used for the time derivative term.

$$\rho \left. \frac{\partial \phi}{\partial t} \right|^{n+1/2} \approx \rho \frac{\phi^{n+1} - \phi^n}{\Delta t} \quad (3.24)$$

A fully explicit second-order Adams-Bashforth scheme for $\mathbf{R}(\emptyset)$

$$\mathbf{R}^{n+1/2}(\emptyset) \approx \frac{3}{2} \mathbf{R}(\emptyset^n) - \frac{1}{2} \mathbf{R}(\emptyset^{n-1}) \quad (3.25)$$

First order backward Euler scheme is for the pressure gradient term in the momentum equation, then the discretized general transport equations are as follows;

$$\rho \frac{\mathbf{u}^{n+1} - \mathbf{u}^n}{\Delta t} = \frac{3}{2} \mathbf{R}(\mathbf{u}^n) - \frac{1}{2} \mathbf{R}(\mathbf{u}^{n-1}) - \nabla p^{n+1} \quad (3.26)$$

$$\rho \frac{\mathbf{T}^{n+1} - \mathbf{T}^n}{\Delta t} = \frac{3}{2} \mathbf{R}(\mathbf{T}^n) - \frac{1}{2} \mathbf{R}(\mathbf{T}^{n-1}) \quad (3.27)$$

4 Algorithm for pressure velocity coupling (fractional step method)

This method was proposed by Chorin and Temam , which is usually known as the projection method for solving the Navier-Stokes equations because equations are interpreted as projection into a divergence-free velocity space. Predictor velocity is firstly obtained by solving the momentum equation which is an approximate solution because momentum equation does not include the pressure gradient contribution, so it does not satisfy the incompressibility constraint in the next time step. Then the Poisson equation is solved to get the pressure, which is used to correct the predictor velocity to satisfy the incompressibility constraint.

4.1 Derivation

As mentioned before in the previous chapter in section 3.2.5, that momentum equation is integrated in time using fully explicit time integration scheme as in Eq.(4.1).

$$\rho \frac{\mathbf{u}^{n+1} - \mathbf{u}^n}{\Delta t} = \frac{3}{2} \mathbf{R}(\mathbf{u}^n) - \frac{1}{2} \mathbf{R}(\mathbf{u}^{n-1}) - \nabla p^{n+1} \quad (4.1)$$

The predictor velocity (\mathbf{u}^p) can be uniquely decomposed into divergence free vector (\mathbf{u}^{n+1}), and the gradient of the scalar field (∇p). This decomposition is derived using Helmholtz-Hodge vector decomposition theorem. This decomposition is written as follows;

$$\mathbf{u}^p = \mathbf{u}^{n+1} + \frac{\Delta t}{\rho} \nabla p^{n+1} \quad (4.2)$$

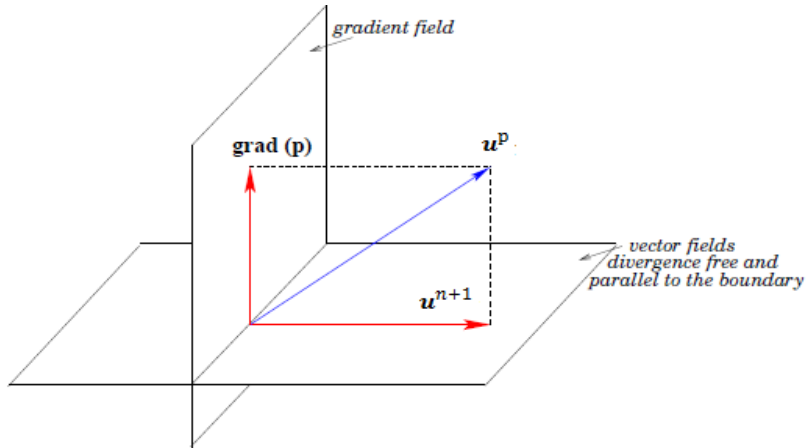


Figure 4.1: predictor velocity decomposition [10]

The original momentum equation is transformed to the following pressure independent equation.

$$\mathbf{u}^p = \mathbf{u}^n + \frac{\Delta t}{2} \left(\frac{3}{2} \mathbf{R}(\mathbf{u}^n) - \frac{1}{2} \mathbf{R}(\mathbf{u}^{n-1}) \right) \quad (4.3)$$

By taking the divergence of Eq.(4.2) yields Poisson equation for solving the pressure.

$$\nabla \cdot (\mathbf{u}^p) = \nabla \cdot (\mathbf{u}^{n+1}) + \nabla \cdot \left(\frac{\Delta t}{\rho} \nabla p^{n+1} \right) \quad (4.4)$$

For compressible flow $\nabla \cdot (\mathbf{u}^{n+1}) = 0$, so Poisson equation is as follows;

$$\Delta p^{n+1} = \frac{\rho}{\Delta t} \nabla \cdot \mathbf{u}^p \quad (4.5)$$

Finally, velocity at new time step (\mathbf{u}^{n+1}) is obtained from original decomposition equation Eq.(4.2).

$$\mathbf{u}^{n+1} = \mathbf{u}^p - \frac{\Delta t}{\rho} \nabla p^{n+1} \quad (4.6)$$

- **Discretization of Poisson equation**

Gauss theorem is applied to Poisson equation Eq.(4.7) yields Eq. (4.8).

$$\int_V \Delta p^{n+1} dV = \frac{\rho}{\Delta t} \int_V \nabla \cdot \mathbf{u}^p dV \quad (4.7)$$

$$\int_S \nabla p^{n+1}_f \cdot n dS = \frac{\rho}{\Delta t} \int_S \mathbf{u}^p_f \cdot n dS \quad (4.8)$$

Poisson equation will be discretized on the pressure control volume as shown in Figure 4.2.

$$\begin{aligned} & \frac{P_E^{n+1} - P_p^{n+1}}{d_{Ep}} A_e + \frac{P_N^{n+1} - P_p^{n+1}}{d_{Np}} A_n - \frac{P_p^{n+1} - P_w^{n+1}}{d_{Wp}} A_w - \frac{P_p^{n+1} - P_s^{n+1}}{d_{Sp}} A_s \\ &= \frac{1}{\Delta t} [(\rho u^p)_e A_e + (\rho u^p)_n A_n - (\rho u^p)_w A_w + (\rho u^p)_s A_s] \end{aligned} \quad (4.9)$$

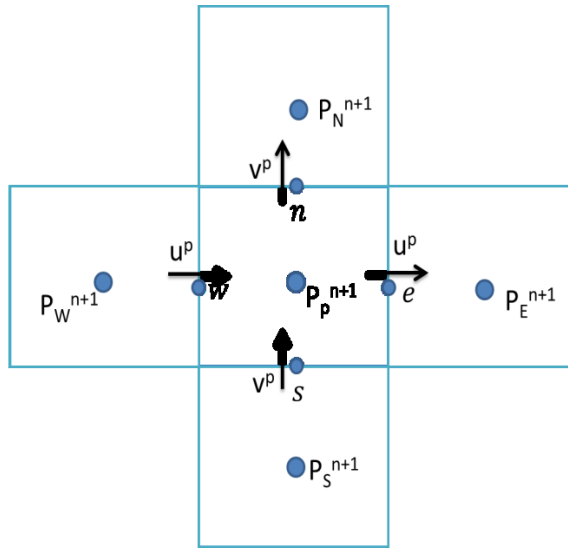


Figure 4.2: pressure control volume.

The discretized equation Eq.(4.9) can be written as follows;

$$a_p p_p^{n+1} = a_E p_E^{n+1} + a_N p_N^{n+1} + a_W p_W^{n+1} + a_S p_S^{n+1} + b_p \quad (4.10)$$

Where the coefficient of Eq.(4.10) are show in Eq.(4.11) till Eq.(4.15)

$$a_E = \frac{A_e}{d_{EP}} \quad (4.11)$$

$$a_W = \frac{A_w}{d_{WP}} \quad (4.12)$$

$$a_N = \frac{A_n}{d_{NP}} \quad (4.13)$$

$$a_S = \frac{A_s}{d_{SP}} \quad (4.14)$$

$$b_p = \frac{-1}{\Delta t} [(\rho u^p)_e A_e + (\rho u^p)_n A_n - (\rho u^p)_w A_w - (\rho u^p)_s A_s] \quad (4.15)$$

Any linear solver like Gauss-Seidal or Tridiagonal matrix algorithm+Gauss-Seidal can be used to solve Poisson, which will be discussed in the following section.

4.2 Solvers for discretized equations

In the previous section set of algebraic equation like Poisson equation need linear equation solvers. There are two types of solution techniques for linear system of equations: direct method and indirect or iterative method.

Iterative solver like Gauss-Sedial is based on repeated application of relatively simple algorithm until the convergence is achieved after number of iteration, but the convergence rate can be slow when the system of equations is large.

Direct solver like tri-diagonal matrix algorithm (TDMA) developed by Thomas (1949), which is direct method for solving one-dimensional problems. Also it can be used iteratively in line by line technique in order to solve multi-dimensional problems. Its advantage is computationally inexpensive compared to Gauss-Sedial.

4.2.1 Gauss-Sedial

This solver start by using the assumed initial guess for the variable ϕ_{guess} , new value for variable ϕ_p is calculated. If the new value satisfies the convergence criteria, the iteration loop stops. Else the new value is used as initial guess in the next iteration. These steps are repeated until convergence is achieved. Algorithm for Gauss-Sedial is shown in Figure 4.4. Only diagonally dominant coefficient matrix or symmetric positive definite matrix can achieve convergence for system of equation using Gauss-Sedial [11], which means that the coefficient on the diagonal must be at least equal to the sum of the other coefficients in that row and at least one row with a diagonal coefficient greater than the sum of the other coefficients in that row.

4.2.2 Tri-diagonal matrix algorithm

Tridiagonal solver is based on Gaussian elimination. First we create zeros below the diagonal and then once we have a triangular matrix, we solve for the ϕ_p using back substitution. Consider a system of equations that has a tri-diagonal form.

$$\begin{bmatrix} \phi_1 & 0 & 0 & 0 \\ -\beta_2\phi_1 & D_2\phi_2 & -\alpha_2\phi_3 & 0 \\ 0 & -\beta_3\phi_2 & D_3\phi_3 & -\alpha_3\phi_4 \\ 0 & 0 & 0 & \phi_4 \end{bmatrix} = \begin{bmatrix} c_1 \\ c_2 \\ c_3 \\ c_4 \end{bmatrix} \quad (4.16)$$

By applying forward substitution and backward elimination, we get that general form Eq.(4.17)

$$\phi_j = A_j \phi_{j+1} + C'_j \quad (4.17)$$

Where

$$A_j = \frac{\alpha_j}{D_j - A_{j-1}B_j} \quad (4.18)$$

$$C'_j = \frac{B_j C'_{j-1} + C_j}{D_j - B_j A_{j-1}} \quad (4.19)$$

- Algorithm for TDMA

- I. for $i = 1, \dots, N$

Evaluate A_j and C'_j

- II. for $i = N, \dots, 1$

Evaluate $\phi_j = A_j \phi_{j+1} + C'_j$

4.2.3 Line by line TDMA in 2D dimensional problem

TDMA can be used iteratively to solve system of equations for two dimensional problems. General transport equation is as follow;

$$\phi_p a_p = a_E \phi_E + a_W \phi_W + a_N \phi_N + a_S \phi_S + b \quad (4.20)$$

To solve TDMA along (south-North) lines as shown in Figure 4.3. Eq.(4.20) has to be rearranged as shown in Eq.(4.21).

$$-a_N \phi_N + \phi_p a_p - a_S \phi_S = a_E \phi_E + a_W \phi_W + b \quad (4.21)$$

Eq.(4.21) is in the form of Eq.(4.17), so the equation coefficient (α_j, B_j, D_j, C_j) have to be changed to apply TDMA on vertical lines from south to north.

$$B_j = a_S \quad (4.22)$$

$$\alpha_j = a_N \quad (4.23)$$

$$D_j = a_p \quad (4.24)$$

$$C_j = a_E \emptyset_E + a_W \emptyset_W + b \quad (4.25)$$

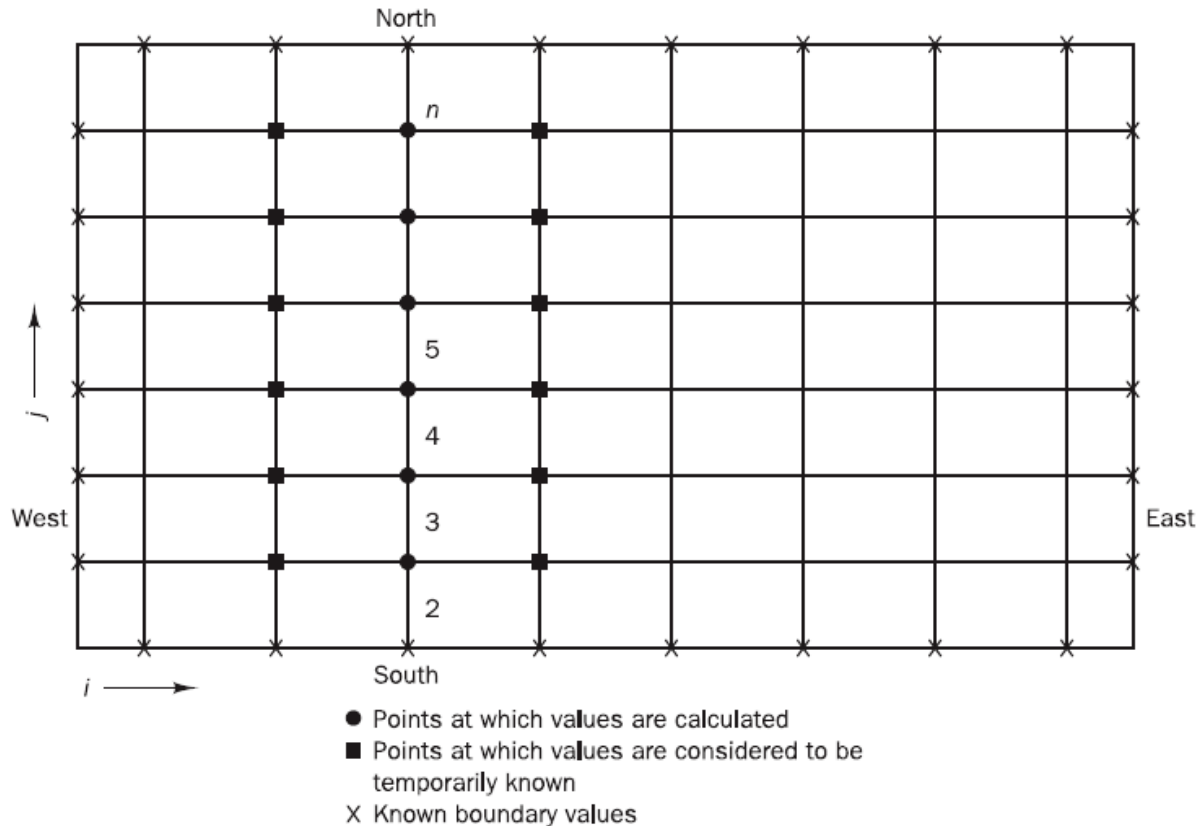


Figure 4.3: TDMA line by line[8]

After calculation of vertical line from south to north, same procedures are done for the next line. The next line can be on east or west according to the sweep direction. If the sweep direction is from west to east. The values of point to the west of point P (\emptyset_W) are known while the points on the east (\emptyset_E) are unknown. Line by line calculations is repeated for several number of iteration in which values at end of each iteration are used as initial guess for unknown points in the new iteration. This process is repeated till convergence is achieved.

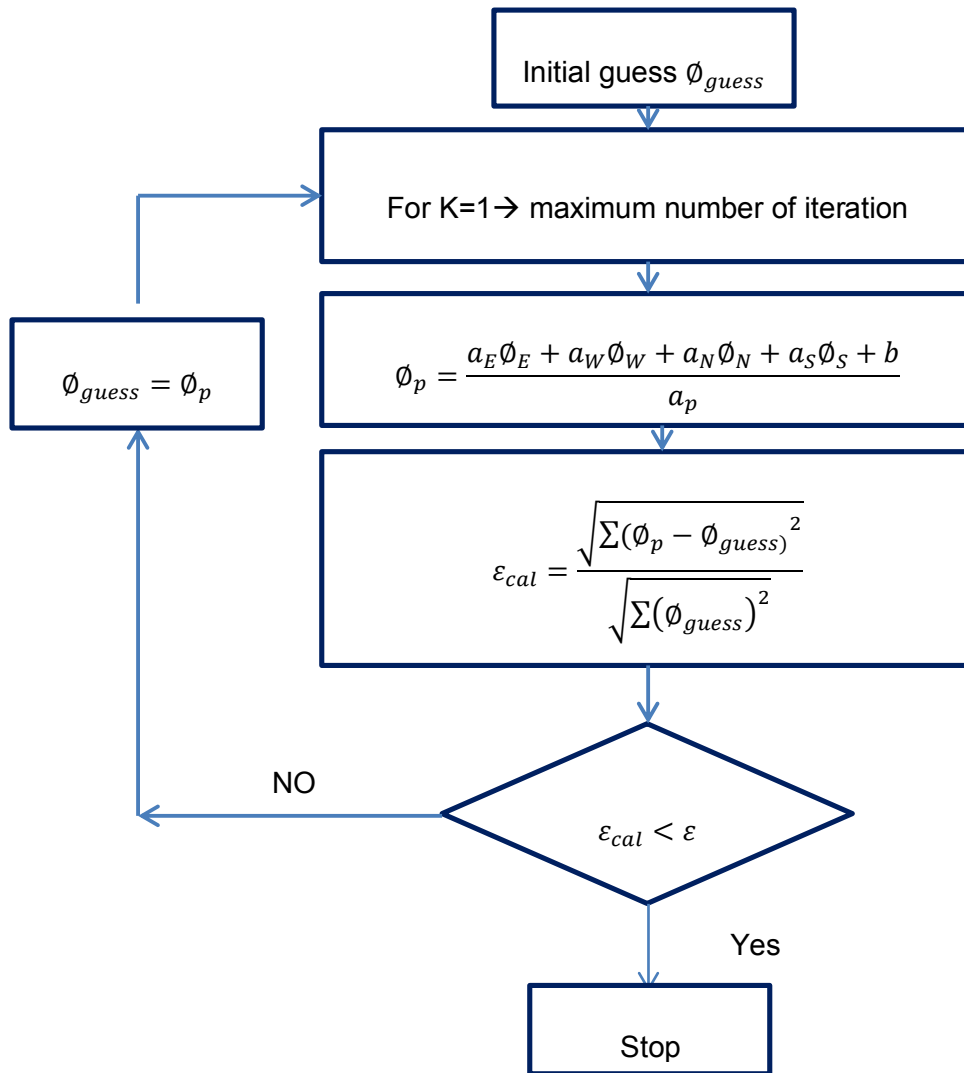


Figure 4.4: Gauss-Seidel Algorithm

4.3 Boundary conditions

Every interior control volume is bounded by four control volumes in 2D problems and is governed by one algebraic equation. Volume integrals are performed for all interior control volume in the same way except for control volume, which one of its faces coincides with the domain boundary, requires special treatment. The values of physical properties ϕ have to be known on the faces that coincide with domain boundary or expressed as function of the interior point using forward or backward differences.

4.3.1 Types of boundary conditions

Mainly, there are three boundary conditions which are used to close the system of equations that will be used in proposed CFD problem,

- Constant gradient boundary condition: by defining the solution gradient of transport quantity ϕ to be constant at direction normal to the boundary face. This condition is also known as a Neumann type boundary condition. It is commonly used for the pressure inlet condition, at the walls by setting gradient to zero, and for velocity at outlet boundary condition.

$$\frac{\partial \phi}{\partial n} = \text{constant} \quad (4.26)$$

Where;

n :direction normal to the boundary

For implementing Neumann boundary condition for the velocity for the east face, it can be easily applied as shown in Eq.(4.33).

$$\frac{u_p - u_E}{\Delta x} = \text{constant} \quad (4.27)$$

But if the transport quantity is not solved directly, but solver is used like the pressure in which solver is used to solve Poisson equation. The coefficients of the pressure equation have to be assumed as shown in Eq.(4.28) , if Neumann boundary condition is applied to the east face.

$$a_E = 0$$

$$a_W = 1$$

$$a_S = 0 \quad (4.28)$$

$$a_N = 0$$

$$a_p = 1$$

$$b = \text{constant}$$

- Fixed value boundary condition: is specified by setting the transport quantity ϕ to constant value for the nodes on the boundary face. It is also known by Dirichlet boundary condition. It is commonly used in the inlet boundary and outlet for setting

velocity, temperature and pressure by specific value. Also on the wall to set no slip boundary condition by setting velocity to zero at the wall surface

$$\emptyset = \text{constant} \quad (4.29)$$

For applying Dirichlet boundary condition to directly solved quantities like velocity, and temperature, it is set as shown in Eq.(4.29), but if the transported quantity is solved by using solver, the coefficient of transport equation has to be as follows.

$$\begin{aligned} a_E &= 0 \\ a_W &= 0 \\ a_N &= 0 \\ a_S &= 0 \\ a_p &= 1 \\ b &= \text{constant} \end{aligned} \quad (4.30)$$

- Convective boundary condition (CBC): it is used in open outlet boundary condition. Convective boundary layer requires less CPU time compared to Neumann condition. Moreover, it reduces the downstream extent of the computational domain[12].

$$u_N^{n+1} = u_N^n - \frac{\Delta t}{(\Delta x)_N} u_c (u_N^n - u_{N-1}^n) \quad (4.31)$$

Where u_c is the convective velocity. The value of u_c is set to free stream velocity u_∞ [13]. Sub index denote position and super index denote time step, where N is the outlet and n the current time step.

4.4 Determination of time step

In proposed fractional step method fully explicit time scheme is used, so determination of time step is so critical due to stability reasons. Time step has to fulfill the following Courant-Friedrichs-Lowy (CFL), in which time-step must be less than the time for the wave to travel to adjacent grid points. CFL is a necessary condition for convergence while solving certain partial differential equations numerically by the method of finite differences , so time step has to be bounded by CFL condition [14].

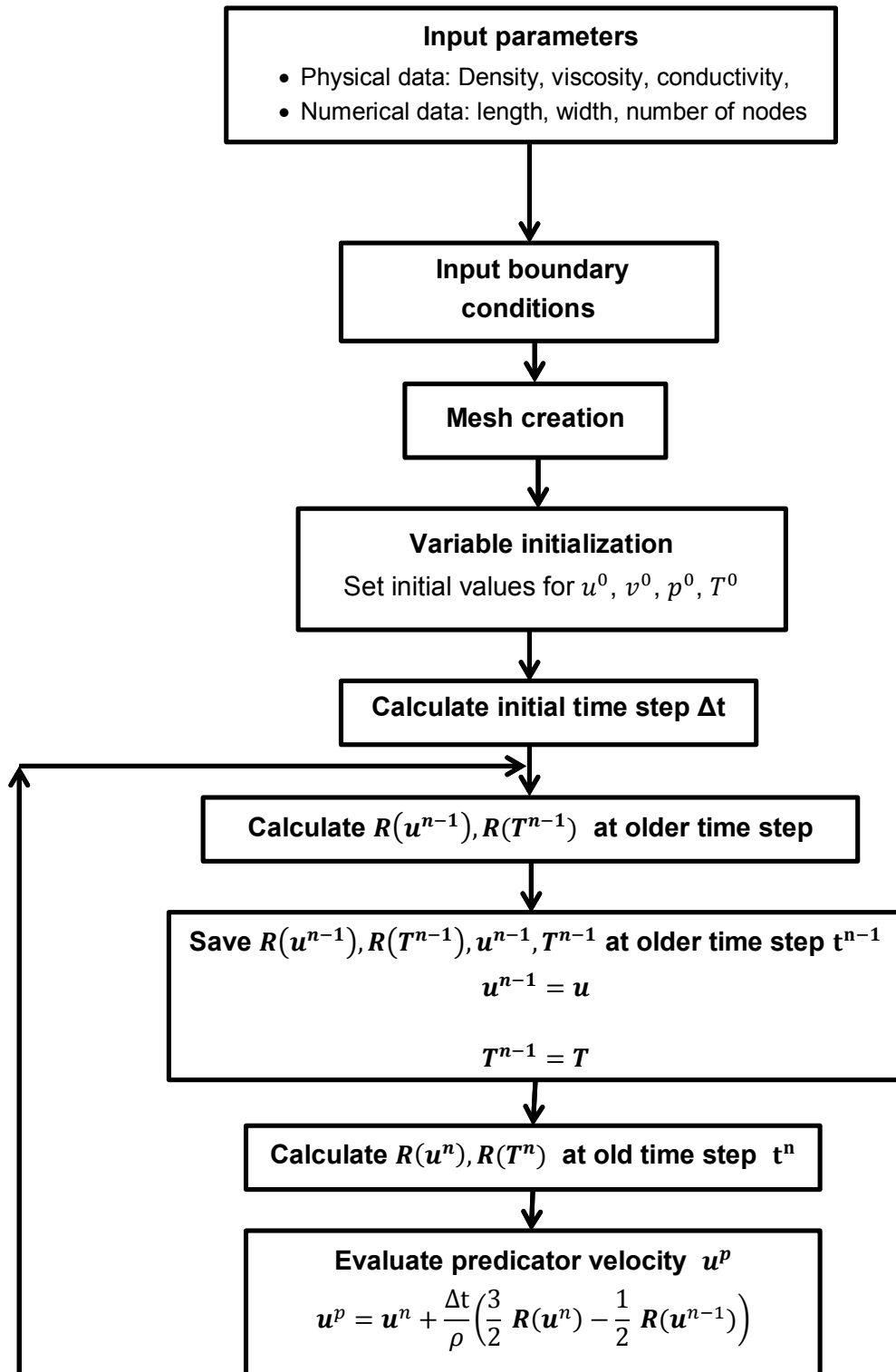
$$\Delta t \left(\frac{|u_i|}{\Delta x_i} \right)_{max} \leq C_{conv} \quad (4.32)$$

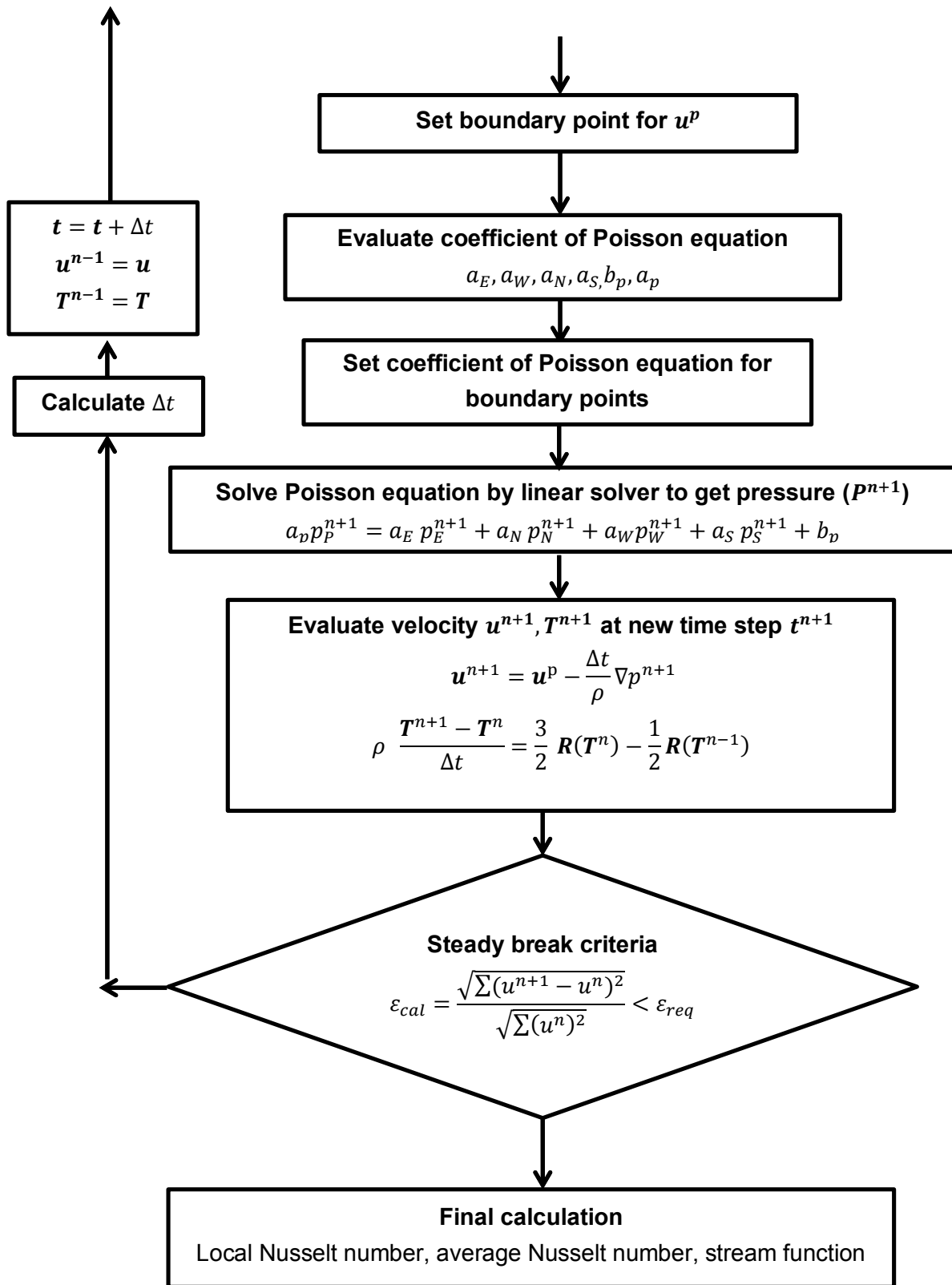
$$\Delta t \left(\frac{\Gamma}{\rho \Delta x_i^2} \right)_{max} \leq C_{visc} \quad (4.33)$$

The bounding constant C_{conv} are C_{visc} have to be smaller than unity. The recommended values for C_{conv} are C_{visc} are 0.35 and 0.2 respectively as proposed by [15]. The CFL condition for diffusion is calculated only one time because viscosity and mesh does not change with time ,while CFL condition for convection has to be calculated each time step because of changing velocity.

4.5 Solving Algorithm

In the previous sections, Different parts of program are discussed separately. In this part, these different sections are assembled together to have an overview of the program sequence as shown in Figure 4.5.





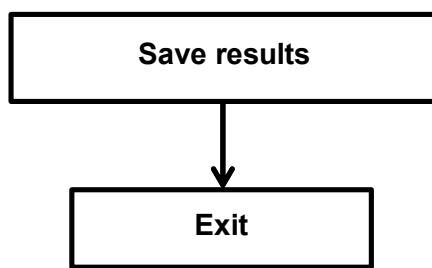


Figure 4.5: Solver algorithm

5 Software verification

In this chapter, the verification of the computer code will be discussed briefly. Verification provides evidence that the conceptual model is solved correctly by discrete mathematics that is performed by the computer code. Verification does not ensure that the conceptual model has any relation to the real world. But comparing computational model to real or experimental model is called validation which will not be addressed in our work.

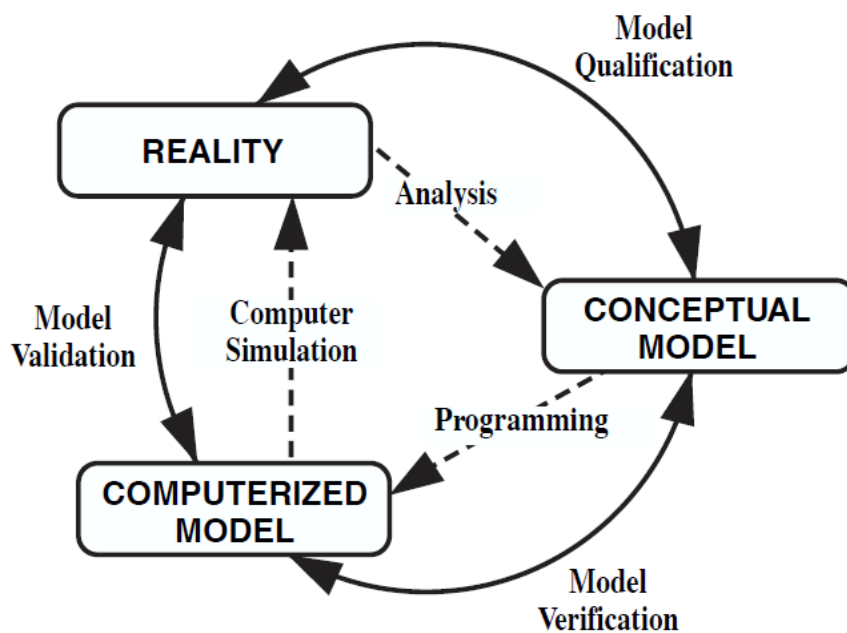


Figure 5.1:Difference between model verification and validation[16]

The fundamental strategy of verification is the identification of the error, error quantification and error reduction in the computational model solution. To quantify the numerical error in the computational model, it has to be compared to high accurate benchmark PDE solutions or with analytical solution like Method of Manufactured solution, but highly accurate solution is only available for relatively small number of simplified cases. Examples of benchmark PDE solutions in fluid dynamics are the following: incompressible laminar flow over a semi-infinite flat plate; incompressible laminar flow over a parabolic plate; incompressible laminar flow in a square cavity driven by a moving wall; laminar natural convection in a square cavity, and incompressible laminar flow over a backward-facing step, with and without heat transfer. In order to quantify error, global or local error norms have to be calculated to assess the agreement of the model with the high accurate solution as shown in Figure 5.2.

The most common sources of errors in CFD solution are as follows;

- Insufficient spatial discretization convergence
- Insufficient temporal discretization convergence
- Insufficient convergence of iterative procedures
- Computer round-off
- Computer programming errors

The first three sources of error are the most common sources of error in CFD problems. The fourth error is rarely dealt with in CFD. Computer programming errors are more related to computer science, which occur in input or output data files and compilers.

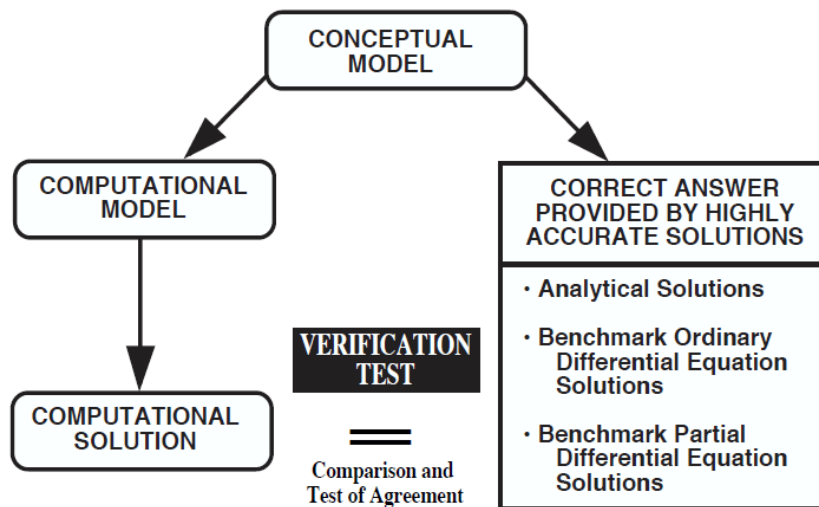


Figure 5.2: verification process

In the presented works, computer code will be verified using Method of manufactured and will be compared with two benchmark solution: square Driven cavity and differentially heated square cavity.

5.1 Method of Manufactured Solution

A manufactured solution (MMS) is an exact solution for PDE that has been constructed by solving the equation backwards. Let differential equation that has the following form.

$$\mathbf{D}\phi = S_\phi \quad (5.1)$$

Where \mathbf{D} is the differential operator, ϕ is the solution, and S_ϕ is a source term. In the exact solution, the source term S_ϕ is applied, then using method from applied mathematics to invert the operator to get solution for ϕ . In MMS, firstly manufactured solution for ϕ is assumed, and then the operator \mathbf{D} is applied to ϕ to get the source term that satisfied the equation.

MMS verification procedures

- Construct the manufactured solution, in which the analytical function ϕ_a is chosen.
- The source term S_ϕ is obtained by isolating the source term in the PDE.
- Boundary conditions in the domain are obtained by using the analytical function ϕ_a .
- By using numerical discretization of domain in the code, numerical solution ϕ_n is obtained, which has to be compared to analytical solution ϕ_a .
- Grid refinement is performed to obtain error using Eq.(5.3) on sequence of grids to test the code on general level, where ϕ_a is the analytical solution and ϕ_n is numerical solution.

$$E = \frac{\max|\phi_a - \phi_n|}{\max|\phi_a|} \quad (5.2)$$

- Compare the order of accuracy to the theoretical order using Eq.(5.3) , where r is the grid refinement ratio and E is the error.

$$\text{Accuracy order} = \log_r \left(\frac{E_{grid1}}{E_{grid2}} \right) \quad (5.3)$$

Manufactured solution has to follow specific guidelines. MMS has to be composed of analytical function like polynomials, trigonometric, or exponential function. Also, it should have a sufficient number of non-trivial derivatives.

5.1.1 Verification of coupling of the steady continuity and momentum equation, with staggered mesh and unknown field by MMS.

The equations that will be verified are continuity and momentum equation, in which the unknowns are u , v and p .

$$\frac{\partial u}{\partial x} + \frac{\partial v}{\partial y} = 0 \quad (5.4)$$

$$\rho u \frac{\partial u}{\partial x} + \rho v \frac{\partial u}{\partial y} = -\frac{\partial p}{\partial x} + \Gamma \left(\frac{\partial^2 u}{\partial x^2} + \frac{\partial^2 u}{\partial y^2} \right) + F_x \quad (5.5)$$

$$\rho u \frac{\partial v}{\partial x} + \rho v \frac{\partial v}{\partial y} = - \frac{\partial p}{\partial y} + \Gamma \left(\frac{\partial^2 v}{\partial x^2} + \frac{\partial^2 v}{\partial y^2} \right) + F_y \quad (5.6)$$

The verification process by MMS is divided into three steps; firstly, verification of the momentum equation in x-direction is studied separately. Secondly, similar step to previous step is done to verify the momentum equation in y-direction. Finally, the coupling between the momentum equation and continuity equation is studied.

5.1.1.1 Verification of momentum equation in x-direction

To verify the momentum equation in x- direction. The velocity field in x-direction u is the unknown while the other variables p , and v are known. Analytical solution is chosen as shown in the following equations.

$$u = x^2 y \quad (5.7)$$

$$v = -y^2 x \quad (5.8)$$

$$p = x^3 + y^3 \quad (5.9)$$

The analytical velocity field (u, v) satisfies the continuity equation. The partial derivatives are calculated and substituted in the momentum equation in x-direction Eq.(5.5) to obtain the source term F_x as shown in Eq.(5.10).

$$F_x = \rho x^3 y^2 + 3x^2 - 2\Gamma y \quad (5.10)$$

The equation in the numerical code is solved considering:

- Density: $\rho = 1 \text{ kg/m}^3$
- Diffusivity: $\Gamma = 0.5 \text{ kg/m}^2 \text{s}$
- Domain: L=1.5 and W=1
- Criterion to stop program execution: $|u^{n+1} - u^n| < 10^{-8}$

The program is tested for different meshes using grid refinement ratio of two. The error using Eq.(5.2) and the accuracy order are calculated using Eq.(5.3) for the different meshes as shown in Table 5.1

From Table 5.1, it is clearly seen that the error decrease with decreasing mesh size. Also, in the program upwind scheme is used, which is first order scheme and the accuracy order

obtained from our program is close to unity which match the order of the numerical scheme used.

Mesh	Error	Accuracy order
15*10	1.03E-02	
30*20	5.43E-03	0.923093692
60*40	2.75E-03	0.983496785
120*80	1.39E-03	0.987274465

Table 5.1: Table of the error convergence for u

5.1.1.2 Verification of momentum equation in y-direction

Here the velocity in y-direction v is the unknown while the other variables p, u are known. Same equations and parameter are used similar to the previous case as shown in Eqs.(5.7),(5.8) and (5.9). After substituting the partial derivatives in momentum equation in y-direction Eq.(5.6). The source term F_y is obtained as shown in the following expression.

$$F_y = \rho x^2 y^3 + 3y^2 + 2\Gamma x \quad (5.11)$$

The program is tested for different meshes using grid refinement ratio of two. The error using Eq.(5.2) and the accuracy order are calculated using Eq.(5.3) for the different meshes as shown in Table 5.2.

Mesh	Error	Accuracy order
15*10	0.019184	
30*20	0.008487	1.176613201
60*40	0.004049	1.067764727
120*80	0.001979	1.032977879

Table 5.2: Table of the error convergence for v

It is clearly seen from Table 5.2 that the error decreases with decreasing the mesh size. Moreover, the accuracy order is close to unity as predicted because of the upwind scheme used, which is first order accuracy scheme.

5.1.1.3 Verification of the coupling between momentum and continuity equation

After verifying the momentum equation in x and y direction individually. The coupling between momentum and continuity equation need to be checked. Same velocity field and pressure field equations are used as shown in Eqs.(5.7), (5.8) and (5.9). The same source terms F_y, F_x for the momentum equations in x and u direction as indicated in Eqs (5.10) and (5.11).

In this case the unknown variables are u, v and p . Boundary points are calculated using the given velocity and pressure fields. The error between the analytical and numerical solution is checked for u, v and p using different meshes. Also the accuracy order is calculated for different meshes.

In this case the considered parameter are as follows;

- Density : $\rho = 2\text{kg}/\text{m}^3$
- Diffusivity : $\Gamma = 0.8 \frac{\text{kg}}{\text{m}^3\text{s}}$
- Domain: L=1 and W=1.5
- Criteria to stop pressure solver $|p - p_{guess}| < 10^{-8}$
- Criteria to stop program execution : $|u^{n+1} - u^n| < 10^{-8}$

The error velocity in x and y direction u and v are presented in Table 5.3. Moreover, numerical code is tested on different mesh size using mesh refinement ratio of two. Finally the accuracy order is calculated.

Mesh	Error in u	Accuracy order for u	Error in v	Accuracy order for v
10*15	0.003974		0.00564	
20*30	0.002198	0.854400486	0.002345	1.266301733
40*60	0.001151	0.933264162	0.001066	1.136595615
80*120	0.000587	0.970699965	0.000513	1.056859682
160*240	0.000298	0.980616853	0.000251	1.030496147

Table 5.3: Table of the error convergence for u and v

From Table 5.3, it can be observed that error in u and v decrease with decreasing mesh size. Moreover, the accuracy order is close to one because of upwind scheme used in the convective term in the momentum equation which mean that the error in the convective scheme predominates over the other numerical schemes used.

5.2 Reference cases

The goal of this section is to verify that the code used for solving Navier-stokes equation works properly by comparing its solution to highly accurate problems like Driven cavity and differentially heated cavity.

5.2.1 Driven square cavity

5.2.1.1 Problem description

The problem considers incompressible flow in a square cavity placed in x-y plane with upper wall moving with uniform velocity u in x-direction. The other walls have no slip boundary conditions as shown in Figure 5.3.

5.2.1.2 Boundary conditions

For the velocity, no slip boundary condition is applied on the left, right and bottom wall ($u = v = 0$). For the top wall, Dirichlet boundary condition is used for velocity in x-direction ($u = 1, v = 0$).

For the pressure, zero Neumann boundary condition in normal direction to the wall is applied for the four wall $\frac{\partial p}{\partial n} = 0$. For solving the pressure linear solver is used like TDMA or Gauss-Seidal which will have infinite number of solution if zero Neumann boundary condition is used for all the walls. In order to avoid this problem, the pressure has to be set to reasonable value at any point in the solution domain.

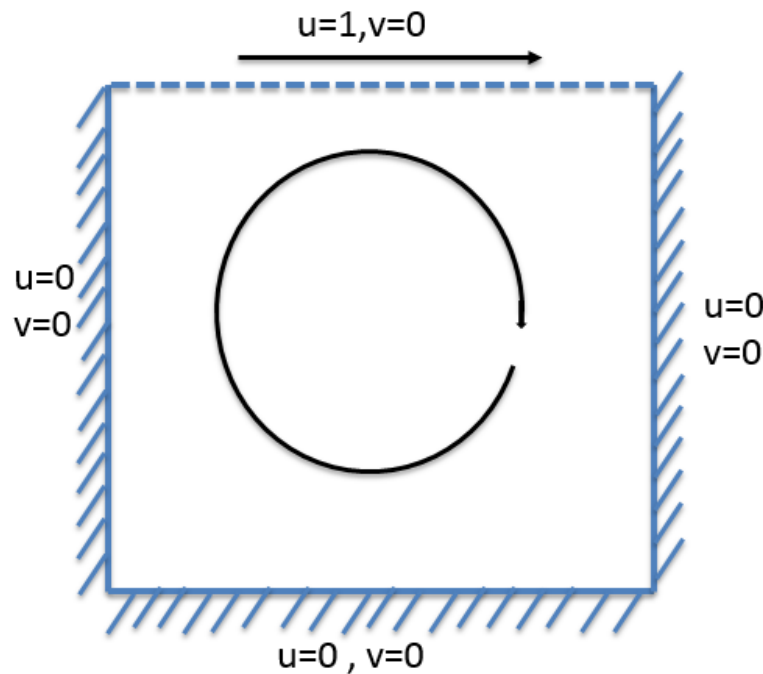


Figure 5.3: Driven cavity problem description

5.2.1.3 Results

The case will be solved for different Reynolds numbers 100, 400, 3200 and 7500. Different numerical schemes will be tested like central, upwind, Hybrid and smart. u-velocity profiles along a vertical line passing through the geometric centre of the cavity and v-velocity profiles along a horizontal line passing through the geometric centre of the cavity at various Reynolds numbers will be evaluated and compared to Benchmark solution[17]. Also the streamline will be plotted for different Reynolds number.

Firstly different numerical schemes for convective term are tested on mesh size of 50 by 50 and compared to the Benchmark solution as shown in Figure 5.4 and Figure 5.5 . It is clearly seen that, the solution using smart and central scheme are quite similar to the benchmark solution, so smart scheme will be used for the other Reynolds numbers.

Comparison between program solution and benchmark solution for different Reynolds are shown in the following figures from Figure 5.6 till Figure 5.13. Streamlines for different Reynolds number are shown in Figure 5.14 till Figure 5.18.

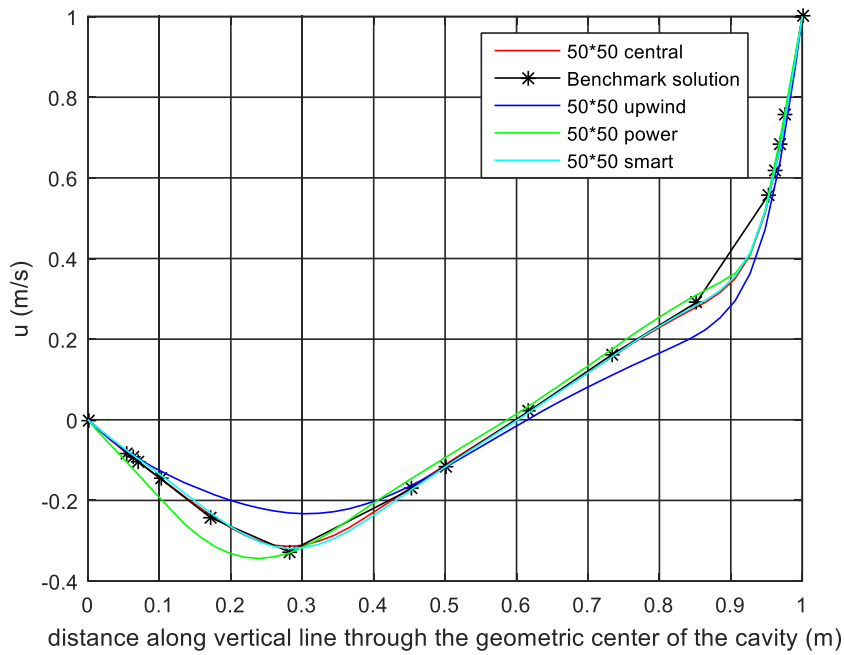


Figure 5.4: Comparison of u velocity with Benchmark solution for $Re=400$ using different numerical scheme on mesh $50*50$

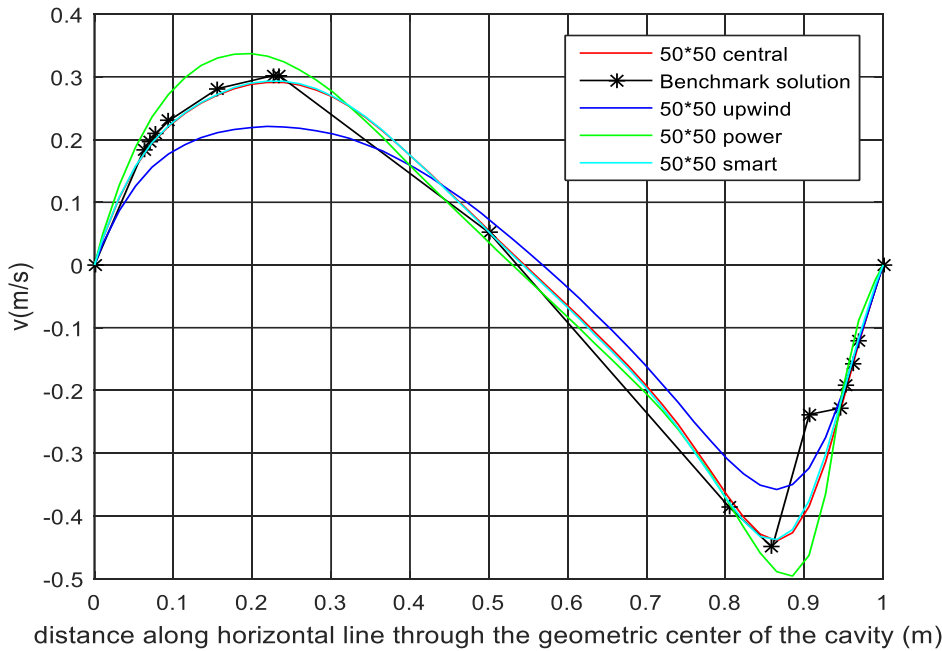


Figure 5.5: Comparison of v velocity with Benchmark solution for $Re=400$ using different numerical scheme on mesh $50*50$

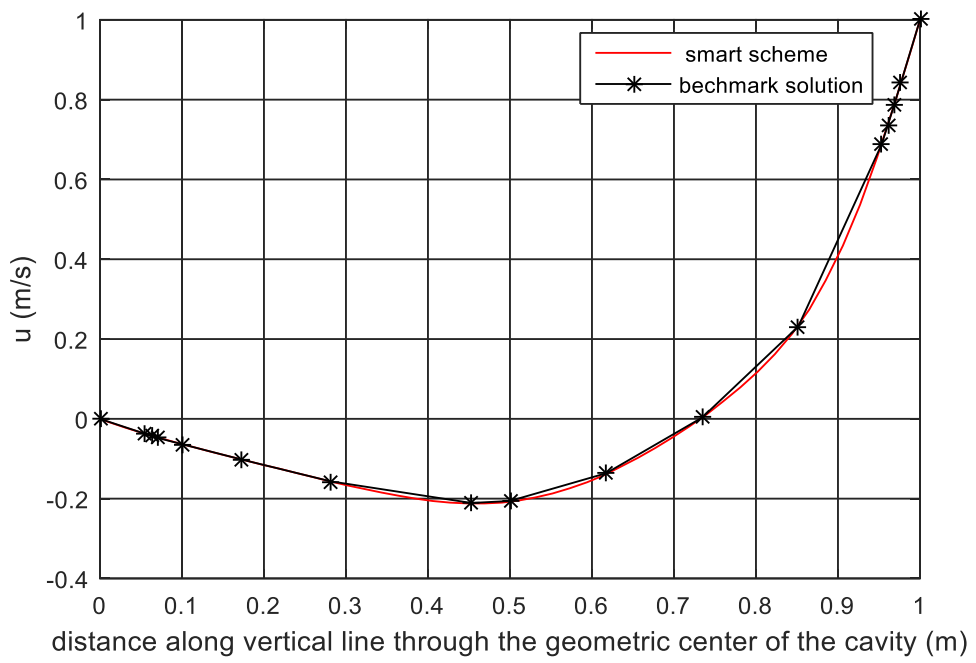


Figure 5.6: Comparison of u velocity with Benchmark solution for $Re=100$ (mesh 50*50)

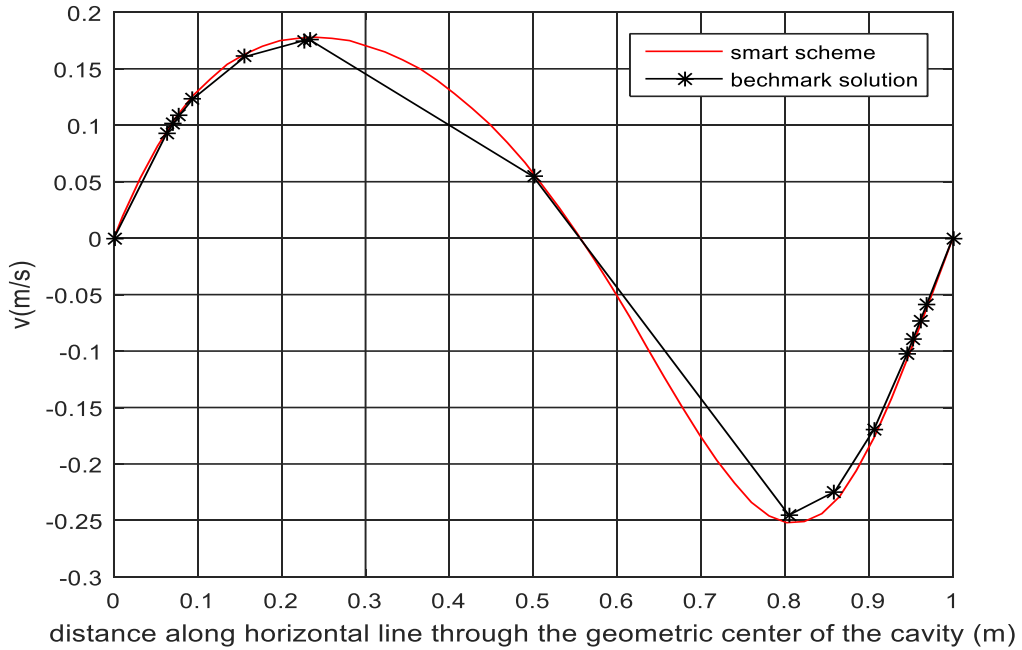


Figure 5.7: Comparison of v velocity with Benchmark solution for $Re=100$ (mesh 50*50)

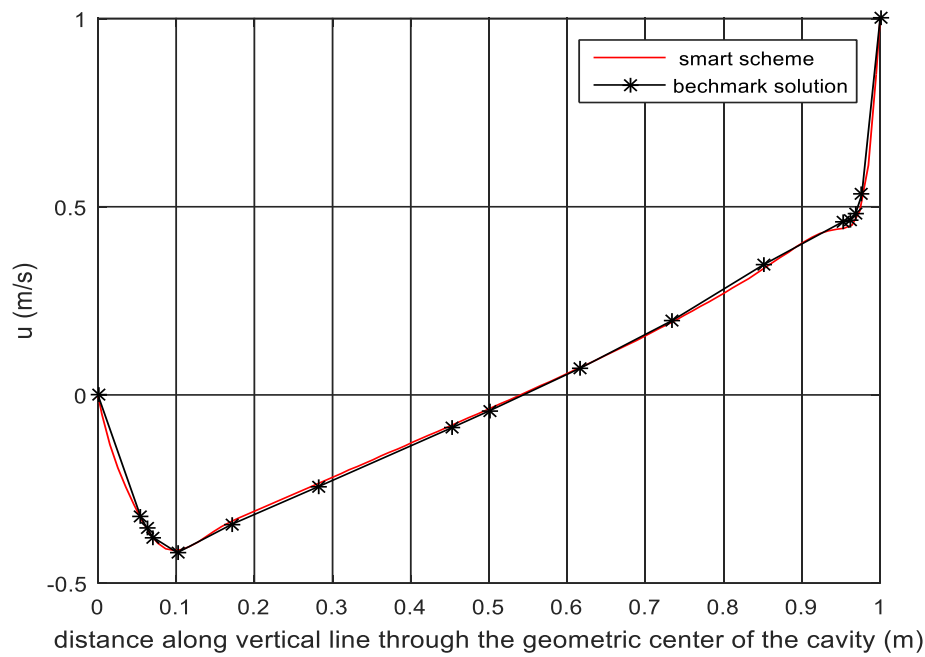


Figure 5.8: Comparison of u velocity with Benchmark solution for $Re=3200$ (mesh 100*100)

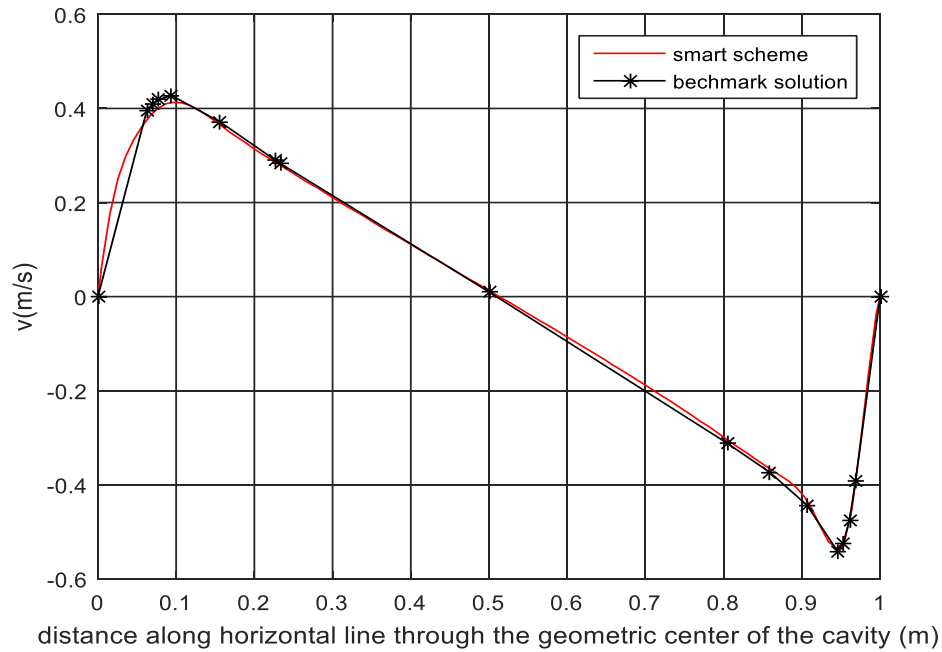


Figure 5.9: Comparison of v velocity with Benchmark solution for $Re=3200$ (mesh 100*100)

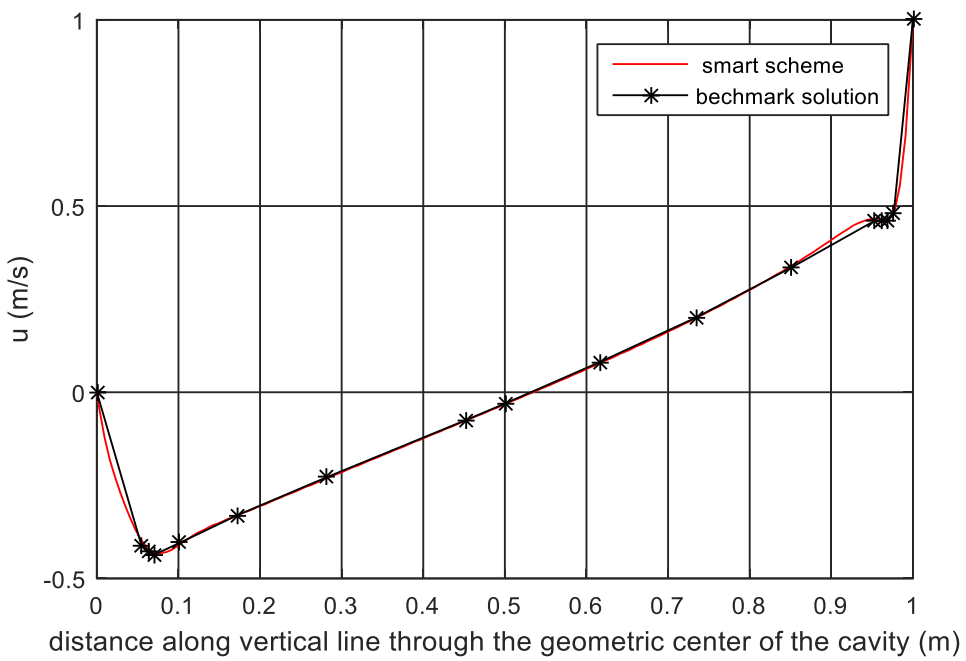


Figure 5.10: Comparison of u velocity with Benchmark solution for $Re=5000$ (mesh 160*160)

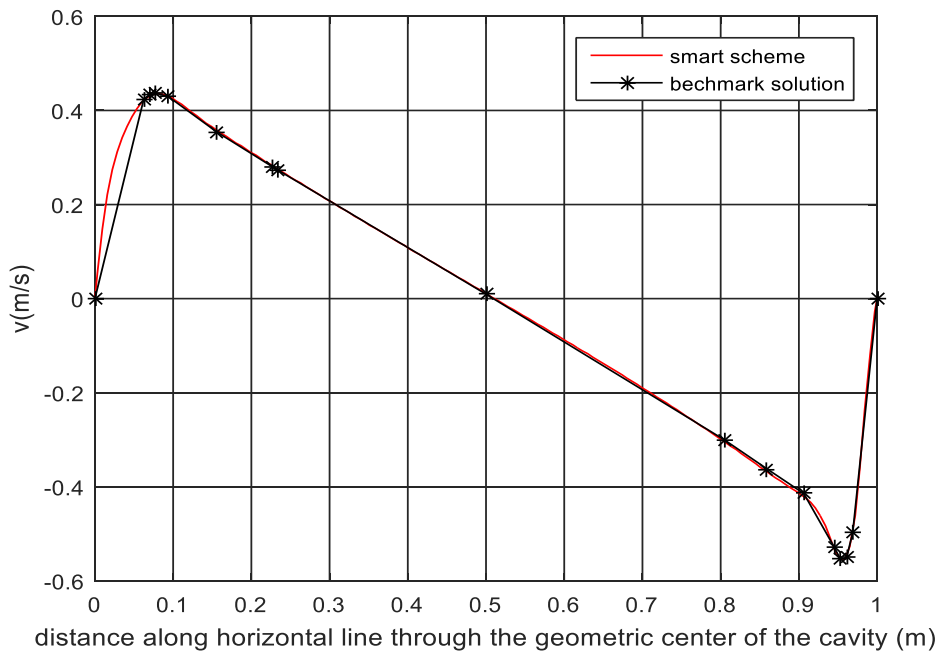


Figure 5.11: Comparison of v velocity with Benchmark solution for $Re=5000$ (mesh 160*160)

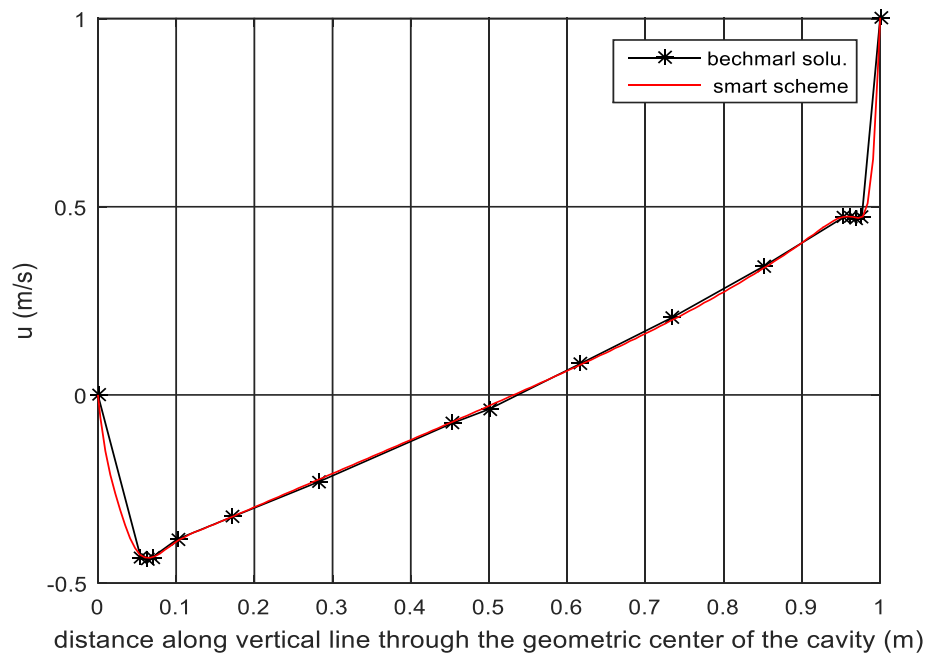


Figure 5.12: Comparison of u velocity with Benchmark solution for $Re=7500$ (mesh 160*160)

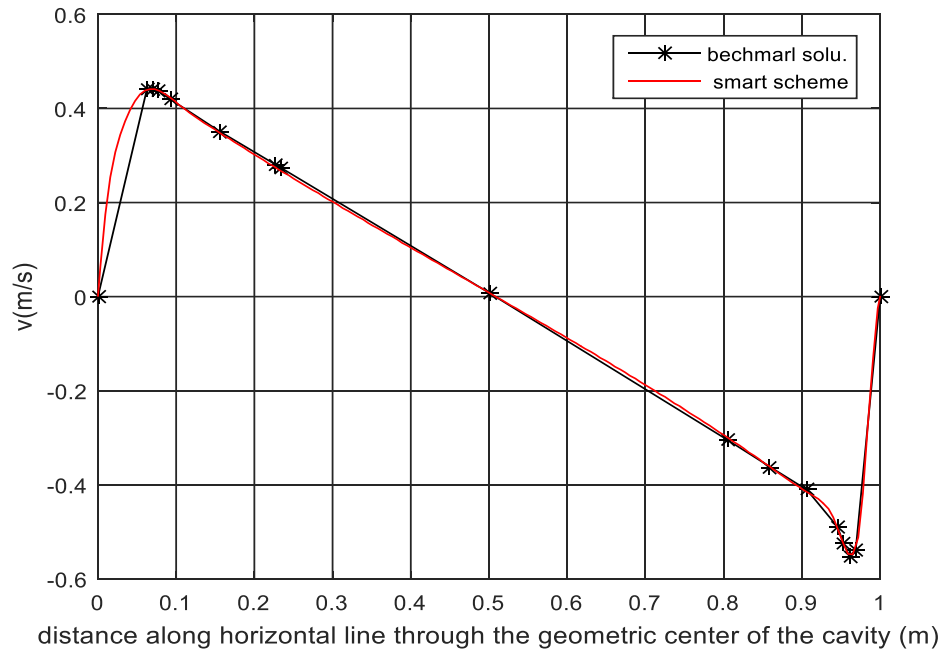


Figure 5.13: Comparison of v velocity with Benchmark solution for $Re=7500$ (mesh 160*160)

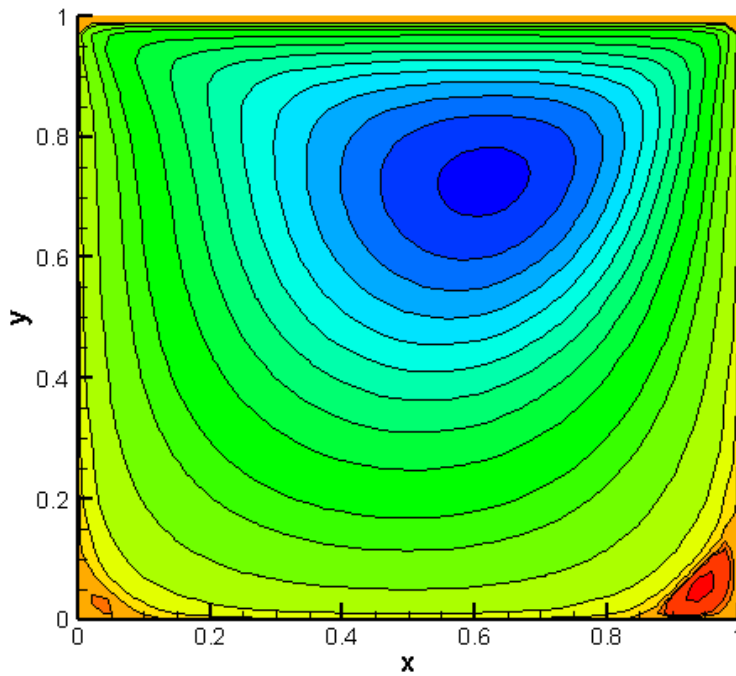


Figure 5.14: Streamlines for $Re=100$ (mesh 50*50)

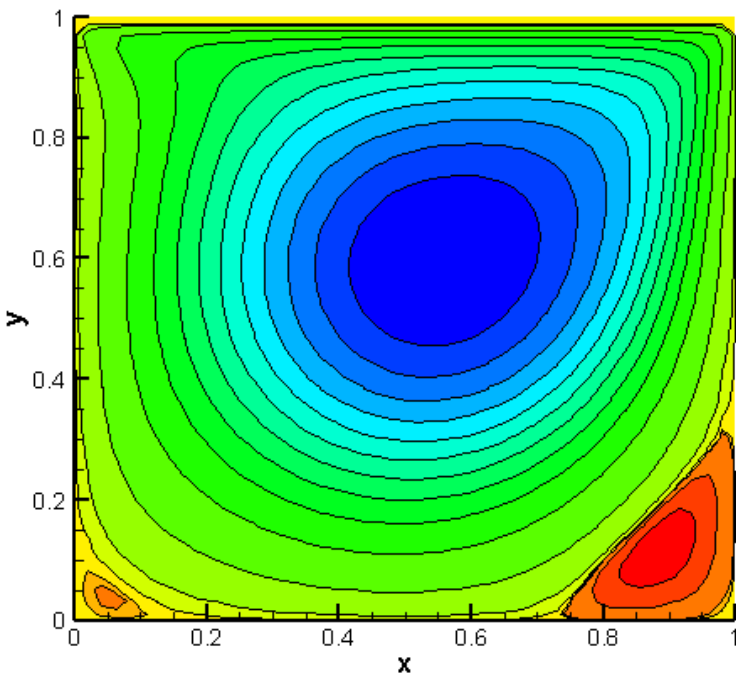


Figure 5.15: Streamlines for $Re=400$ (mesh 50*50)

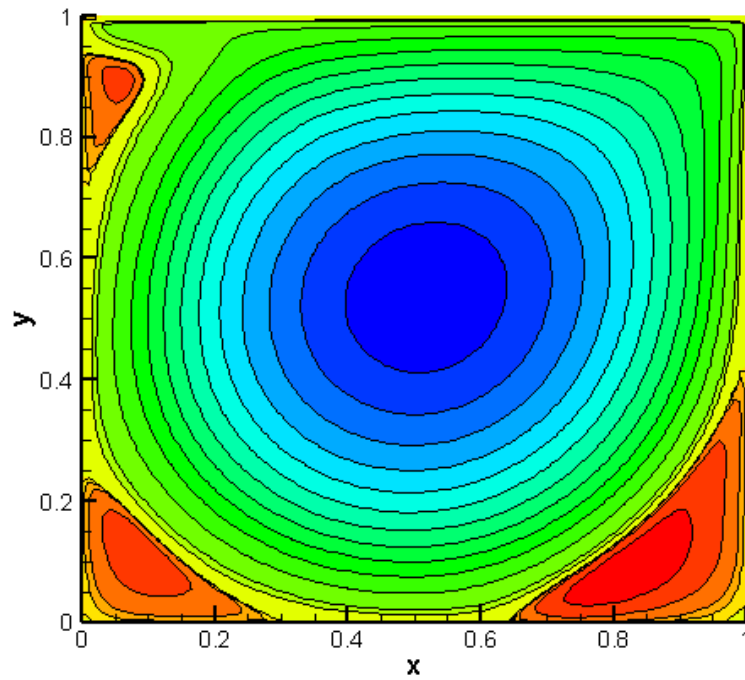


Figure 5.16: Streamlines for $Re=3200$ (mesh 100*100)

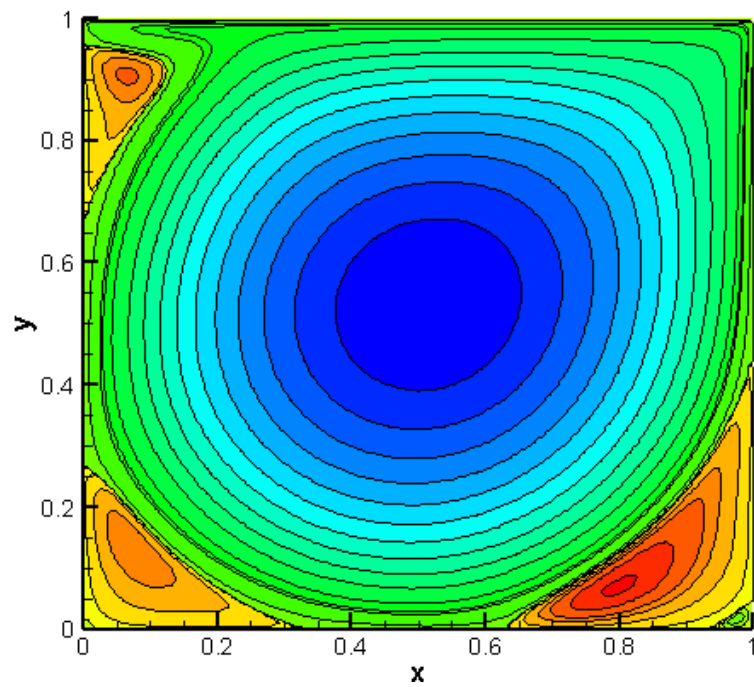


Figure 5.17: Streamlines for $Re=5000$ (mesh 160*160)

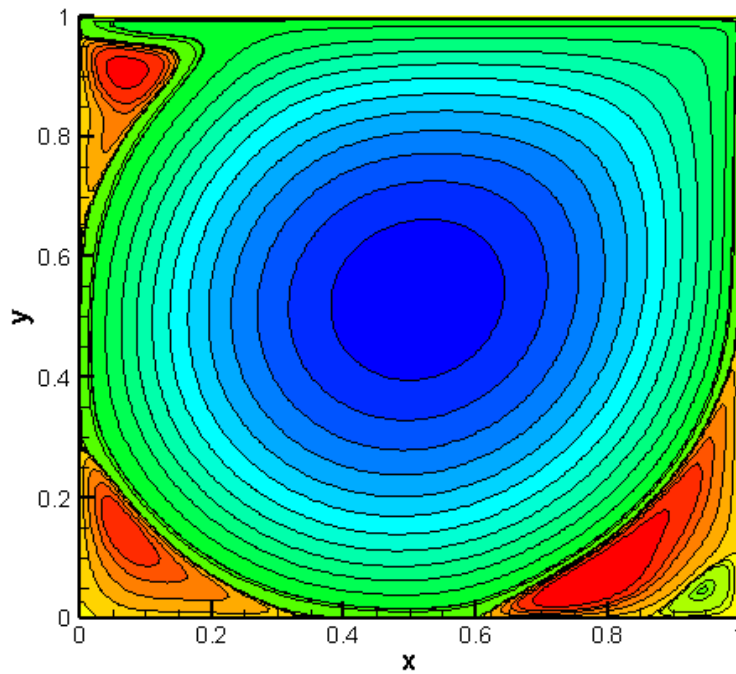


Figure 5.18: Streamlines for $Re=7500$ (mesh160*160)

5.2.1.4 Results discussion

From the previous figures, it is clearly seen that there is good match between computed results and reference values for different Reynolds number. Also, finer mesh is required for high Reynolds number in order to obtain accurate results. It is observed that, upper left secondary vortex appears in high Reynolds numbers (3200, 5000, and 7000) as shown in Figure 5.16, Figure 5.17 and Figure 5.18 .

5.2.2 Differentially heated square cavity

5.2.2.1 Problem Description

Two dimensional flow of Bossinseq fluid of Prandtl number 0.71 in an upright square cavity of side length L. Bossinseq approximation for natural convection will be used in momentum equation in y-direction .Both velocity components are zero on the boundaries. The horizontal wall are insulated, and the vertical sides are at temperatures; high temperature T_h and cold temperature T_c .The velocities and temperature will be solved for different Rayleigh numbers of $10^3, 10^4, 10^5$ and 10^6 .

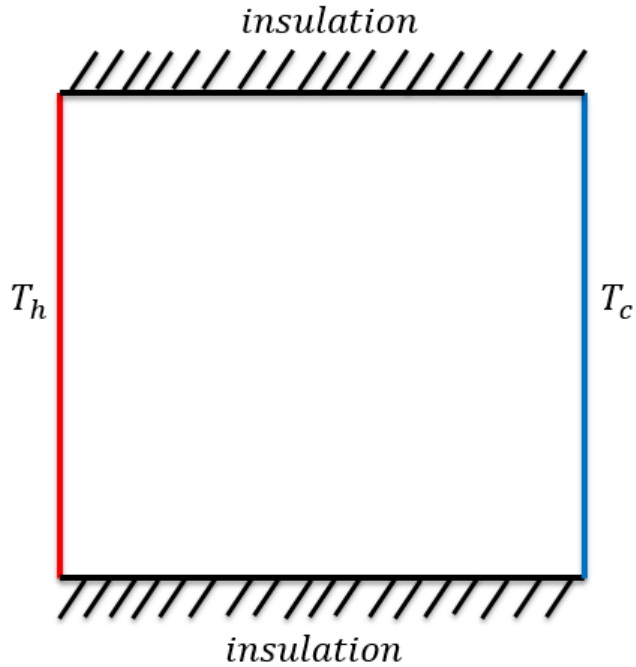


Figure 5.19: Problem description

5.2.2.2 Boundary conditions

For the velocity, no slip boundary condition is applied on the walls ($u = v = 0$). For the pressure, zero Neumann boundary condition in normal direction to the wall is applied for the four wall $\frac{\partial p}{\partial n} = 0$. For solving the pressure linear solver is used like TDMA or Gauss-Seidal which will have infinite number of solution if zero Neumann boundary condition is used for all the walls. In order to avoid this problem, the pressure has to be set to reasonable value at any point in the solution domain. For the temperature, Dirichlet boundary condition is used for the left and right wall T_h and T_c respectively. Zero Neumann boundary condition is used for the top and bottom wall.

5.2.2.3 Results

This case will be solved for different Rayleigh numbers of $10^3, 10^4, 10^5$ and 10^6 . The solution will be compared to Benchmark solution [18]. For the convective term central and smart scheme will be tested. For comparing results with the Benchmark solution, the value of the average Nusselt number will be computed at the left wall (Nu_0), right wall (Nu_1) and in the middle plane of the cavity ($Nu_{1/2}$). Also, local maximum and minimum Nusselt

number Nu_{max} , Nu_{min} will be calculated at the left wall. The maximum velocity in x-direction along vertical line passing through the middle of the cavity ($u_{max}(x = 0.5)$) and the maximum of the velocity in y-direction along horizontal line passing through the middle of the cavity($v_{max}(z = 0.5)$) will be calculated and compared to reference values. Also the value of streamline function in the middle of the cavity (Ψ_{mid}) and the value of maximum streamline function (Ψ_{max}) and its location will be calculated.

Ra=10 ³							
	Reference value	Central scheme		Smart scheme			
		uniform mesh (50*50)	Error %	Hyperbolic mesh (k=0.5) (50*50)	Error %	Hyperbolic mesh (k=2) (50*50)	Error %
$ \Psi_{mid} $	1.174	1.1815	0.638	1.1813	0.621	1.1765	0.212
$u_{max}(x=0.5)$	3.649	3.663	0.383	3.674	0.685	3.676	0.739
z	0.813	0.8229	1.217	0.8172	0.516	0.8158	0.344
$v_{max}(z=0.5)$	3.697	3.721	0.649	3.722	0.676	3.726	0.784
x	0.178	0.1771	-0.505	0.1828	2.696	0.1842	3.483
$Nu_{1/2}$	1.118	1.1195	0.134	1.11971	0.152	1.11809	0.008
Nu_0	1.117	1.11953	0.226	1.11993	0.262	1.12286	0.524
Nu_1		1.11942		1.11979		1.11534	
$Nu_{max}(x=0)$	1.505	1.51264	0.507	1.51291	0.525	1.51391	0.592
z	0.092	0.0937500	1.902	0.0831702	-9.597	0.0964778	4.867
$Nu_{min}(x=0)$	0.692	0.689055	-0.425	0.689268	-0.394	0.693346	0.194
z	1	1	0	1	1	1	0

Table 5.4: comparison between Benchmark solution and code solution at Ra=10³

The temperature, velocity and streamlines contours will be plotted as shown in the following figures Figure 5.20, Figure 5.21, Figure 5.22, and Figure 5.23.

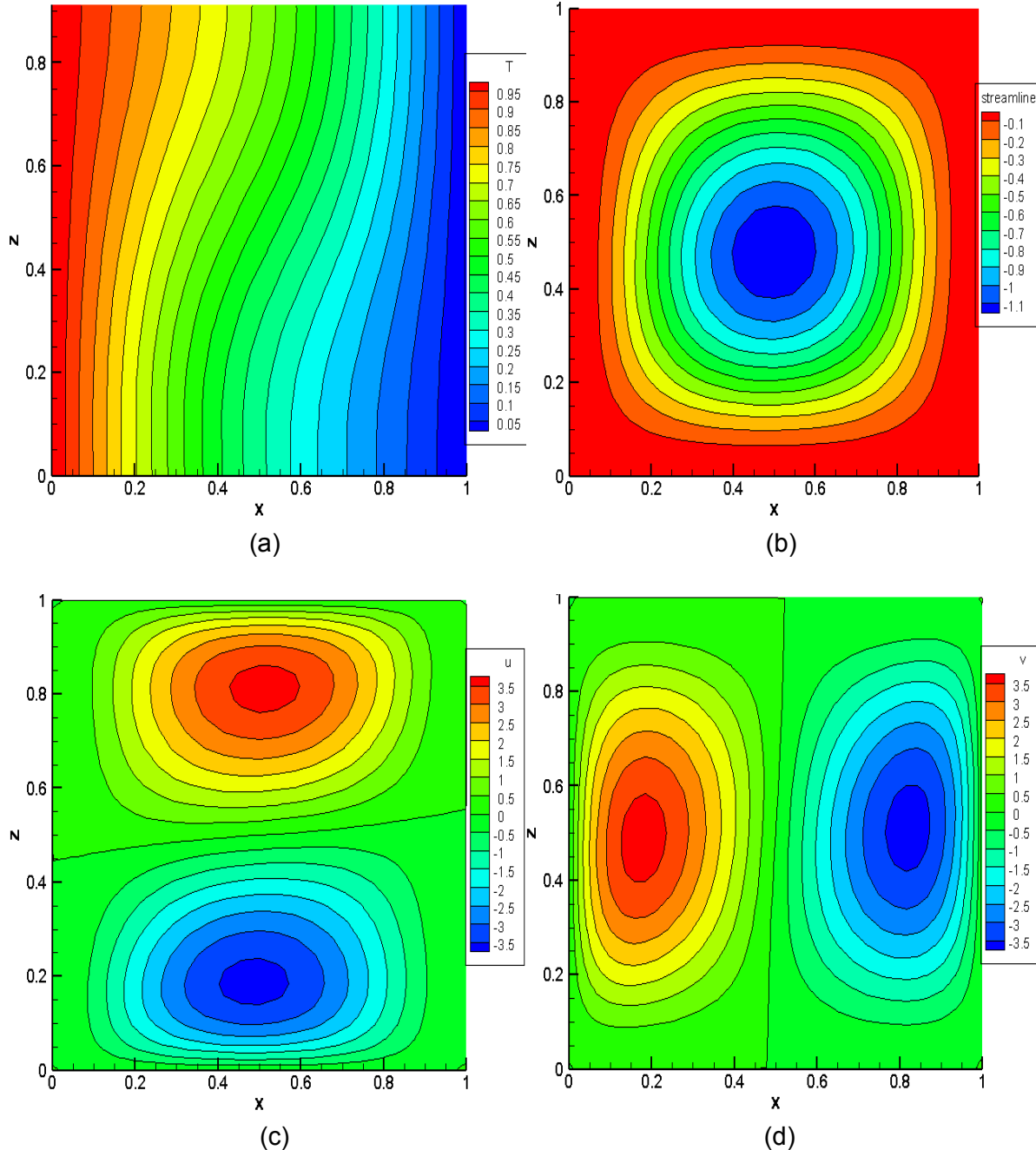


Figure 5.20: contours of (a) temperature, (b) streamline function, (c) u velocity,(d) v velocity at $Ra=10^3$

Ra=10 ⁴			
	Reference value	Central scheme	
		uniform mesh (50*50)	Error %
Ψ_{mid}	5.071	5.064	-0.138
$u_{max}(x=0.5)$	16.178	16.16	-0.111
z	0.823	0.8229	-0.012
$v_{max}(z=0.5)$	19.617	19.6	-0.087
x	0.119	0.1146	-3.697
$Nu_{1/2}$	2.243	2.24757	0.204
Nu_0	2.238	2.24785	0.440
Nu_1		2.24766	
$Nu_{max}(x=0)$	3.528	3.55709	0.825
z	0.143	0.135417	-5.303
$Nu_{min}(x=0)$	0.586	0.581915	-0.697
z	1	1	0.000

 Table 5.5: Comparison between Benchmark solution and code solution at Ra=10⁴

Ra=10 ⁵					
	Reference value	Central scheme			
		uniform mesh (50*50)	Error %	uniform mesh (100*100)	Error %
Ψ_{mid}	9.111	9.111	0	9.13	0.2085
Ψ _{max}	9.612	9.617	0.05201	9.6324	0.2122
X,Z	0.285,0.601	0.2917,0.5938	2.35,1.198	0.286,0.597	0.350,-0.665
$u_{max}(x=0.5)$	34.73	34.44	0.835	34.7559	0.0745
z	0.855	0.8646	1.122	0.852	-0.3508
$v_{max}(z=0.5)$	68.59	67.72	1.268	68.6966	0.1554
x	0.066	0.07292	10.484	0.0663	0.4545
$Nu_{1/2}$	4.519	4.53846	0.430	4.53880	0.438
Nu_0	4.509	4.53843	0.652	4.53910	0.667
Nu_1		4.53848		4.53871	
$Nu_{max}(x=0)$	7.717	7.97948	3.401	7.80216	1.1035
z	0.081	0.0729167	9.979	0.0765306	-5.517
$Nu_{min}(x=0)$	0.729	0.712392	2.278	0.726843	-0.2958
z	1	1	0	1	0

 Table 5.6: Comparison between Benchmark solution and code solution at Ra=10⁵

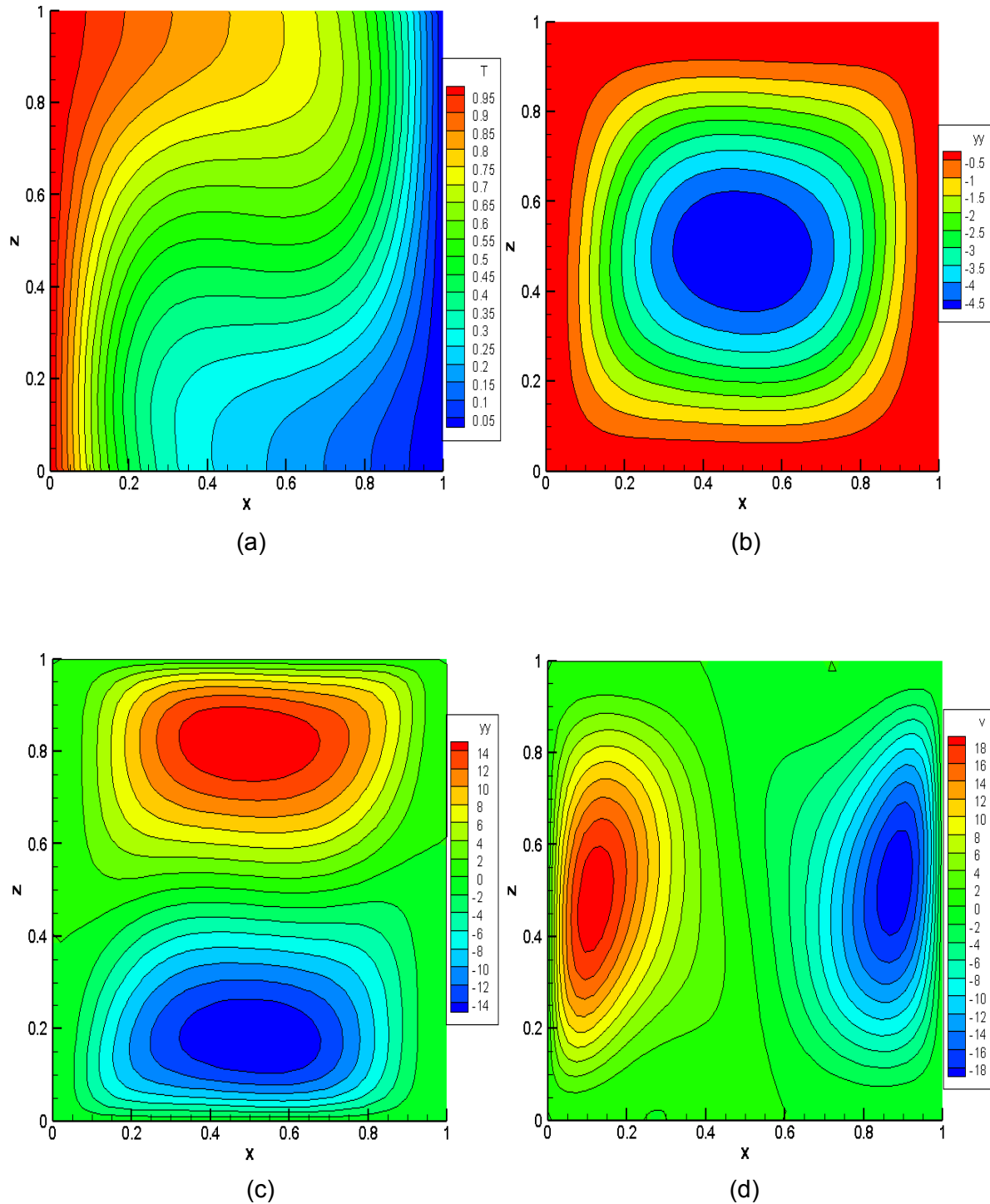


Figure 5.21: contours of (a) temperature, (b) streamline function, (c) u velocity, (d) v velocity at $Ra=10^4$

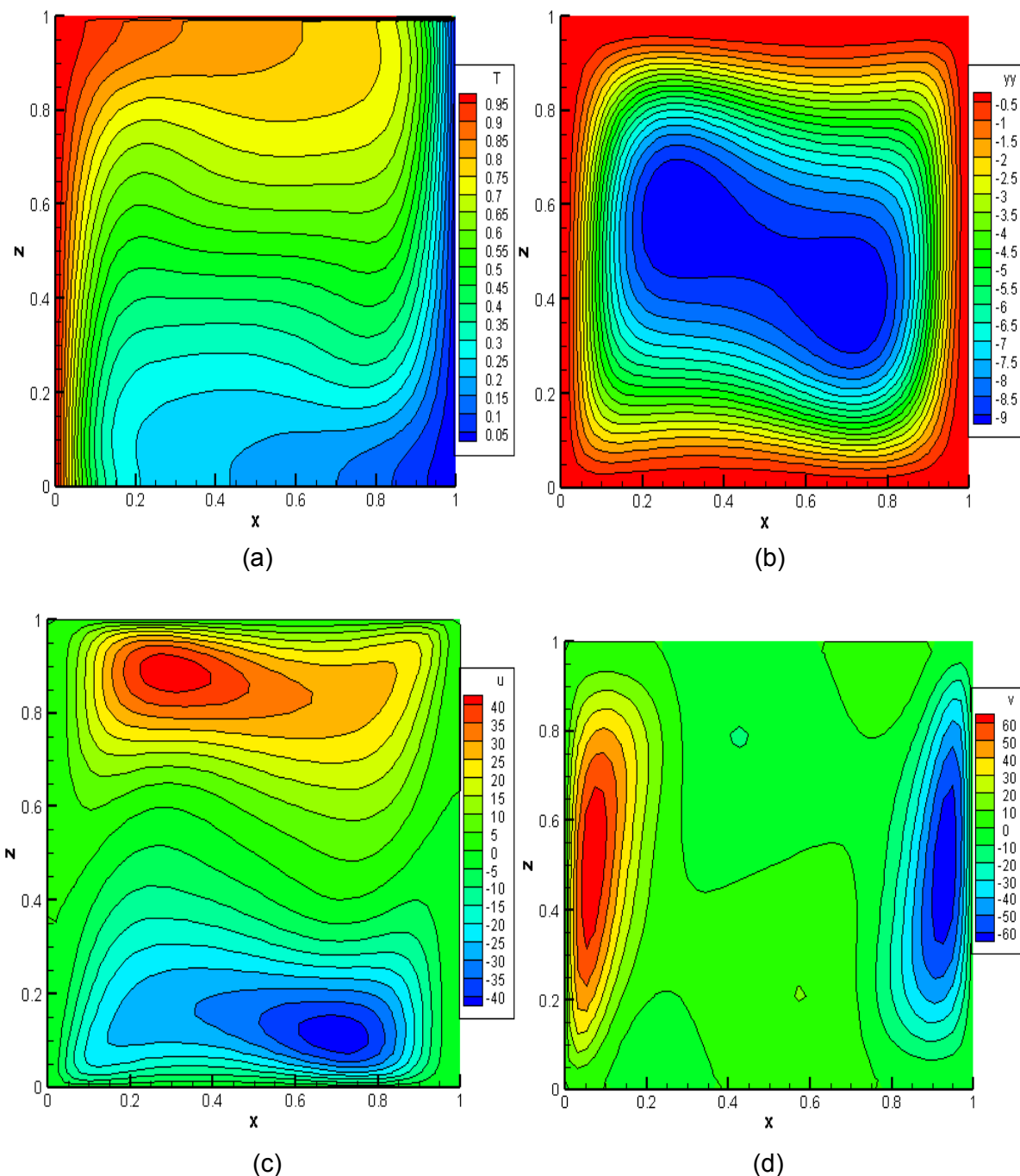


Figure 5.22: contours of (a) temperature, (b) streamline function, (c) u velocity, (d) v velocity at $Ra=10^5$

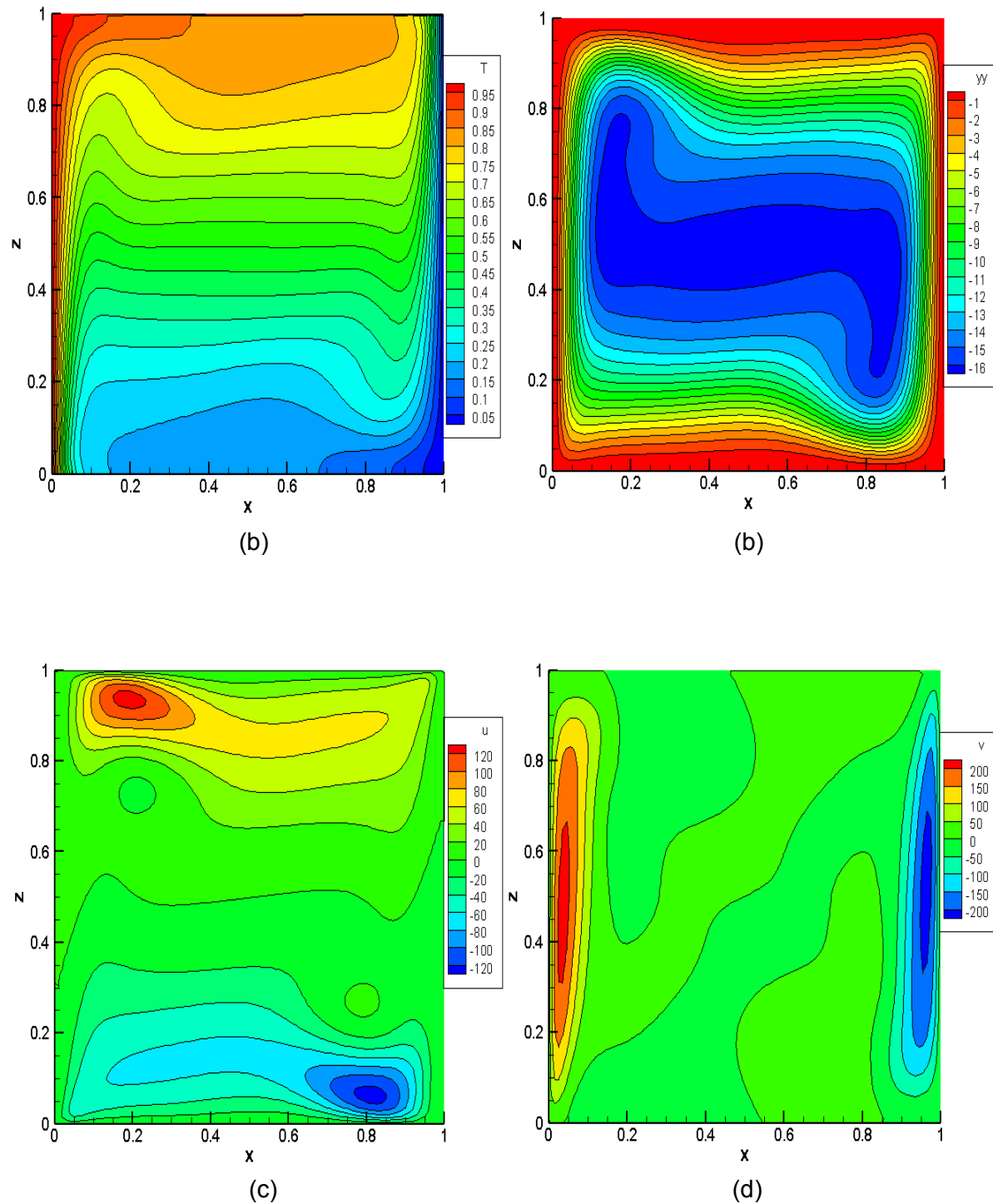


Figure 5.23: contours of (a) temperature, (b) streamline function, (c) u velocity, (d) v velocity at $Ra=10^6$

Ra=10 ⁶									
	Ref. value	Uniform mesh(50*50)		Uniform mesh(100*100)		hyperbolic k=2 mesh(50*50)			
		Central scheme	Error %	Central scheme	Error %	Central scheme	Error %	Smart scheme	Error %
Ψ_{mid}	16.32	16.425	0.643	16.385	0.398	16.345	0.153	16.34	0.123
Ψ_{max}	16.750	16.88	0.776	16.82	0.417	16.81	0.358	16.79	0.239
X,Z	0.151 ,0.547	0.1458, 0.5313	3.44, 2.87	0.1513, 0.5357	0.198, 2.06	0.1461, 0.5216	3.245, 4.644	0.1461, 0.5216	3.24, 4.644
u_{max} (x=0.5)	64.63	63.58	1.624	63.88	1.1604	64.32	0.480	64.4	0.356
Z	0.850	0.8438	0.729	0.8418	0.964	0.8648	1.741	0.8416	0.988
v_{max} (z=0.5)	219.36	216.8	1.167	219.6	0.109	220.5	0.52	220.3	0.429
x	0.0379	0.0312	17.54	0.03571	5.77	0.03475	8.311	0.0347	8.311
Nu _{1/2}	8.799	8.9284	1.470	8.84405	0.511	8.82753	0.324	8.8167	0.202
Nu ₀	8.817	8.9285	1.264	8.84428	0.309	8.82956	0.142	8.8240	0.080
Nu ₁		8.9284		8.84393		8.82583		8.8202	
Nu _{max} (x=0)	17.925	19.613	9.420	18.2285	1.693	17.6515	1.526	17.604	1.790
Z	0.0378	0.0312	17.32	0.03571	5.517	0.03475	8.065	0.0347	8.065
Nu _{min} (x=0)	0.989	0.9030	8.693	0.95931	3.002	0.98832	0.068	0.9794	0.969
z	1	1	0	1	0	1	0	1	0

Table 5.7: Comparison between Benchmark solution and code solution at Ra=10⁶

5.2.2.4 Results discussion

From comparison Table 5.4, Table 5.5, Table 5.6, and Table 5.7 , it can be concluded that the maximum percentage of error is less than 1% for all the values, but for the location of the values, the maximum error percentage is less than 9%. The reason for this error might be the different mesh size used in the Benchmark solution compared to the present solution. Smart scheme slightly decrease error compared to central scheme. Moreover the use of concentrated mesh near the wall especially for high Rayleigh number 10⁶ improve error percentage compared to uniform mesh because at high Rayleigh number the gradient of the physical properties is very high near the walls.

In this chapter, Analytical and benchmark solutions are used to verify the code. The code shows that it has good agreement with the benchmarks solution for driven square cavity, and differentially heated cavity. Also the program accuracy order is similar to the convective

scheme order as shown in Method of Manufactured solution (MMS), and error between analytical and numerical solution decreases with increasing number of control volume. It can be concluded that, the develop code our code is reliable and can be used for simulating our case study, which will be discussed in the next chapter.

6 Case study: laminar flow around square cylinder

In this chapter after validating the code that is used to solve Navier-Stokes equation using Method of Manufactured and comparing our code solution to the solution of Benchmark problem. Here the code is used to simulate laminar flow over square cylinder Figure 6.1 and to find aerodynamic forces, pressure distribution, force coefficients, vortex shedding, flow patterns, Nusselt number of the boundaries of the square cylinder with the fluid and Strouhal number. Flow over square cylinder case is chosen because of its dominant role in many applications such as building aerodynamics and heat exchangers.

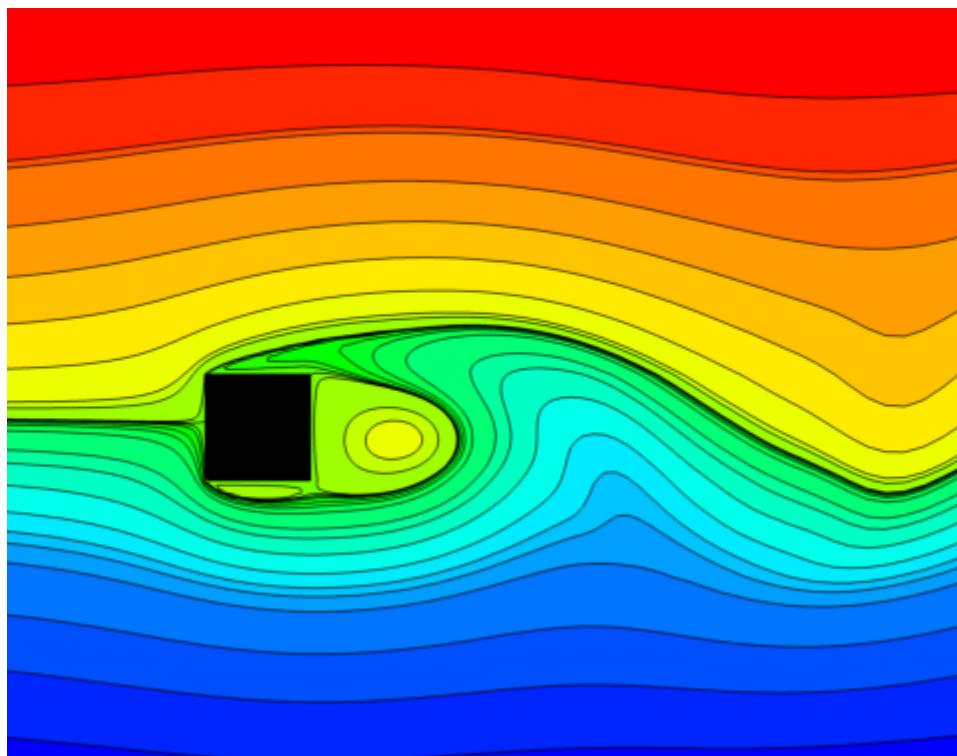


Figure 6.1: Laminar flow over square cylinder

In this chapter, the effect of changing Reynolds number of the flow over the square cylinder will be investigated for fixed blockage ratio. Also, the effect of blockage ratio will be studied for different Reynolds number. Then, tandem arrangement of two square cylinders will be studied. Finally the effect of thermal buoyancy on flow pattern and different calculated quantities will be investigated for the tandem arrangement.

6.1 The effect of changing Reynolds number for fixed blockage ratio

In this section the effect of changing of Reynolds number on confined square cylinder will be investigated for fixed blockage ratio of 12.5%. Force coefficients and vortex shedding frequency will be calculated for different Reynolds number and compared with previous work [19].

6.1.1 Geometry of the computational domain and mesh

In this case the square cylinder with diameter D is mounted inside a plane channel of height H . The blockage ratio is fixed ($B = \frac{D}{H} = \frac{1}{8}$) . In order to reduce the effect of inflow and of outflow boundary condition, the length of the channel was set to ($L/D = 50$) and inflow length of ($l = L/4$) as recommended by Breuer [19]. The geometry of computational domain is shown in Figure 6.2 .

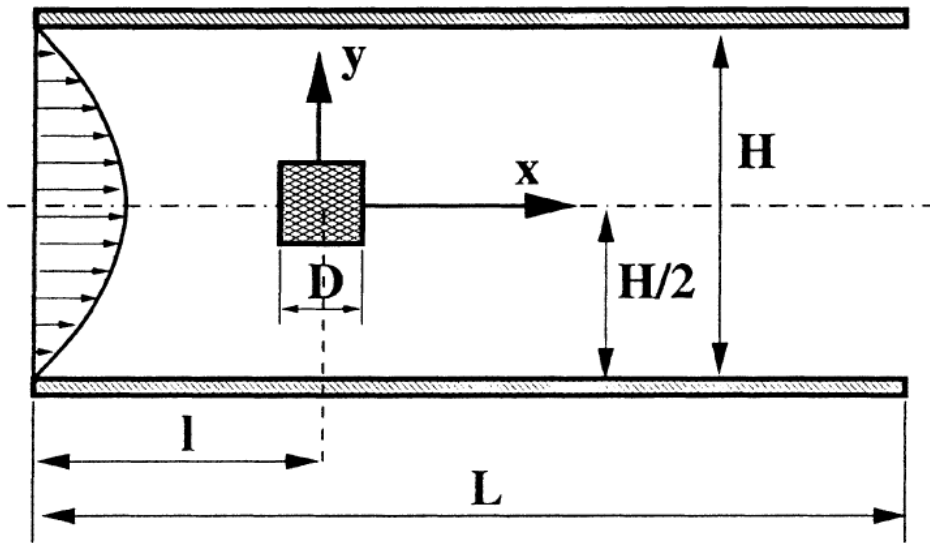


Figure 6.2: Geometry of computational domain[19]

Mesh

To get more accurate results, concentrated mesh is used in region of interest around the square cylinder. In x-direction the mesh is divided into three parts; first part is from inlet to the left wall of the square with length(L_1), second part is from left wall of the square to the right side of the square with length(L_2), and the third part is from the right side of the square till the outlet of the channel with length(L_3). In the first part hyperbolic mesh is used with

concentration factor of 2 Eq.(6.1) in which the mesh is more concentrated near the right wall of the square. In the second part, symmetrical concentrated hyperbolic mesh with low concentration factor of 1 Eq.(6.2) is used. In the third part, hyperbolic mesh with concentration factor of 2 Eq.(6.3) is utilized in which the mesh is more concentrated near the right wall of the square cylinder. Similar procedures are used for the mesh in y-direction. The used mesh is shown in Figure 6.3. Two meshes are used in this case 184*66, and 236*90.

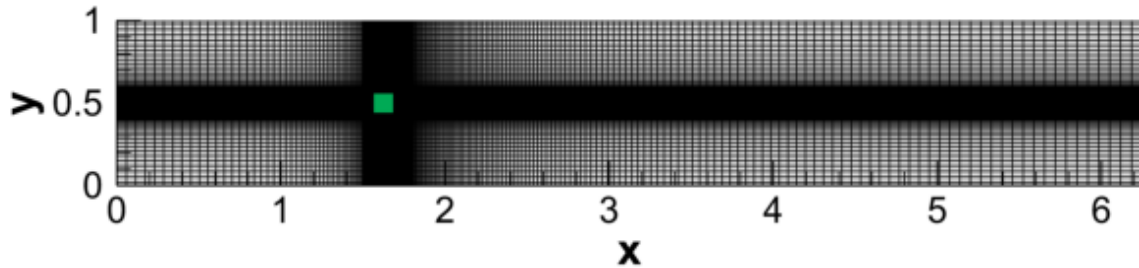


Figure 6.3: Mesh used in square cylinder case

$$x = -L_1 + L_1 * \left(1 + \frac{\tanh\left(\frac{k_1 * (i - 1 + N_1)}{N_1} - k_1\right)}{\tanh k_1} \right) \quad (6.1)$$

$$x = L_1 + \frac{L_2}{2} * \left(1 + \frac{\tanh\left(\frac{2 * k_2 * (i - 1)}{N_2} - k_2\right)}{\tanh k_2} \right) \quad (6.2)$$

$$x = (L_1 + L_2) + L_3 * \left(1 + \frac{\tanh\left(\frac{k_3 * (i - 1)}{N_3} - k_3\right)}{\tanh k_3} \right) \quad (6.3)$$

Where;

K: grid concentration factor.

N: number of control volumes.

6.1.2 Boundary conditions

In this section, the boundary conditions used in the inlet, outlet, walls of the square, and the walls of the channel will be discussed.

6.1.2.1 Inlet boundary conditions

In order to simulate fully development laminar flow around the square cylinder, a parabolic velocity profile with maximum velocity u_{max} is used at the inlet of the channel for the velocity in x-direction Eq.(6.4). The component of the velocity in y-direction is set to zero ($v = 0$).

$$u = u_{max} * \left(1 - \left(1 - \left(\frac{2y}{H} \right)^2 \right) \right) \quad (6.4)$$

For the pressure at the inlet of the channel, Neumann boundary condition is utilized Eq.(6.5).

$$\frac{\partial p}{\partial x} = 0 \quad (6.5)$$

6.1.2.2 Outlet boundary condition

At the outlet Neumann boundary condition is used for the velocity Eq.(6.6)

$$\frac{\partial u}{\partial x} = \frac{\partial v}{\partial x} = 0 \quad (6.6)$$

Dirichlet boundary condition is used for the pressure at the outlet Eq.(6.7)

$$p = 0 \quad (6.7)$$

6.1.2.3 Channel wall boundary conditions

No slip boundary condition will be used for the velocity at the top and bottom wall of the channel Eq.(6.8).

$$u = v = 0 \quad (6.8)$$

For the pressure boundary condition at the channel wall, zero Neumann boundary condition is utilized Eq.(6.9).

$$\frac{\partial p}{\partial y} = 0 \quad (6.9)$$

6.1.2.4 Square cylinder wall

No slip boundary condition is used for the walls of the square cylinder Eq.(6.10).

$$u = v = 0 \quad (6.10)$$

For the pressure boundary conditions at the square wall, zero Neumann boundary condition is used in direction normal to the square walls is utilized Eq.(6.11).

$$\frac{\partial p}{\partial n} = 0 \quad (6.11)$$

6.1.3 Results

In this section the flow is investigated for Reynolds number range $1 \leq Re \leq 200$. Reynolds number is based on the diameter of the square cylinder D and the maximum velocity u_{max} at inlet of the channel Eq.(6.12).

$$Re = \frac{\rho v D}{u_{max}} \quad (6.12)$$

Also, flow parameter like; the recirculation length, strouhal number and dimensionless force coefficient (lift and drag) will be calculated for different Reynolds number. Before presenting these parameter, the meaning and equation used in calculating these parameter will be discussed briefly in the following paragraphs.

Recirculation length

The flow recirculation length is the length of the flow separation bubble that is formed after the square cylinder as shown in Figure 6.4.

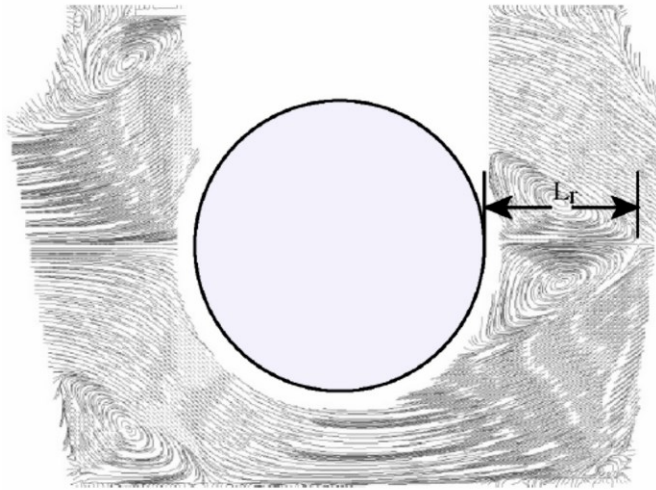


Figure 6.4: Definition of the recirculation length[20]

Drag and Lift coefficient

The drag force is the force that is acting on square cylinder in direction parallel to outcoming flow direction. While the lift force is the force acting on square cylinder in direction perpendicular to the outcoming flow direction. The force can be obtained by integrating the total stress along the body surface as shown in the following equations [21].

$$\begin{aligned}
 F_x &= - \int_s p n_x ds + \mu \int_s \left[2 \frac{\partial u}{\partial x}, \left(\frac{\partial u}{\partial y} + \frac{\partial v}{\partial x} \right) \right] \cdot \vec{n} ds \\
 &= \int_e p dy - \int_w p dy - \mu \int_w 2 \frac{\partial u}{\partial x} dy + \mu \int_e 2 \frac{\partial u}{\partial x} dy \\
 &\quad + \mu \int_n \left(\frac{\partial u}{\partial y} + \frac{\partial v}{\partial x} \right) dx - \mu \int_s \left(\frac{\partial u}{\partial y} + \frac{\partial v}{\partial x} \right) dx
 \end{aligned} \tag{6.13}$$

$$\begin{aligned}
 F_y &= \int_s p n_y ds - \mu \int_s \left[\left(\frac{\partial u}{\partial y} + \frac{\partial v}{\partial x} \right), 2 \left(\frac{\partial v}{\partial y} \right) \cdot \vec{n} ds \right] \\
 &= \int_s p dx - \int_n p dx + \mu \int_e \left(\frac{\partial u}{\partial y} + \frac{\partial v}{\partial x} \right) dy \\
 &\quad - \mu \int_w \left(\frac{\partial u}{\partial y} + \frac{\partial v}{\partial x} \right) dy + 2\mu \int_n \frac{\partial v}{\partial y} dx - 2\mu \int_s \frac{\partial v}{\partial y} dx
 \end{aligned} \tag{6.14}$$

Where;

S: body surface

\vec{n} : Unit normal vector on the body surface, positive towards the fluid ($\vec{n} = (n_x, n_y)$).

s,w,e,n: south, west ,north, and north face respectively.

In order to calculate the dimensionless aerodynamic coefficient; drag, and lift coefficient, it has to be divided $(0.5 * \rho * u_{max}^2 * D)$.

$$C_d = \frac{F_x}{(0.5 * \rho * u_{max}^2 * D)} \quad (6.15)$$

$$C_L = \frac{F_y}{(0.5 * \rho * u_{max}^2 * D)} \quad (6.16)$$

Strouhal number

The Strouhal Number is a dimensionless number used for analyzing oscillating unsteady fluid flow dynamics problems, which is calculated from Eq.(6.17).

$$St = \frac{f D}{u_{max}} \quad (6.17)$$

Where;

f : Frequency of vortex shedding

The frequency of vortex shedding f is determined by fast Fourier transform of the time series of the lift coefficient.

6.1.3.1 Steady flow

In this section steady laminar flow regimes will be analyzed for Reynolds number $1 \leq Re \leq 60$. Velocity, pressure contours and streamlines will be plotted for different Reynolds number within that range. Also the recirculation length and the drag coefficient will be calculated and compared to previous work presented by Breuer [19] .

6.1.3.1.1 Pressure, velocity, and streamlines contours

In this part the contours of pressure, velocity, and streamlines will be presented for selected Reynolds number $Re=1$ and $Re=30$.

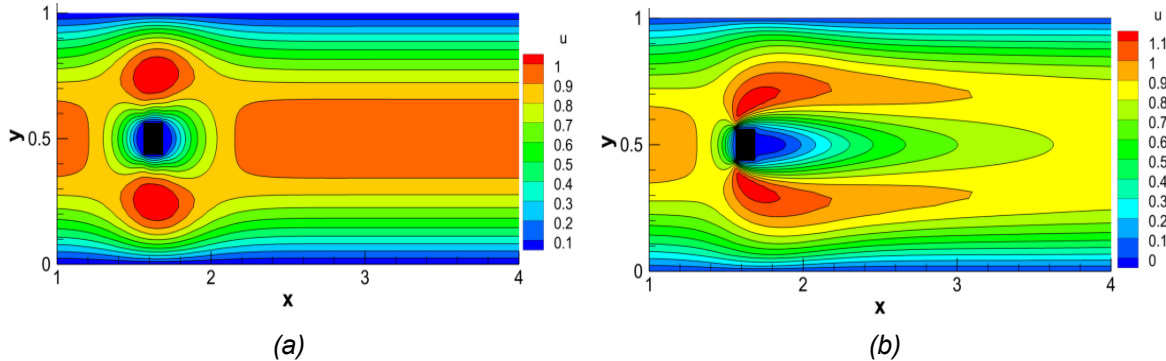


Figure 6.5: Velocity in x -direction contour for; (a) $Re=1$, and (b) $Re=30$

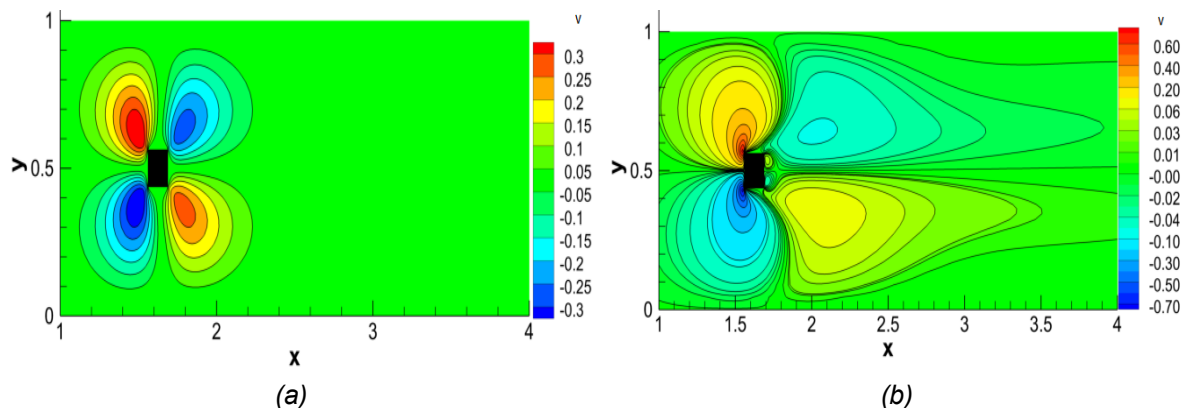


Figure 6.6: Velocity in y -direction contour for; (a) $Re=1$, and (b) $Re=30$

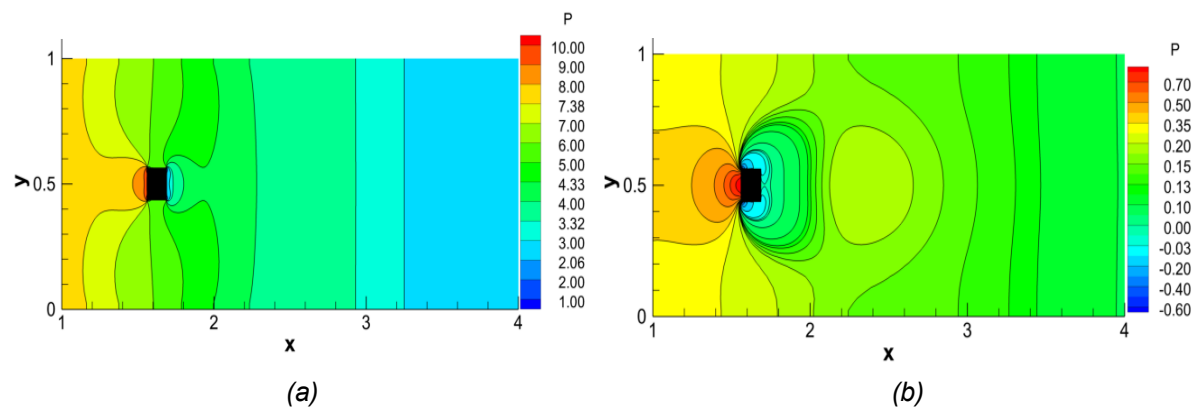


Figure 6.7: Pressure contours for; (a) $Re=1$, and (b) $Re=30$

From the velocity in x-direction contours as shown in Figure 6.5, it is clearly seen that the velocity in x-direction has parabolic profile, in which maximum velocity is in the middle of the channel inlet. Horizontal velocity decrease as it approaches the square, where it reaches zero. The velocity (u) above and below the square increase, due to the decrease of the flow area because of the presence of the square that blocks part of the flow. Also the horizontal velocity values in $Re = 30$ is higher compared to $Re=1$, because the flow is less viscous.

From the vertical velocity component (v) contours as shown in Figure 6.6. It can be seen the v contours are symmetric around $y=0.5$. Also velocity v has positive and negative values because the flow change its direction to avoid square obstacle.

Form the pressure contours as shown in Figure 6.7, pressure increase before the body and decrease after the body. Moreover, the pressure is lower in $Re=30$ compared to $Re=1$, because the flow is less viscous which will lead to lower drag coefficient.

From Figure 6.8 and Figure 6.9, it can be seen that , the streamlines plots are similar to the plots presented by Breuer[19]. Also from the plots,it can be seen that the flow pass over the square without seperation at low Reynolds number $Re=1$, but at $Re=30$ the flow remains steady with the apperance of two symmetric vortices.

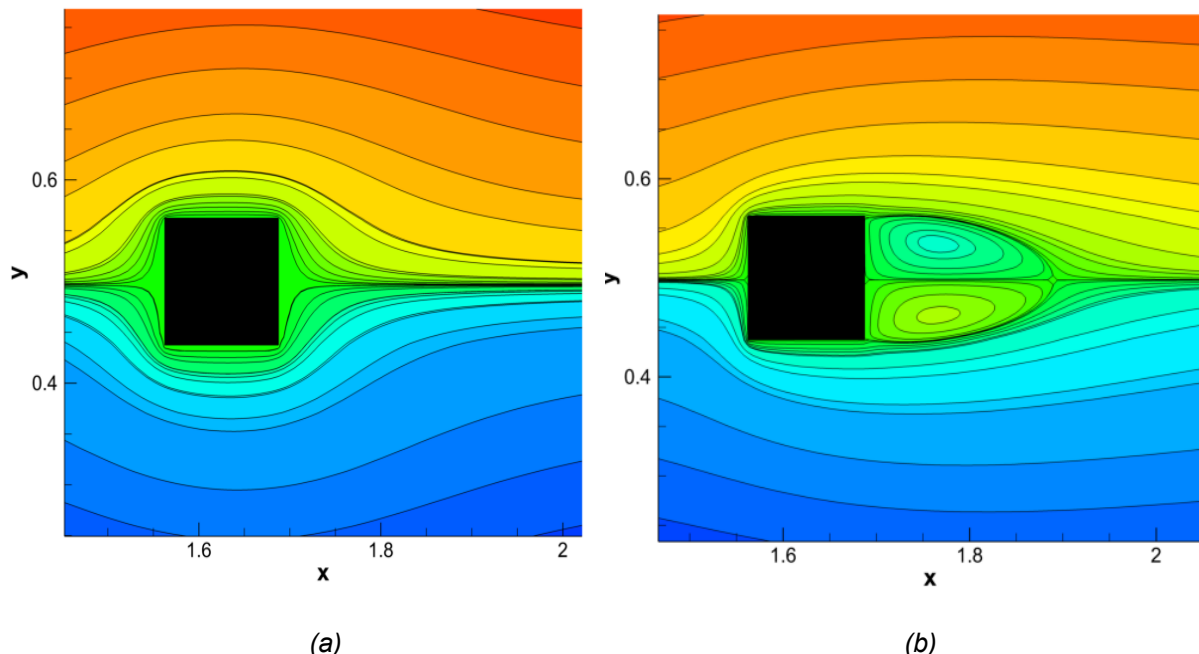


Figure 6.8: Streamlines around square cylinder for (a) $Re=1$; (b) $Re=30$

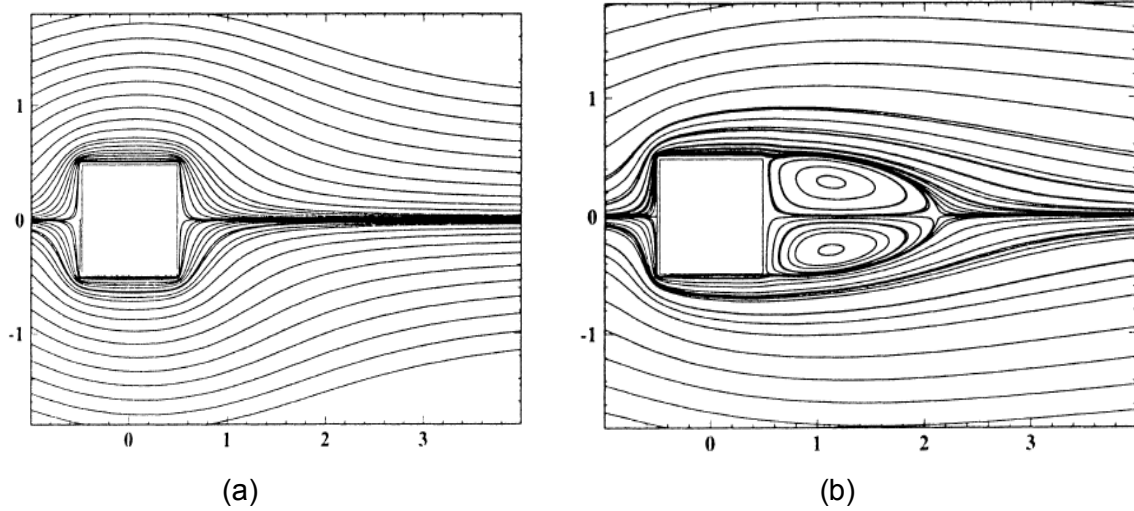


Figure 6.9: Streamlines around square cylinder for (a) $Re=1$; (b) $Re=30$ presented by Breuer [19]

6.1.3.1.2 Recirculation length

The dimensionless recirculation length (L_r/D) is calculated for laminar steady cases for $1 \leq Re \leq 60$ and compared to the result presented by Breuer [19]. From Figure 6.10, I can be concluded that recirculation length increases with increasing Reynolds number and has linear dependency on Reynolds number. Also there is good agreement between present solution and previous work.

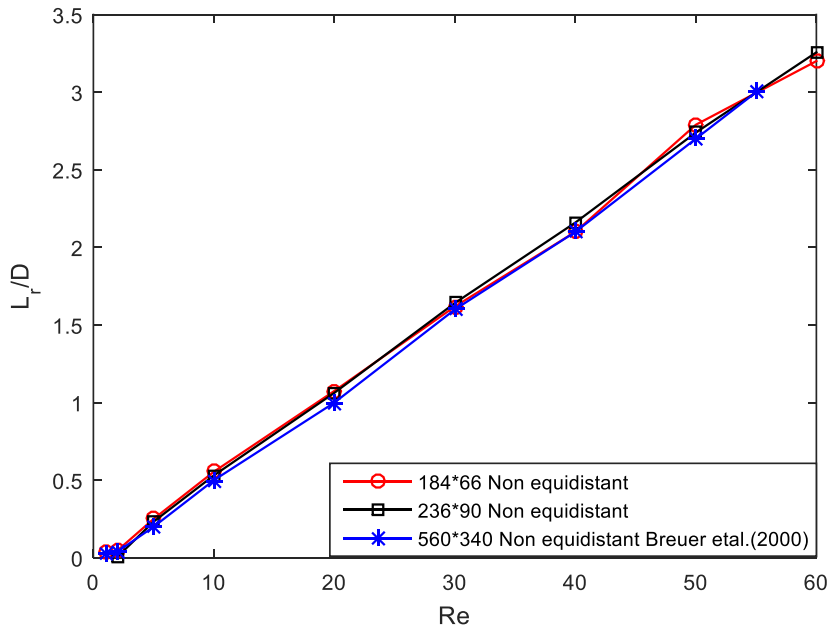


Figure 6.10: comparison of calculated recirculation length with previous work[19]

6.1.3.1.3 Drag coefficient

Drag coefficient is calculated for steady flow for Reynolds number $1 \leq Re \leq 30$ as shown in Figure 6.11(a). It can be seen that Drag coefficient decreases significantly with increasing Reynolds number. The decrease in drag coefficient is due to decrease in pressure and viscous drag. The current solution in Figure 6.11(a) follows the same trend of the solution presented by previous work in Figure 6.11(b).

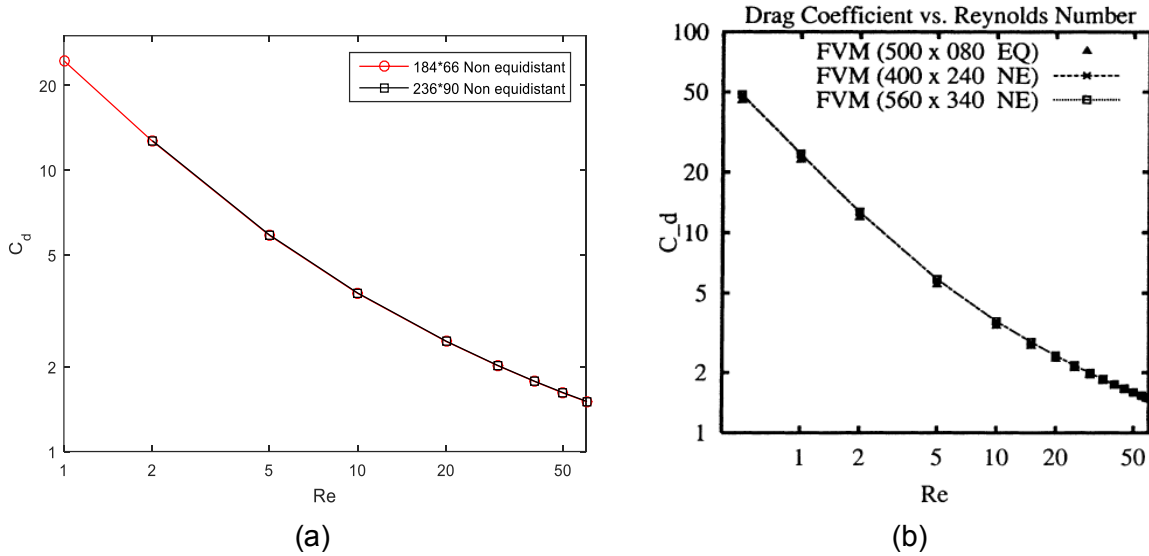


Figure 6.11: Drag coefficient: (a) calculated in present work (b) calculated by Breuer [19]

6.1.3.2 Unsteady flow

In this section, unsteady flow regime will be analyzed for Reynolds $60 < Re \leq 225$. contours plots for the pressure, velocity and streamlines will be presented. Time averaged drag and lift, difference between maximum and minimum drag coefficient ($\max(C_d) - \min(C_d)$) , and difference between maximum , minimum lift coefficient ($\max(C_L) - \min(C_L)$) and Strouhal number will be calculated and compared to previous work [19, 22].

6.1.3.2.1 Pressure, velocity, and streamlines contours

In this section the plots for streamlines, pressure and velocity will be presented for selected Reynolds number $Re = 65$, and $Re = 200$.

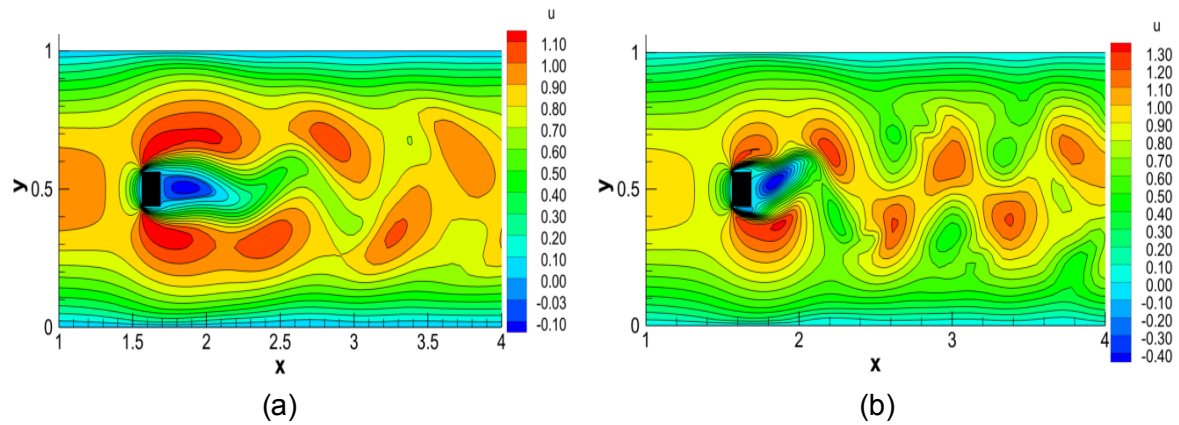


Figure 6.12: Velocity in x -direction contour for; (a) $Re=65$, and (b) $Re=200$

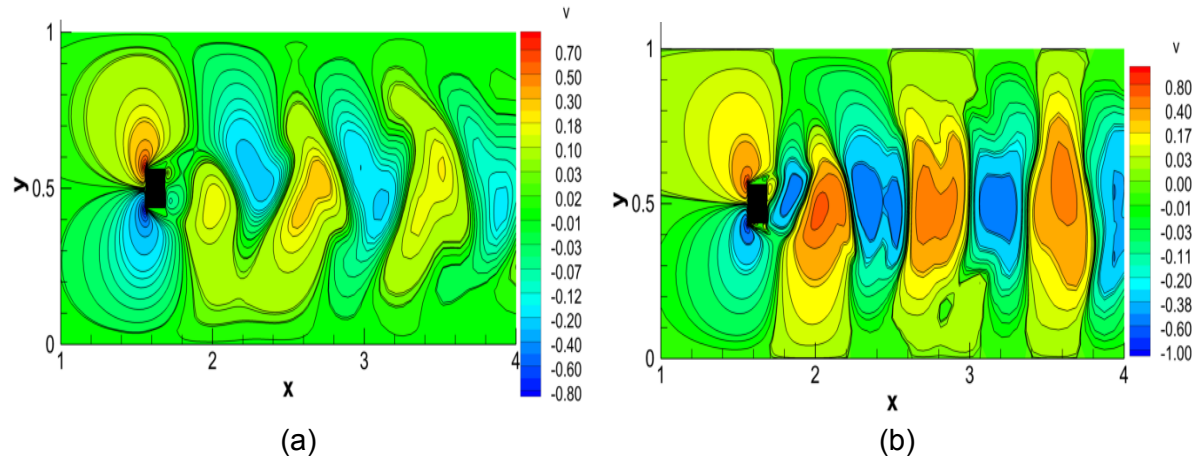


Figure 6.13: Velocity in y -direction contour for ;(a) $Re=65$, and (b) $Re=200$

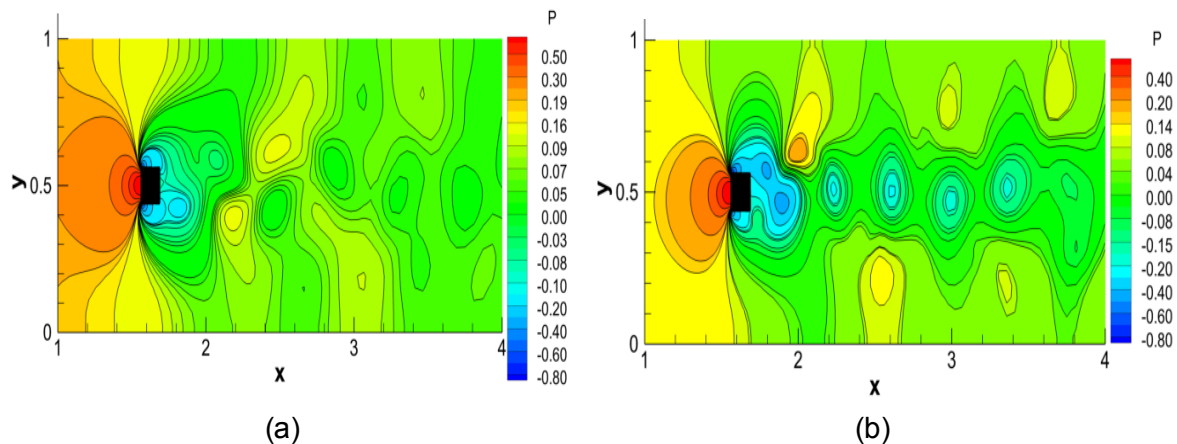


Figure 6.14: Pressure contours for; (a) $Re=65$, and (b) $Re=200$

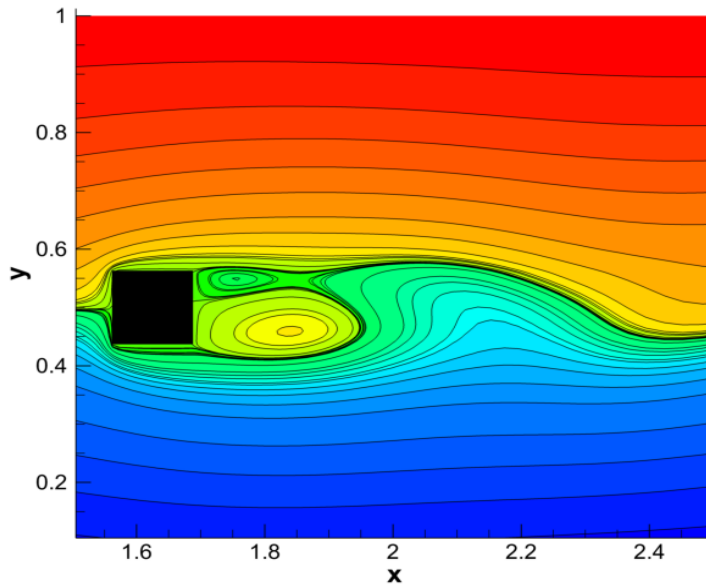


Figure 6.15: Streamlines around square cylinder for $Re=65$

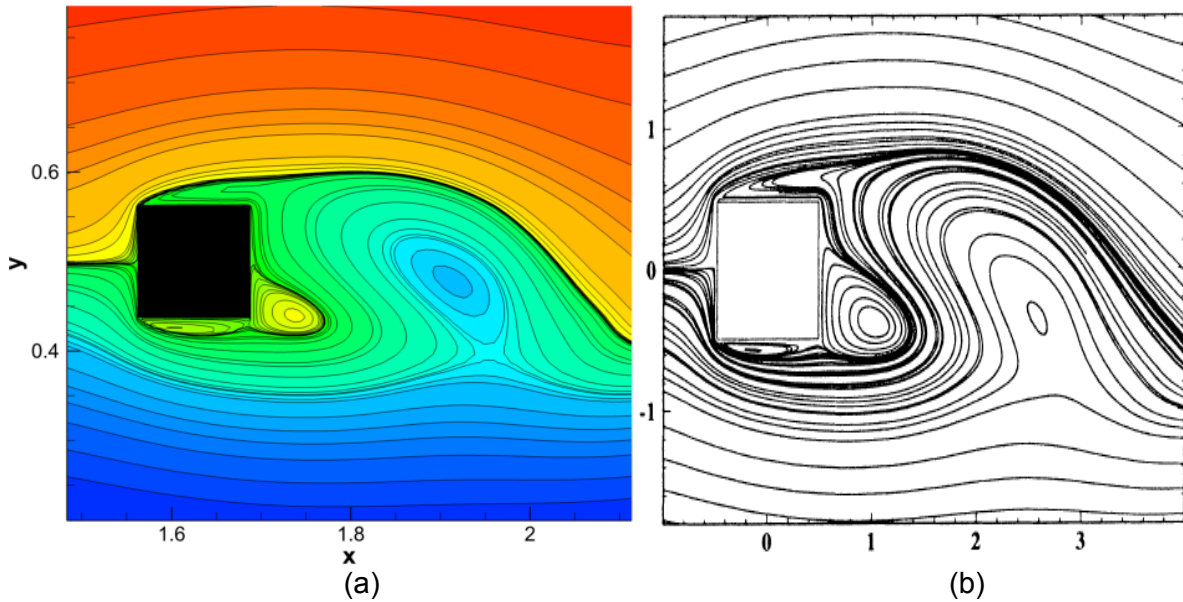


Figure 6.16: Streamlines around square cylinder for $Re=200$ (a) present solution (b)Breuer [19]

From contours of pressure, and velocity as shown in Figure 6.12 till Figure 6.14, it can be seen that contours are no longer symmetric compared to the steady cases. Also a lot of vortices are formed behind the body. Behind the square the flow becomes oscillating as shown in Figure 6.15 and Figure 6.16, which is known as vortex shedding phenomenon. Moreover, it is observed that at $Re = 200$ flow separation occur at the bottom, the top and rear side of

the square while at $Re = 65$ flow separation is at the rear side only. Streamlines for $Re = 200$ in the current study is similar the streamlines in previous work by Breuer [19] as shown in Figure 6.16. Streamlines for other Reynolds number are in the appendix A1.

6.1.3.2.2 Drag and lift coefficient

The time averaged drag and lift coefficient will be computed for unsteady regime $60 < Re \leq 225$ as shown in Figure 6.17. Drag coefficient decrease with Reynolds till it reaches local minimum at $Re=150$, then it starts to increase with Reynolds number. Pressure drag is dominant in unsteady flow regimes. Also drag coefficient follow the same trend of the previous studies in [19, 22]. While the time averaged lift coefficient is zero for different Reynolds number because flow is symmetric around the square.

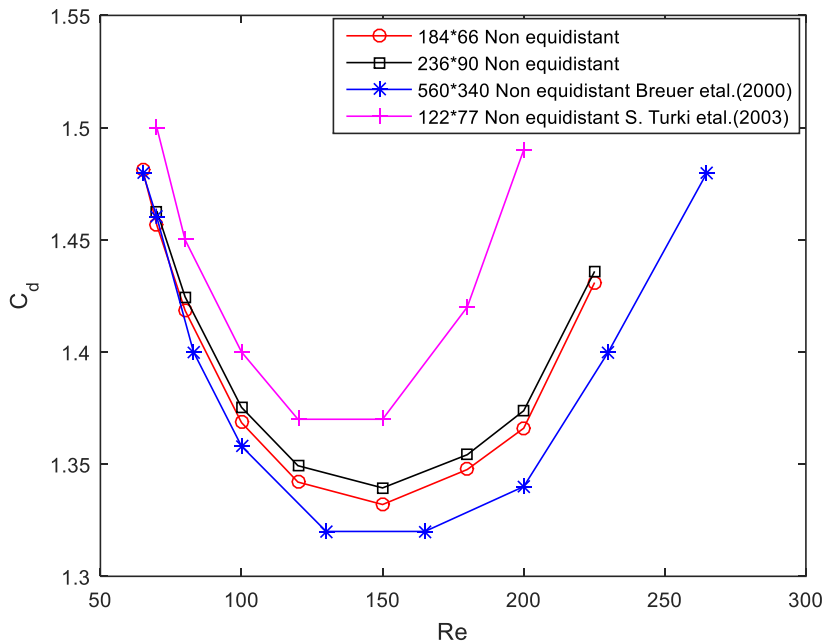


Figure 6.17: Time averaged drag coefficient for different Reynolds number

The variation in the drag and lift coefficient are also calculated as shown in Figure 6.18 and Figure 6.19 respectively. The variation in drag and lift coefficient increase with increasing Reynolds number. The variation of lift coefficient is one order higher than drag coefficient variation. At $Re > 150$ the variation increase at higher rate compared to lower Reynolds number.

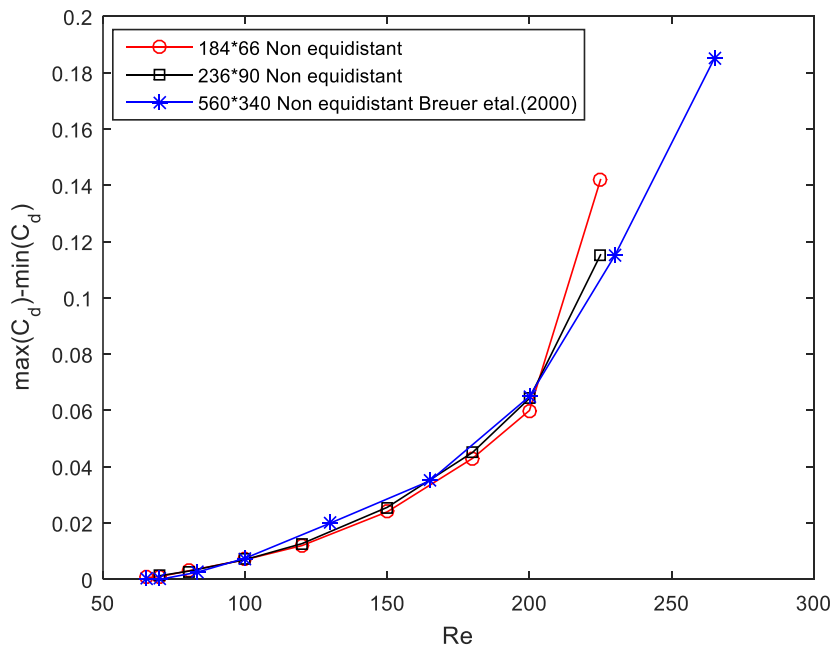


Figure 6.18: Variation of the drag coefficient ($\max(C_d) - \min(C_d)$)

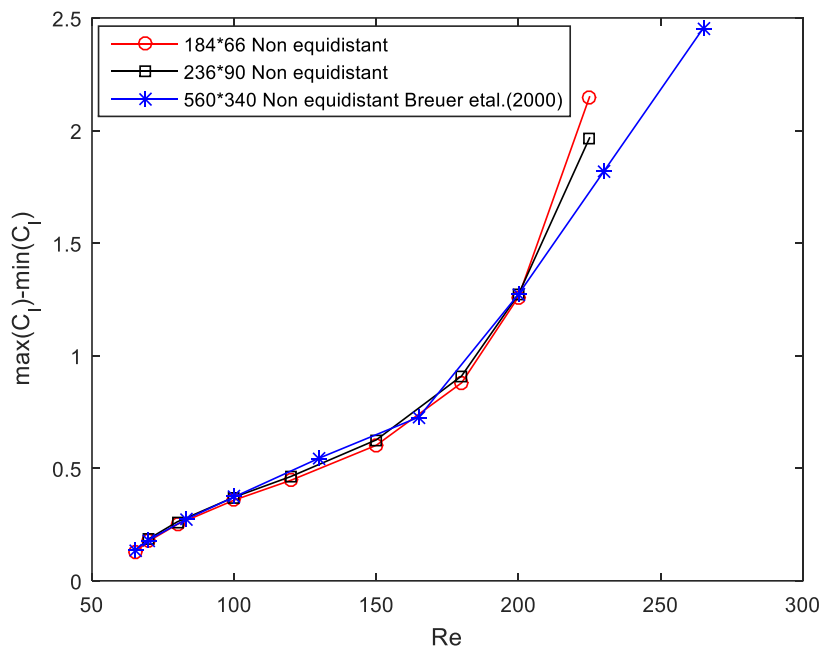


Figure 6.19: Variation of the lift coefficient ($\max(C_l) - \min(C_l)$)

6.1.3.2.3 Strouhal number

Strouhal number is calculated which is used to describe the oscillation of the flow behind square cylinder (vortex shedding phenomenon). As shown in Figure 6.20, Strouhal number increase with increasing Reynolds till it reaches its maximum at $Re = 150$, then it starts to decrease. Current solution follows the same trend of the previous work [19, 22], but at $Re \geq 200$ the deviation between result increase, the reason for this might be using coarser mesh compared to the mesh used in Breuer [19].

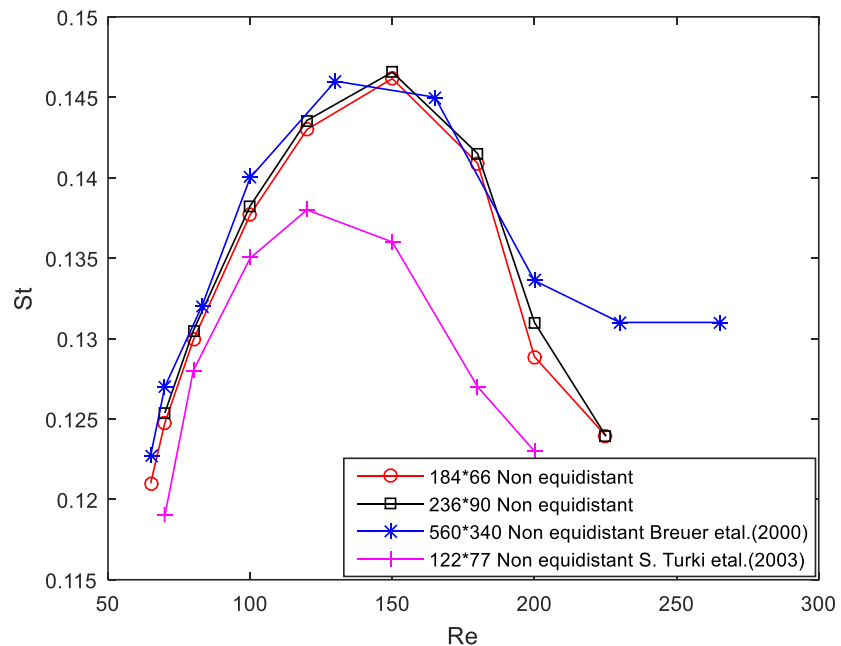


Figure 6.20: Strouhal number for different Reynolds number for unsteady regime

6.2 The effect of blockage ratio on dimensionless force coefficient and heat transfer

In this section the effect of blockage ratio (10% -50% in step of 10%) on dimensionless force coefficient (C_d and C_l) and Nusselt number for constant temperature square cylinder will be investigated. Three different Reynolds number (50,100, and 150) will be used to study the effect of blockage ratio. The flow with Prandtl of 0.7 is used in all the cases.

6.2.1 Computation domain and boundary conditions

The same computational domain and boundary conditions will be used as discussed before in section 6.1.1 and 6.1.2 respectively. Lift coefficient, drag coefficient, Reynolds number and Strouhal number will be calculated based on average velocity u_{av} at the inlet of the channel not based on maximum velocity u_{max} at inlet like in the previous section. Additional boundary conditions for the temperature will be added. Mesh used in this calculations are 288*130,286*110,286*110,288*90,286*80 for blockage ratio from (10-50%). Results for coarser mesh is shown in the Appendix A2.

6.2.1.1 Inlet temperature boundary condition

Dirichlet boundary condition is used for the temperature at the inlet of channel as follows;

$$T = T_\infty \quad (6.18)$$

6.2.1.2 Outlet temperature boundary condition

Zero Neumann boundary condition is applied for the temperature at the outlet of the channel.

$$\frac{dT}{dx} = 0 \quad (6.19)$$

6.2.1.3 Temperature boundary condition for channel walls

Adiabatic boundary condition is used for the channel walls.

$$\frac{dT}{dy} = 0 \quad (6.20)$$

6.2.1.4 Temperature boundary conditions for the square walls

The square walls are maintained at fixed temperature T_w , so Dirichlet boundary condition is applied.

$$T = T_w \quad (6.21)$$

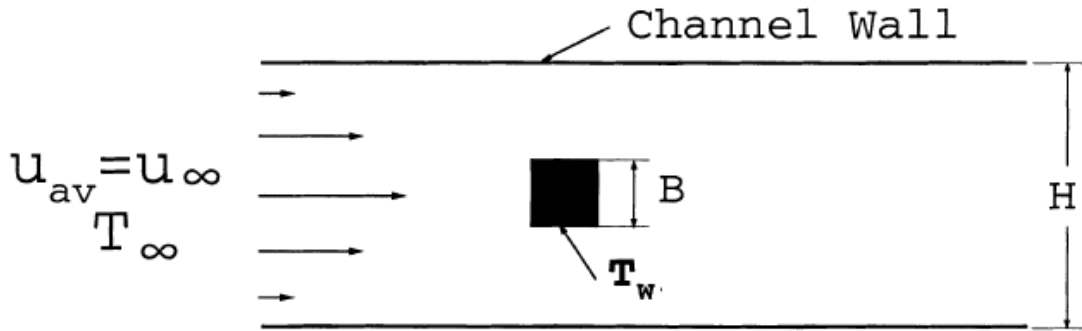


Figure 6.21: Computational domain [23]

6.2.2 Results

6.2.2.1 Flow streamlines and isotherm patterns

6.2.2.1.1 Flow streamlines

Streamlines are plotted for different Reynolds number, and different blockage ratio as shown in Figure 6.22 and Figure 6.23. For $Re = 50$ and blockage ratio of 10% as shown in Figure 6.22(a), it can be seen that unsteady vortex shedding phenomenon appears, but further increasing of the blockage ratio leads to suppression of that phenomenon, flow steadiness and appearance of two vortices as shown in Figure 6.22 (d,g) and Figure 6.23(j,m) for blockage ratio (20-50%). For $Re = 100$ and $Re = 150$, it is observed that flow is unsteady and vortex shedding phenomenon appear for different blockage ratio. Small vortices appear on the channel wall for Reynolds number (100, and 150) for blockage ratio (40% and 50%) as shown in Figure 6.23(n,o) , because at high blockage ratio flow oscillation can easily effect wall boundaries.

6.2.2.1.2 Isotherms patterns

Figure 6.24 and Figure 6.25 shows isotherm pattern for $Re = 150$ for different blockage ratio. At low blockage ratio ($B/H=10\%$), it can be seen that there is single row of temperature contours, but two rows of temperature contours appear at higher blockage ratio ($B/H=20$ and 30%). Further away from the cylinder, the temperature return to the inflow temperature due to flow mixing. At highest blockage ratio ($B/H=40$ and 50%), the temperature contours open and strikes the channel walls.

Chapter 6|Case study: laminar flow around square cylinder

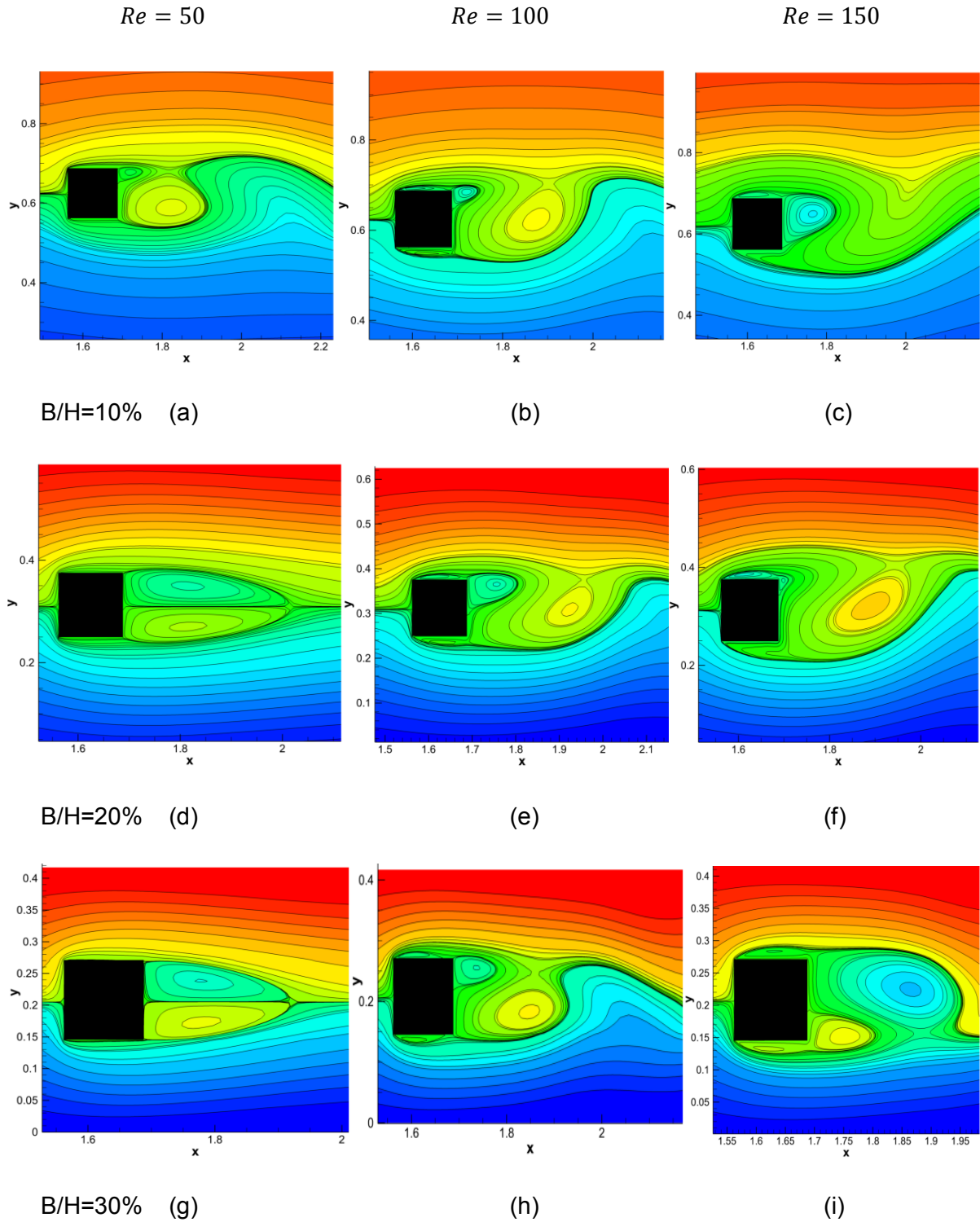


Figure 6.22: Streamlines for blockage ratio (10%-30%) for different Reynolds number (50, 100, and 150)

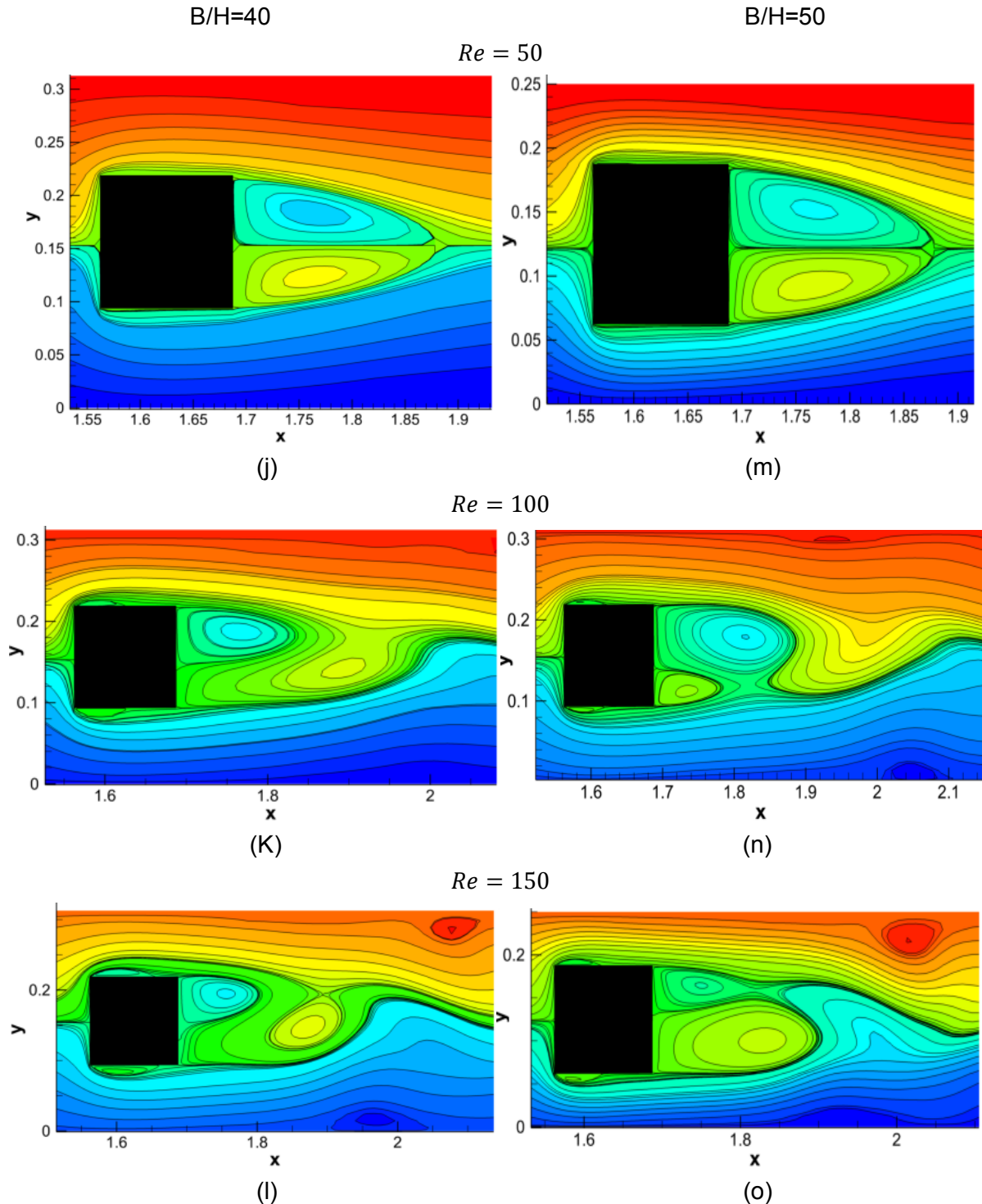


Figure 6.23: Streamlines for blockage ratio (40%, 30%) for different Reynolds number (50, 100, and 150)

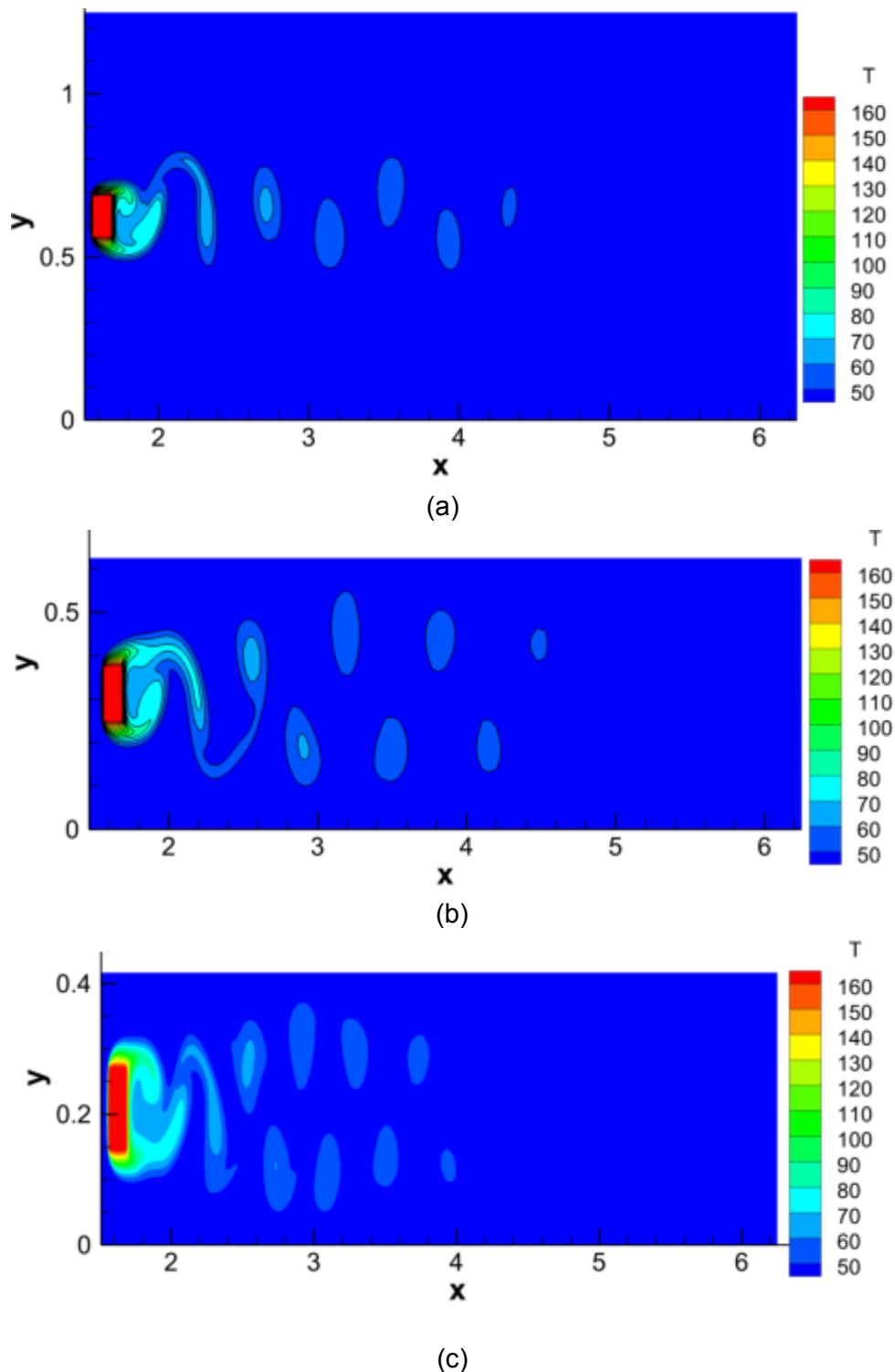


Figure 6.24: Isotherm contours for $Re=150$ for different blockage ratio a) 10% (b) 20% (c) 30%

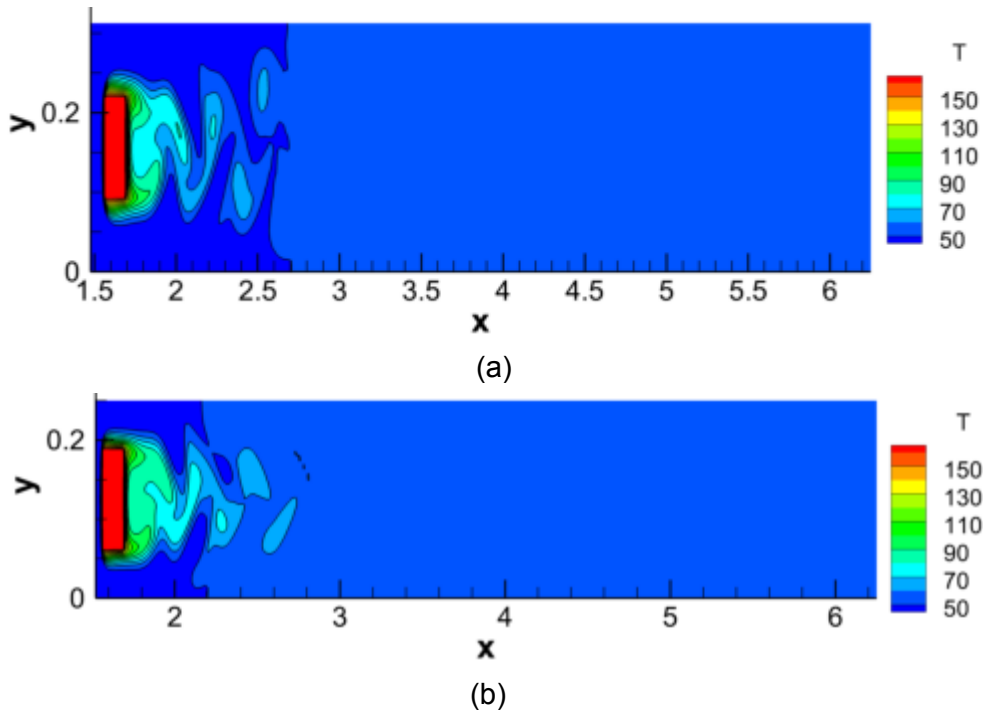


Figure 6.25: Isotherm contours for $Re=150$ for different blockage ratio a) 40% (b) 50%

6.2.2.2 Drag coefficient

In Figure 6.26, drag coefficient or time averaged drag coefficient in case of unsteady flow are plotted for different blockage ratio (10%-50%) for Reynolds number ($Re=50, 100,$ and 150). It can be observed that for the same Reynolds number increasing blockage ratio leads to increasing the Drag coefficient. Also, it can be seen that the drag coefficient decreases with increasing the Reynolds number, however at low blockage ratio (10%, 20%), Drag coefficient at $Re=150$ is higher than Drag coefficient at $Re=100$. Current results are compared to previous work presented by A.Sharma [23]. It can be seen that current solution is quite similar to the previous work and follows the same trend.

6.2.2.3 Strouhal number

Figure 6.27 shows the effect of changing blockage ratio on Strouhal number at different Reynolds number ($Re=50, 100,$ and 150). For $Re=50$, Strouhal number vanishes for blockage ratio $B/H \geq 20\%$, because flow becomes steady. Strouhal number increases with increasing blockage ratio for the same Reynolds number ($Re=100,$ and $Re=150$) especially for blockage ratio greater than 20%. Strouhal number for $Re=150$ is greater than $Re=100$ for blockage ratio 40% and 50%, but for low blockage ratio (10 and 20%), Strouhal number for $Re=100$ is higher.

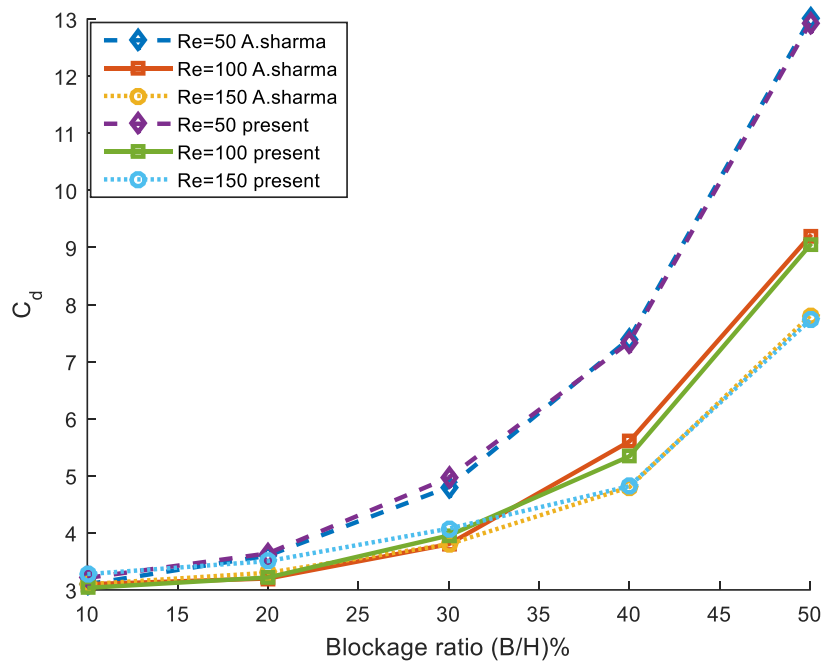


Figure 6.26: Drag coefficient versus blockage ratio at $Re=50, 100, 150$

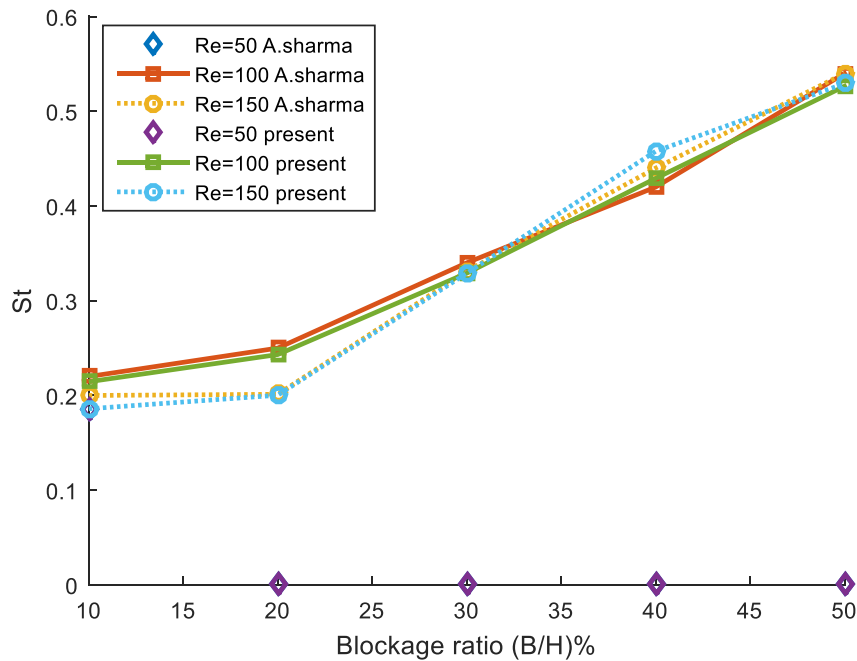


Figure 6.27: Strouhal number versus blockage ratio at $Re=50, 100, 150$

The strouhal number in the current solution is compared to previous work by A.Sharma [23] as shown in Figure 6.27, it can be seen the current solution follow the same trend. There is small difference between the two results because of using coarser mesh compared to mesh used by A.Sharma [23].

6.2.2.4 Average Nusselt number

Average Nusselt number is calculated for front, rear, top and bottom face of the square cylinder for different blockage ratio (10%-50%) at three different Reynolds number ($Re=50,100,$ and 150) as shown in Figure 6.28, Figure 6.29 , and Figure 6.30. The average Nusselt number for the front face is the highest. The top/bottom face are intermediate, followed by the rear face Nusselt number except form blockage ratio (10%, and 20%) at $Re=150$, where the average Nusselt number at the rear face is higher than average Nusselt at Top/bottom face. In Figure 6.28, it can be seen that average Nusselt number for the front face increase with increasing blockage ratio for $Re= 50, 100,$ and 150 . Also at the same blockage ratio increasing Reynolds number leads to increasing the average Nusselt number for the front face, and rear face. From Figure 6.29, for $Re=150,$ and 100 , increasing the blockage ratio causes a decreasing the average Nusselt number for the rear face till it reaches its local minimum at blockage ratio of 40% , then average Nusselt number for rear face starts to increase.

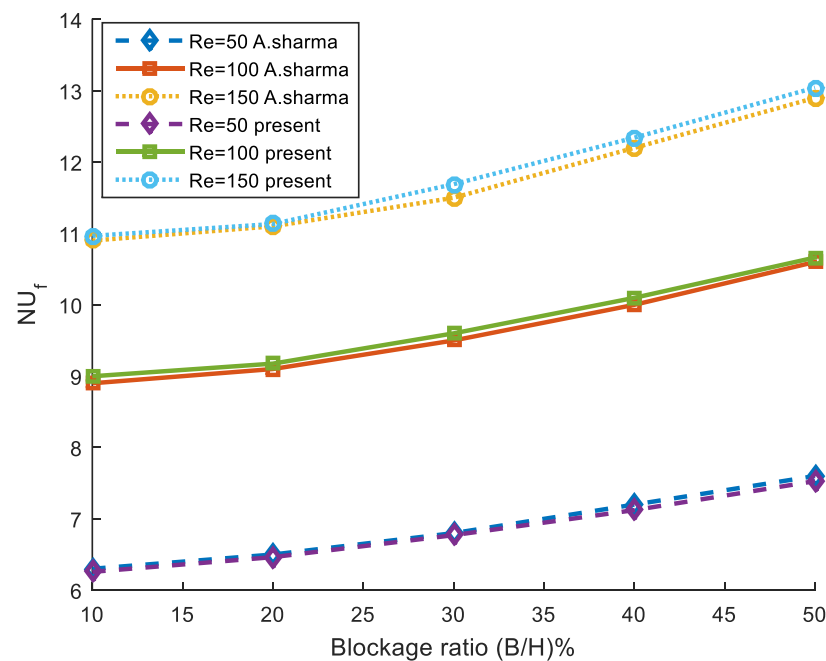


Figure 6.28: Nusselt number for front side of square versus blockage ratio for $Re=50, 100,$ and 150

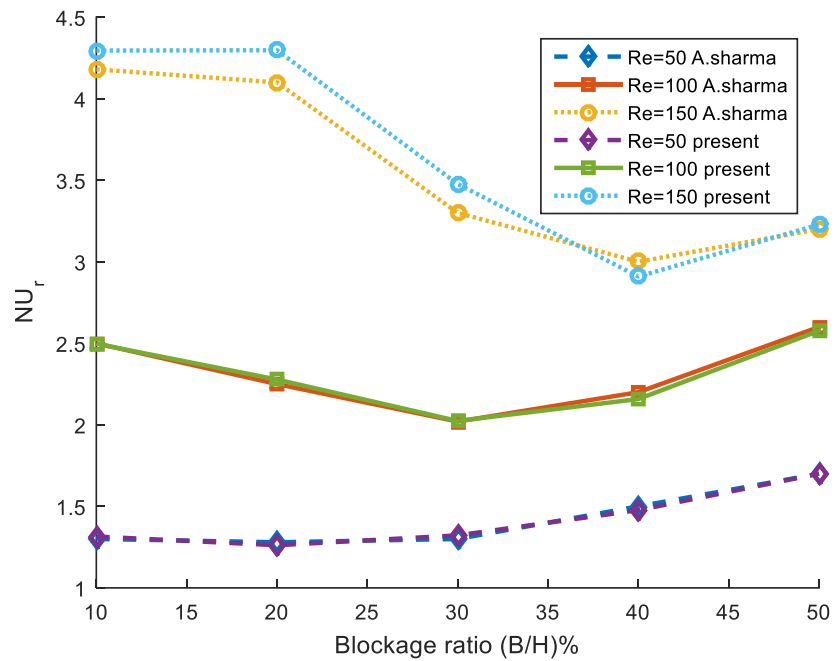


Figure 6.29: Nusselt number for rear side of square versus blockage ratio for $Re=50, 100$, and 150

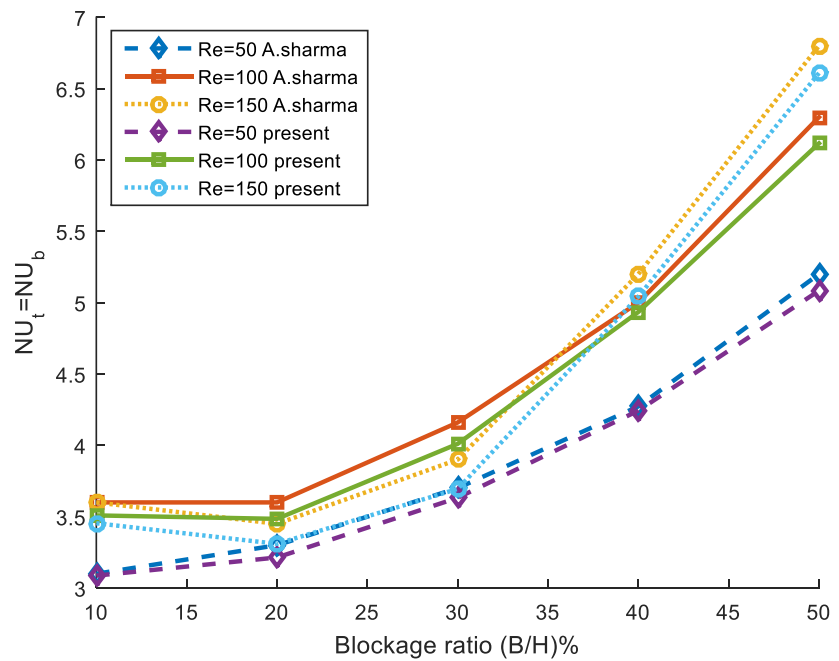


Figure 6.30: Nusselt number for top/bottom side of square versus blockage ratio for $Re=50, 100$, and 150

For $Re=50$ increasing blockage ratio has small effect on average Nusselt number for rear face till blockage ratio of 40% where it starts to increase. For top/bottom average Nusselt number as shown in Figure 6.30, for $Re=150$ increasing blockage ratio causes slight decrease in average Nusselt number for top/bottom face till it reaches its minimum at blockage ratio of 20%, then it increases with increasing the blockage ratio. For $Re=50$, and 100 average Nusselt number for top/bottom face increase with increasing blockage ratio.

From Figure 6.31, it can be concluded that increasing Reynolds number enhances heat transfer and increase average Nusselt number for the square cylinder (NU_c). Also increasing the blockage ratio increase cylinder Nusselt number especially for blockage ratio ≥ 30 .

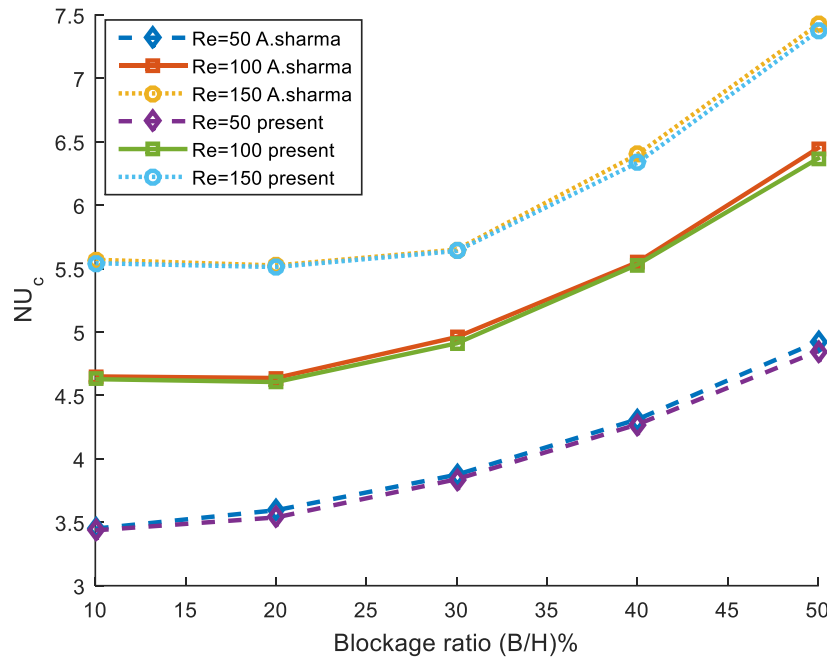


Figure 6.31: Square cylinder average Nusselt number versus blockage ratio for $Re=50$, 100, and 150

6.3 Dimensionless force coefficient and heat transfer for two square cylinder placed in tandem arrangement

After studying the effect of changing Reynolds number and blockage ratio for laminar flow over square cylinder on lift, drag, and heat transfer. In this section, laminar flow over two square cylinder place in tandem arrangement will be analyzed for flow with low Reynolds number $1 \leq Re \leq 30$, and prandtl number $pr = 0.71$.

6.3.1 Computational domain and boundary conditions

Same boundary condition as in the previous section except for the velocity in x-direction for the channel walls as shown in Eq.(6.22). The distance between the inlet and front face of the first cylinder is five Times Square length ($x_u = 5d$) and the distance between the rear face of the second cylinder and the outlet is 15 times of the square length ($x_d = 15d$). Distance separating the two cylinder is five Times Square length($G = 5d$). Blockage ratio of 5% is used ($H = 20d$). Mesh use in this case are 178*152 non uniform mesh and 290*246 non uniform mesh. The later mesh is used in all the presented solution. The computational domain is shown in Figure 6.32

$$\frac{\partial u}{\partial y} = 0 \quad (6.22)$$

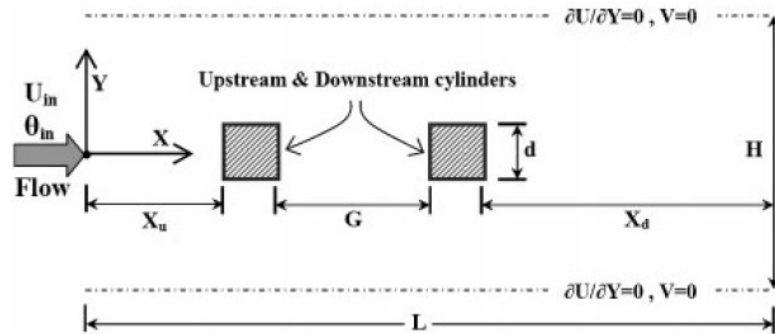


Figure 6.32: Computational domain[24]

6.3.2 Results

6.3.2.1 Streamlines and temperature contours

6.3.2.1.1 Flow streamlines

In Figure 6.33, the streamlines are plotted for different Reynolds number $5 \leq Re \leq 30$. The formation of two symmetrical vortices behind the square cylinders for different Reynolds number can be observed. Also the length of these vortices increase with increasing Reynolds number. The length of vortices behind the upstream cylinder is larger than the vortices length behind the downstream.

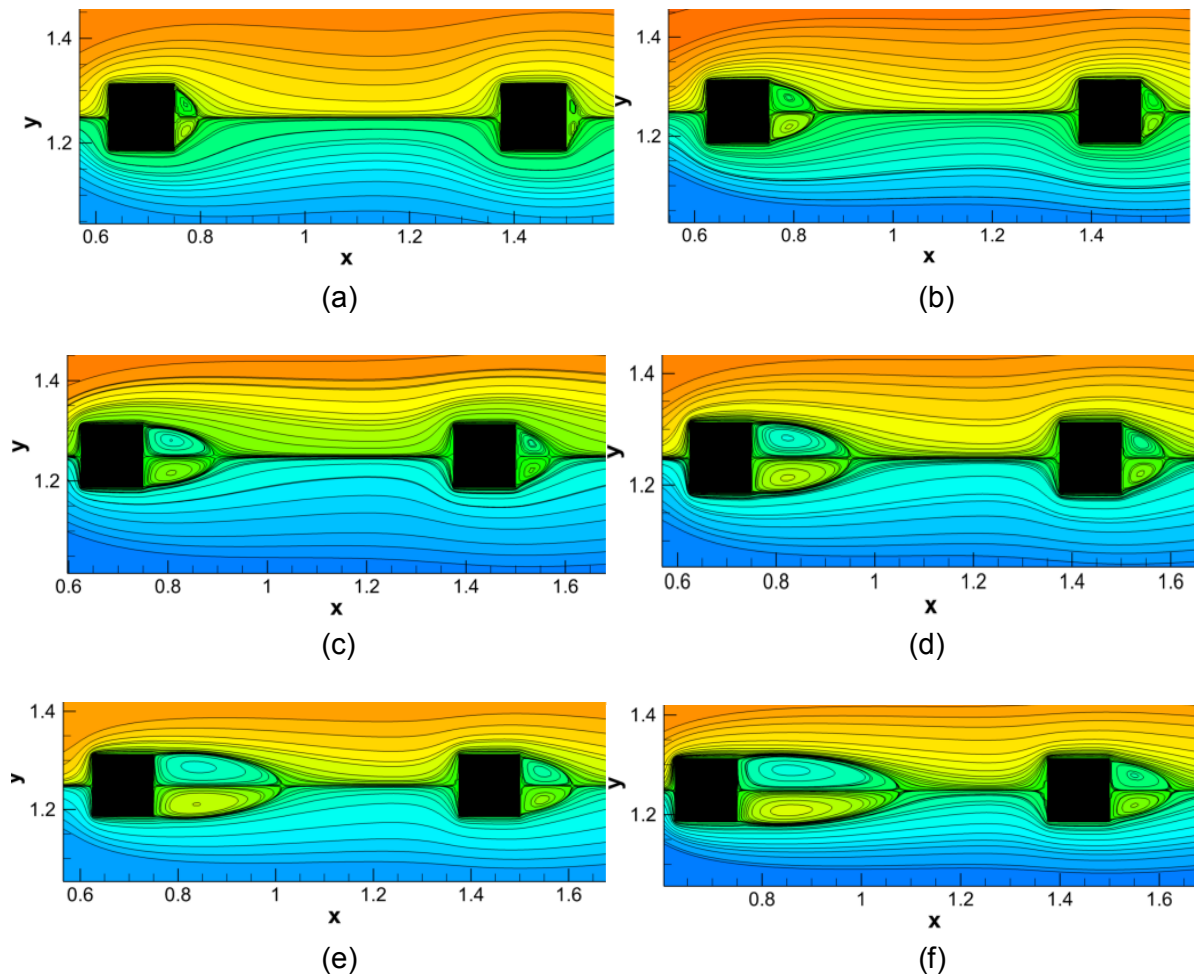


Figure 6.33: Streamlines for two square in tandem arrangement for : (a) $Re=5$, (b) $Re=10$, (c) $Re=15$, (d) $Re=20$, (e) $Re=25$,and (f) $Re=30$

6.3.2.1.2 Temperature contours

Temperature contours are plotted for different Reynolds number $5 \leq Re \leq 30$ as shown in Figure 6.34. It can be seen that contours are more crowded around upstream square cylinder which mean more heat transfer compared to downstream cylinder. Moreover, the thickness of thermal boundary layer decreases with increasing Reynolds number.

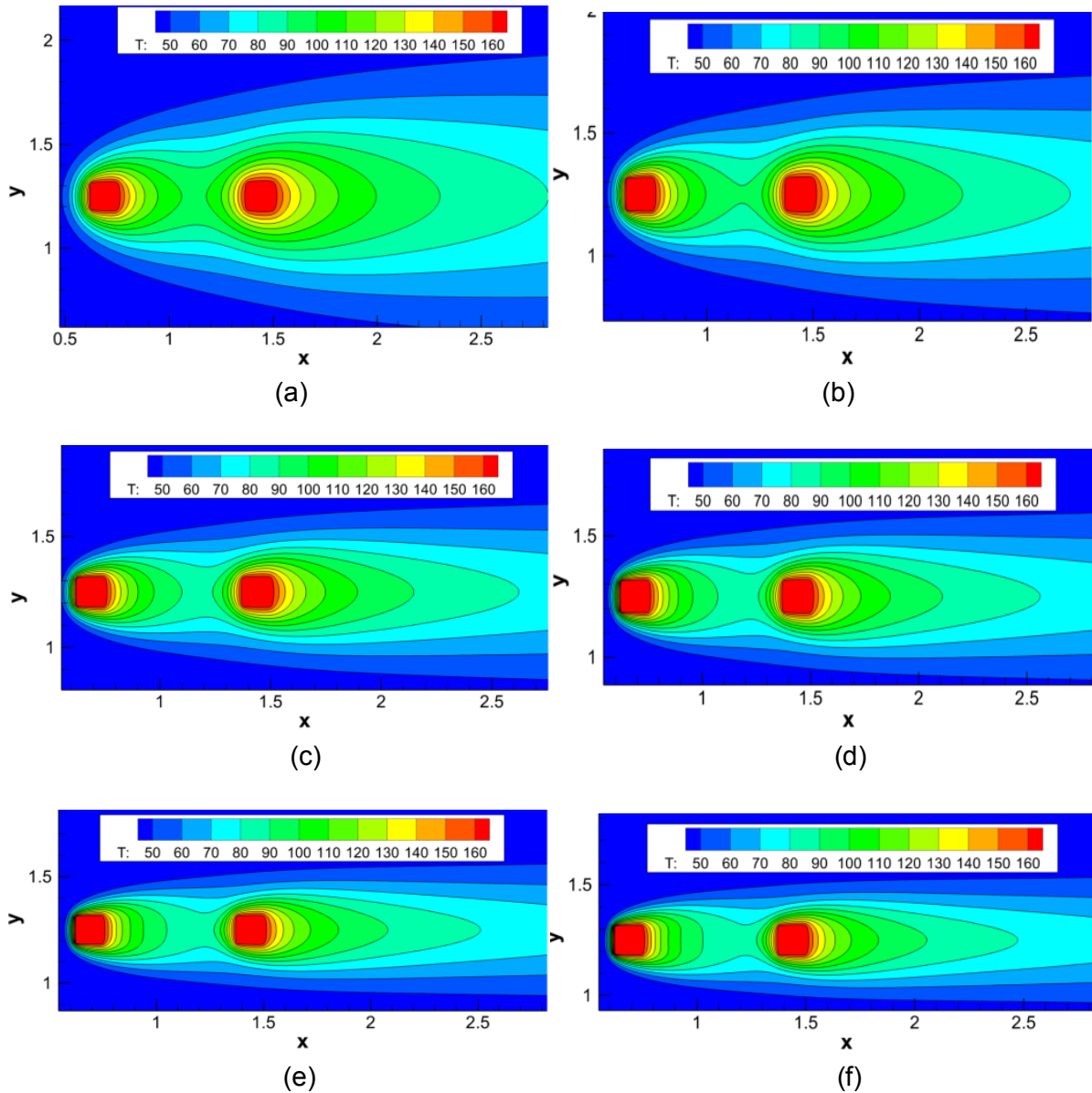


Figure 6.34: Temperature contours for two square in tandem arrangement for: (a) $Re=5$, (b) $Re=10$, (c) $Re=15$, (d) $Re=20$, (e) $Re=25$, and (f) $Re=30$

6.3.2.2 Drag coefficient

Drag coefficient will be calculated and compared to previous work by A. Sohankar [24] as shown in Figure 6.35. It can be observed that the drag coefficient decreases with increasing Reynolds number mainly due to decrease in the pressure drag and friction drag, in which pressure drag contributes more to the drag coefficient compared to friction drag. Also the drag coefficient for the downstream cylinder is lower compared to upstream. The current solution matches previous work by A. Sohankar [24] as shown in Figure 6.35.

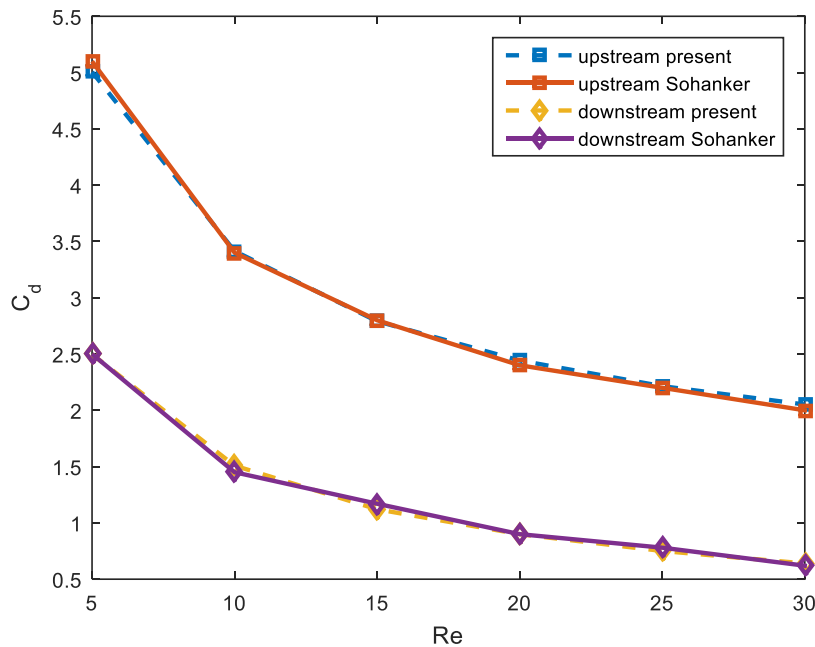


Figure 6.35: Drag coefficient for upstream and downstream square cylinder versus Reynolds number

6.3.2.3 Recirculation length

The recirculation length is calculated as shown in Figure 6.36. It can be seen that recirculation length increases with increasing Reynolds number. Also recirculation length for downstream cylinder is lower compared to downstream cylinder. The current solution is compared to work by A.Sohankar [24] . There is good agreement between the two solutions.

6.3.2.4 Average Nusselt number

Average Nusselt number is calculated for the upstream and downstream square cylinder. Average Nusselt number for the upstream cylinder is higher than the downstream for the same Reynolds number. Nusselt number increase with increasing Reynolds number for both

upstream and downstream square cylinder. Current solution follow the same trend of the previous work by A.Sohanker, however there is difference between the two solutions. Two

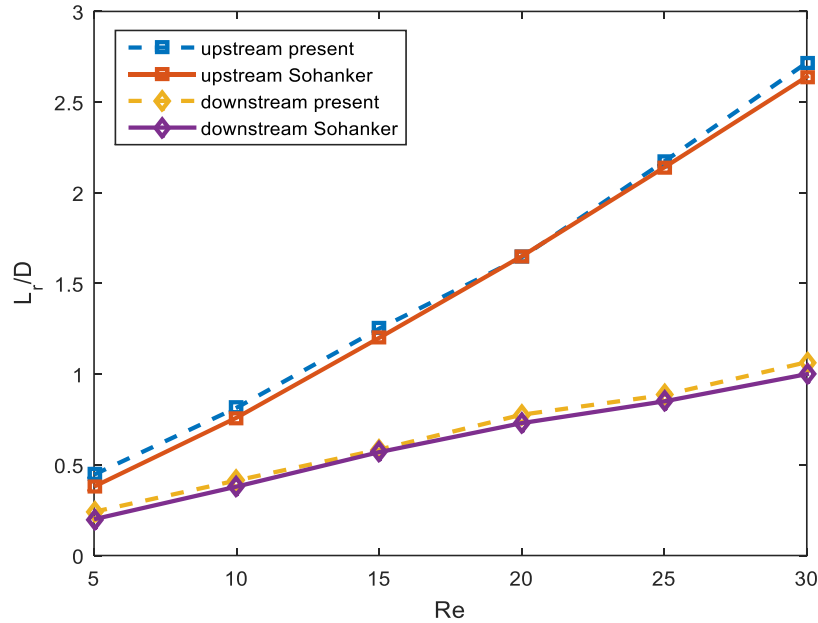


Figure 6.36: Recirculation length for upstream and downstream square cylinder versus Reynolds number

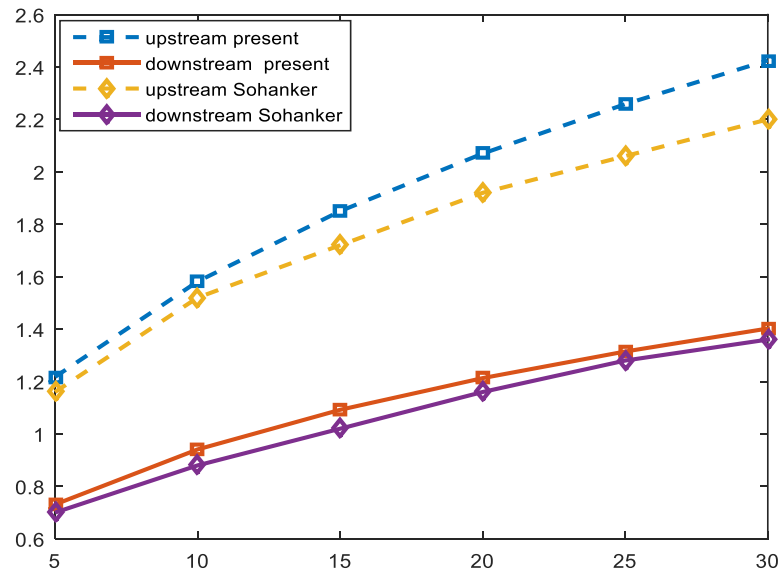


Figure 6.37: Average Nusselt for upstream and downstream square cylinder versus Reynolds number

mesh are used in the current work 178*152 and 290*246 nonuniform meshes and difference between results obtained from two meshes is less than 1%, which mean that current results are mesh independent.

6.4 Comparison between the effects of mixed convection compared to forced convection on heat transfer and dimensionless force coefficient for two square cylinder in tandem arrangement.

In this section the effect of mixed convection for two square cylinders placed in tandem arrangement on dimensionless force coefficient and heat transfer will be investigated and compared to forced convection case. Flow is with Reynolds number $1 \leq Re \leq 30$, Richardson number $Ri = 1$ for mixed convection and prandtl number $\text{Pr} = 0.7$. Fixed blockage ratio of 10% will be used. The spacing between the cylinders is fixed with four times of the cylinder width. The streamlines and temperature contours are presented and discussed. In addition, the overall drag and lift coefficients, and average Nusselt numbers are determined to demonstrate the role of Reynolds, and Richardson numbers on flow patterns and heat transfer.

6.4.1 Computational domain and boundary conditions

The computational domain used is similar to one used as in the previous section. Only the distance between two cylinders is changed to be 4 times the width of the square ($s = 4d$) , and no slip boundary conditions is used for channel walls. Same distance between the inlet (AD) and upstream square front face ($L_u = 5d$), and distance between exit (BC) and downstream cylinder rear face ($L_d = 15d$).The computational domain is shown in Figure 6.38. Non-uniform mesh of $178*70$ is used in all the computations.

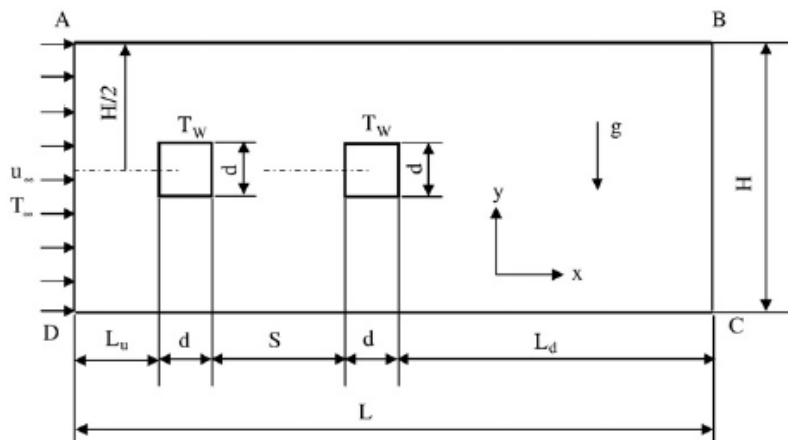


Figure 6.38: Computational domain[25]

6.4.2 Results

6.4.2.1 Streamlines

Streamlines are plotted as shown in Figure 6.39 for different Reynolds number ($Re=1, 10, 20$, and 30) for forced convection ($Ri=0$) and mixed convection ($Ri=1$). It can be seen that

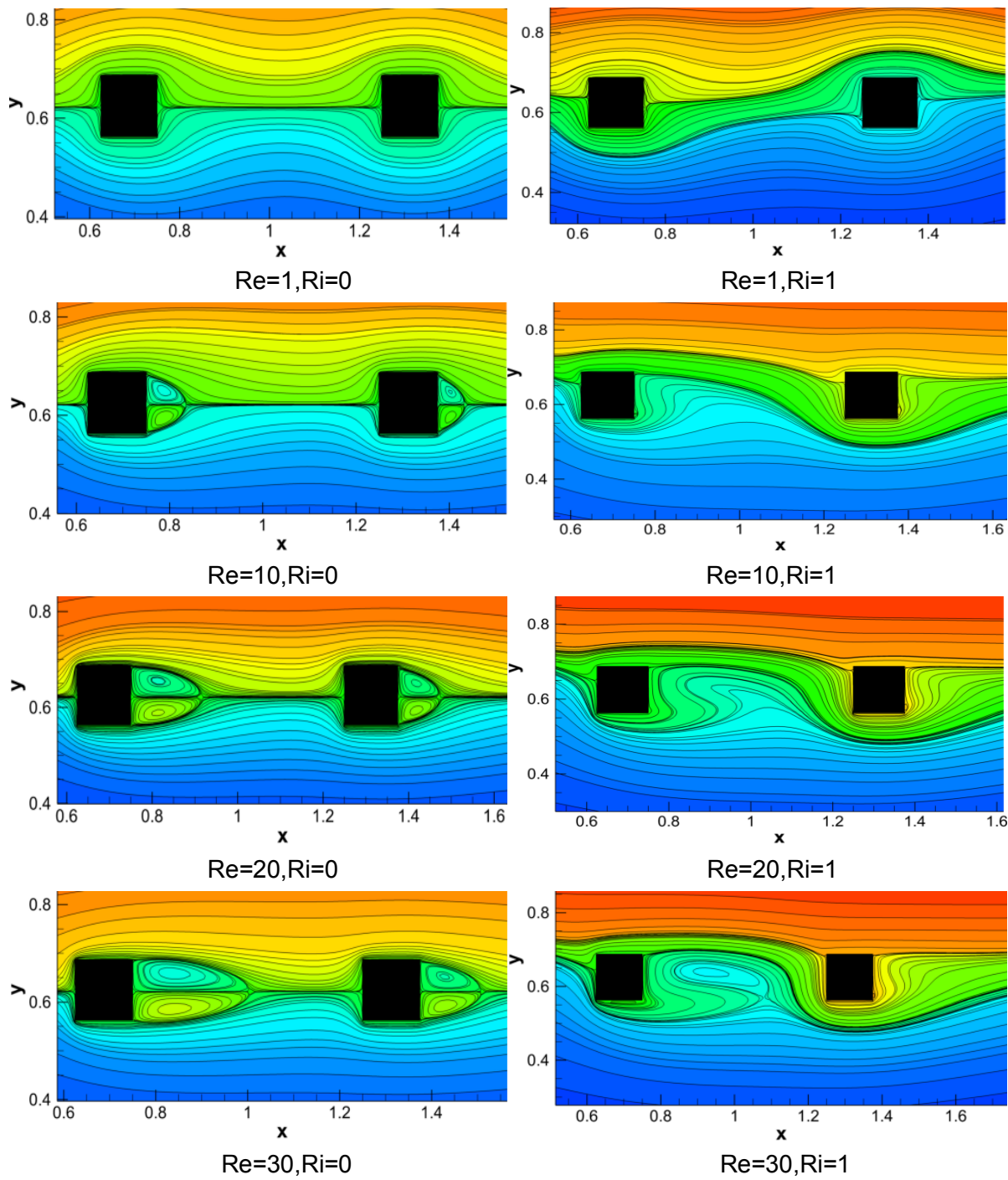


Figure 6.39: Streamlines for Reynolds number $Re= 1, 10, 20$, and 30 for forced convection ($Ri=0$) and mixed convection ($Ri=1$)

The flow is fully attached to square cylinders in low Reynolds number ($Re=1$). Increasing Reynolds number ($Re=10, 20$, and 30) lead to flow separation and formation of vortices behind the square cylinders. In forced convection cases ($Ri=0$), the flow is perfectly symmetric, but for mixed convection cases ($Ri=1$), the flow is no longer symmetric because of thermal buoyancy effect.

6.4.2.2 Temperature contours

Figure 6.41 shows the temperature contours for flow around two squares in tandem arrangement for Reynolds number ($Re=1, 10, 20$, and 30) for forced convection ($Ri=0$) and mixed convection ($Ri=1$). Like streamlines, for forced convection cases the temperature contours are symmetric, while in mixed convection cases the temperature contours are no longer symmetric, due to the effect of thermal buoyancy. Moreover, the temperature contours are more crowded around the upstream cylinder, which indicates higher heat transfer and consequently higher Nusselt number compared to the downstream cylinder.

6.4.2.3 Drag coefficient

The drag coefficient is plotted for forced convection ($Ri=0$) and mixed convection ($Ri=1$) for different Reynolds number ($Re=1, 10, 20$, and 30). Mixed convection cases are compared to

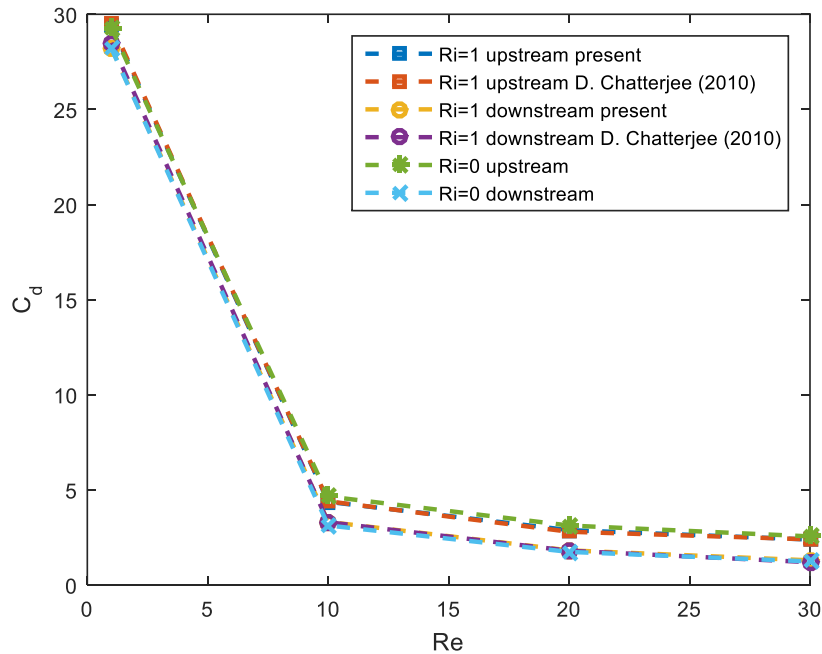


Figure 6.40: Drag coefficient for upstream and downstream cylinder versus Reynolds number for forced convection ($Ri=0$) and mixed convection ($Ri=1$)

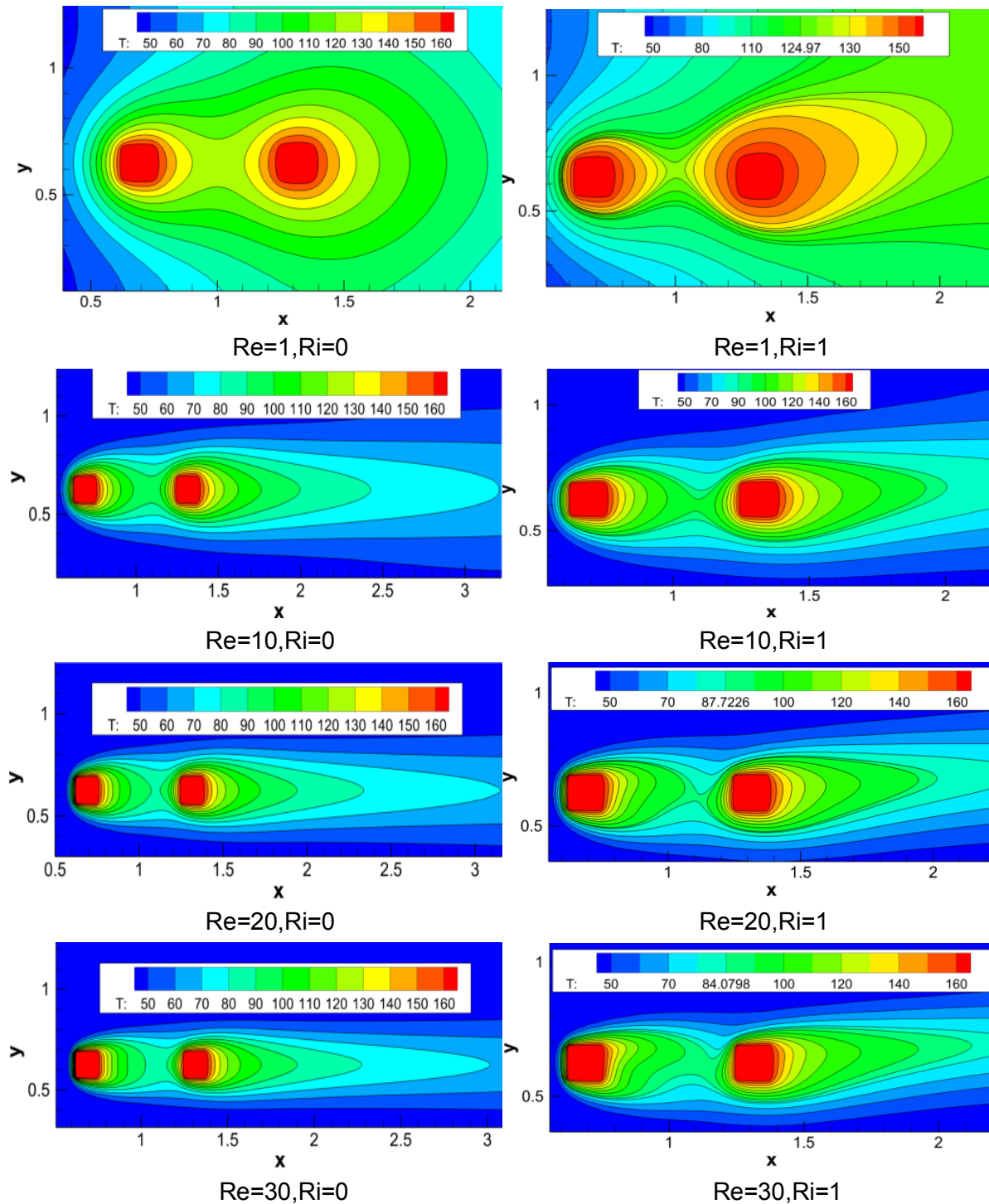


Figure 6.41: Temperature contours for Reynolds number $Re = 1, 10, 20$, and 30 for forced convection ($Ri=0$) and mixed convection ($Ri=1$)

Previous work by D.Chatterjee [25] as shown in Figure 6.40. it can be seen the drag coefficient is high at low Reynolds number for both mixed and forced convection cases ,then it starts to decrease due to decrease in pressure and friction drag because of flow separation. The drag coefficient for upstream cylinder is slightly higher than downstream cylinder. Also the drag coefficient is not highly affected by changing of Richardson number from ($Ri=0$) to ($Ri=1$). Moreover , the current results for Mixed convection ($Ri=1$) follow the same trend of previous work by D.Chatterjee[25] , but small difference appear because of coarse mesh used in current solution($178*70$) compared to ($300*140$) used in the previous work.

6.4.2.4 Lift coefficient

From Figure 6.42, for mixed convection cases ($Ri=1$), lift coefficient for the upstream cylinder decrease with increasing Reynolds number, while it increases with increasing Reynolds number for downstream cylinder. Also in mixed convection cases the lift force is generated because the flow is asymmetric, but in forced convection cases the flow is symmetric, so the lift force vanishes. Current solution follows the same trend of the previous work[25].

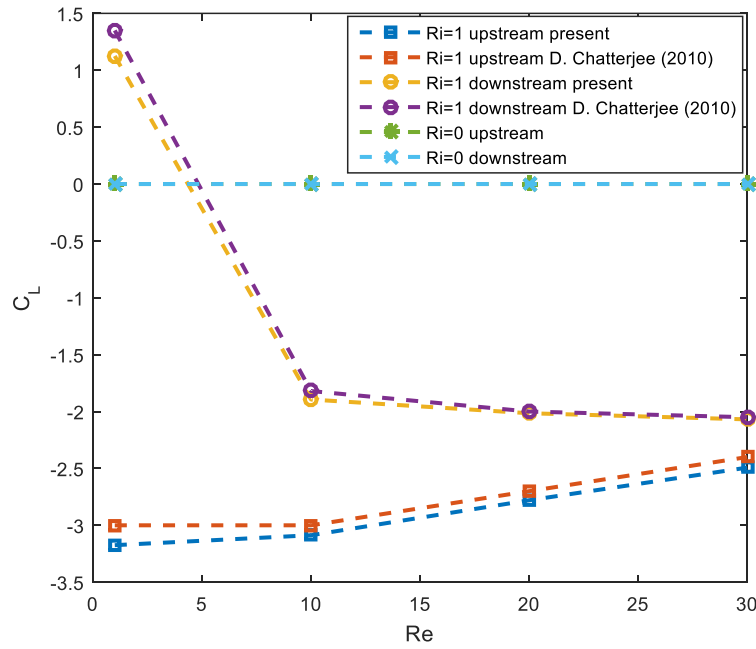


Figure 6.42: lift coefficient for upstream and downstream cylinder versus Reynolds number for forced convection ($Ri=0$) and mixed convection ($Ri=1$)

6.4.2.5 Average Nusselt number

The variation of average Nusselt number for the upstream and downstream cylinder is plotted for different Reynolds number ($Re=1, 10, 20$, and 30) for forced and mixed convection as shown in Figure 6.43. It can be seen, that average Nusselt number increases with increasing Reynolds number for both upstream and downstream cylinders in forced and mixed convection cases. Moreover, average Nusselt number for mixed convection cases is higher than forced convection cases especially for downstream cylinder, while in upstream cylinder the increase is not significant.

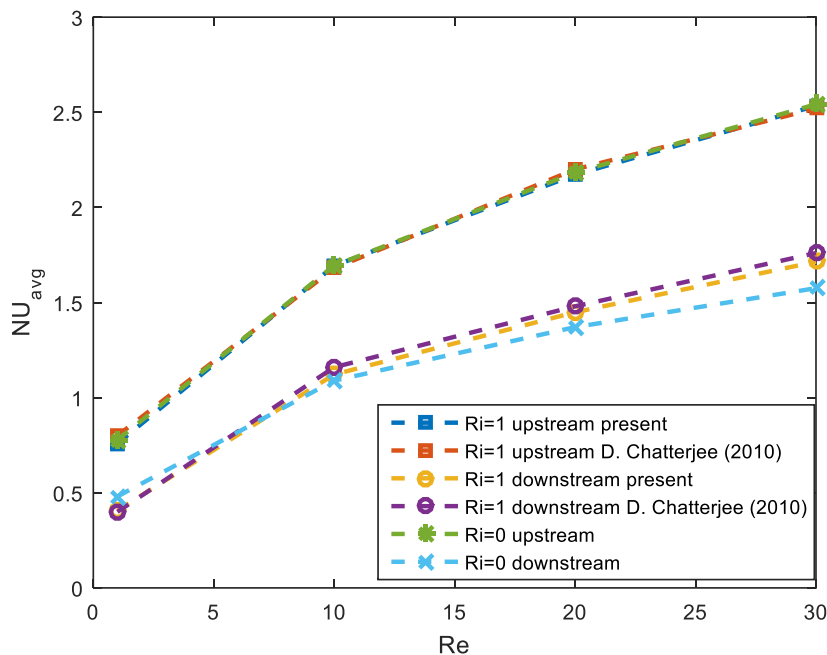


Figure 6.43: Average Nusselt number for upstream and downstream cylinder versus Reynolds number for forced convection ($Ri=0$) and mixed convection ($Ri=1$)

From Figure 6.44, it can be seen that Nusselt number for the front face of the upstream cylinder is unaffected by increasing Richardson number, while the front face for the downstream cylinder increases with increasing Richardson number especially for $Re \geq 10$. For the Nusselt number for the rear face as shown in Figure 6.45, the upstream rear face Nusselt number is unaffected by increasing Ri for $Re \geq 10$. In Nusselt number is higher for ($Ri=1$), and ($Re>10$), but for the downstream cylinder rear face Figure 6.46, the top face Nusselt number decrease for upstream and downstream cylinders by increasing Ri because the velocity on the top faces of the cylinders decrease due thermal buoyancy effect, which leads to decrease in heat transfer. On the contrary, the bottom face Nusselt number for

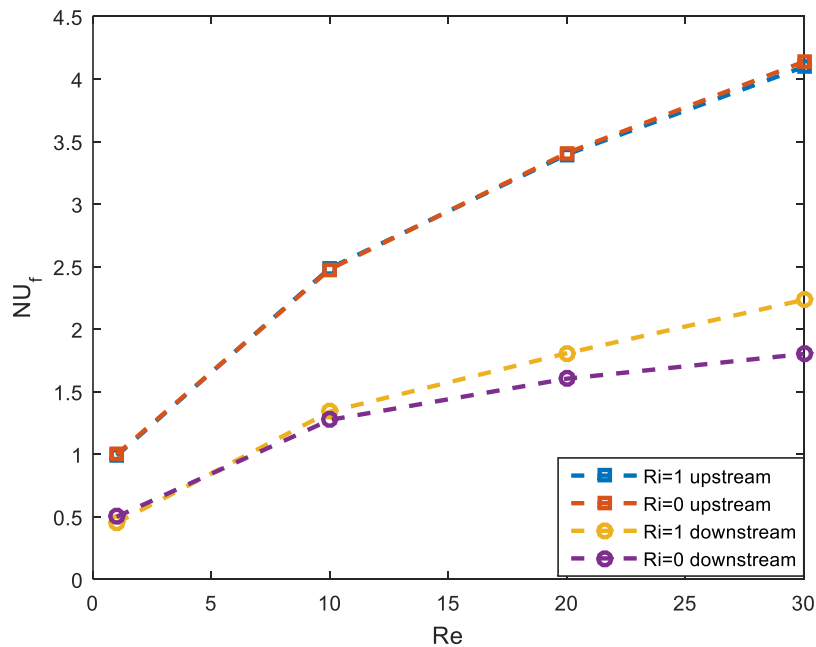


Figure 6.44: Front face Nusselt number for upstream and downstream cylinder versus Reynolds number for forced convection ($Ri=0$) and mixed convection ($Ri=1$)

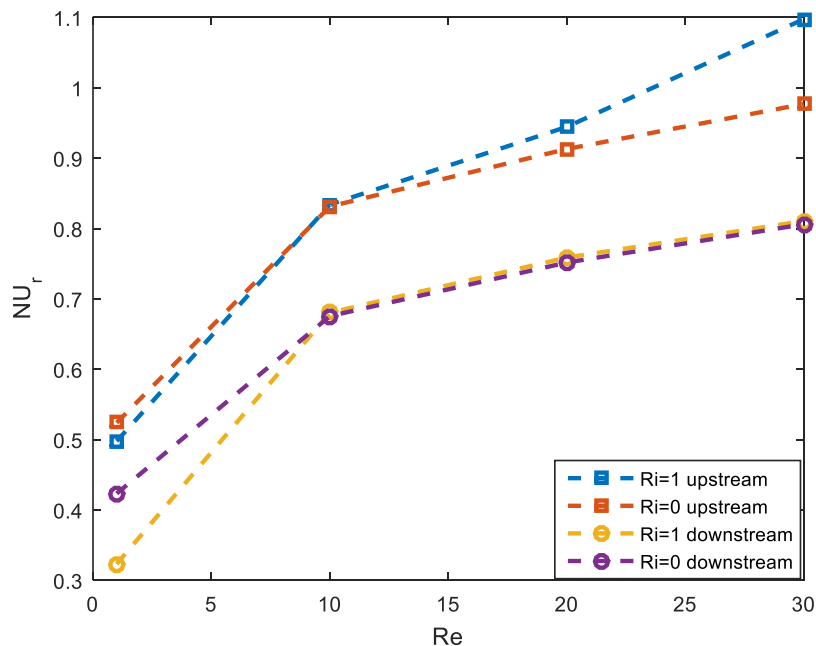


Figure 6.45: Rear face Nusselt number for upstream and downstream cylinder versus Reynolds number for forced convection ($Ri=0$) and mixed convection ($Ri=1$)

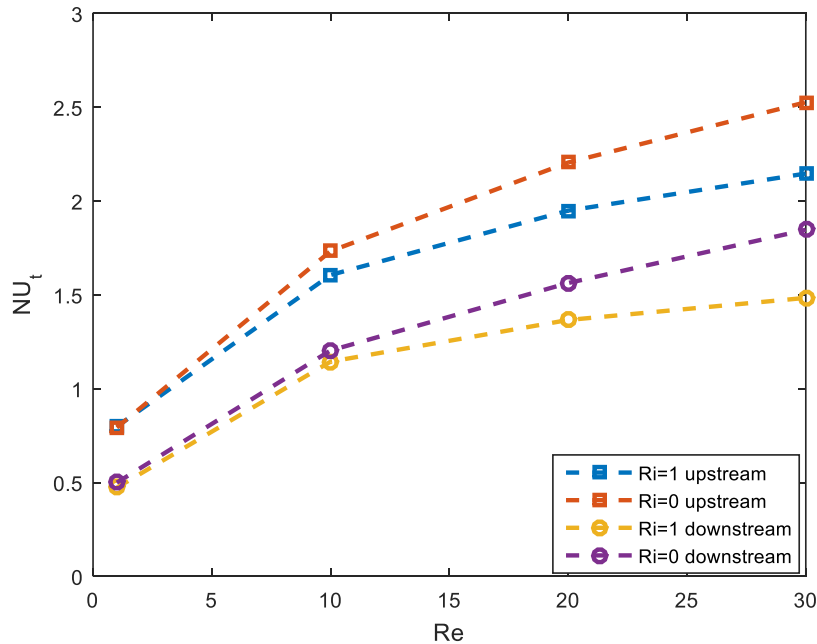


Figure 6.46: Top face Nusselt number for upstream and downstream cylinder versus Reynolds number for forced convection ($Ri=0$) and mixed convection ($Ri=1$)

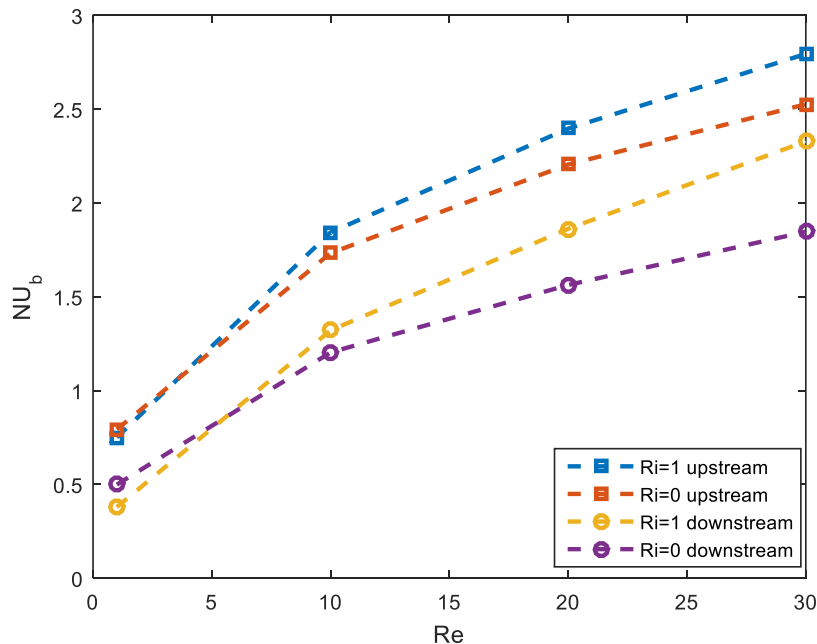


Figure 6.47: Bottom face Nusselt number for upstream and downstream cylinder versus Reynolds number for forced convection ($Ri=0$) and mixed convection ($Ri=1$)

upstream and downstream cylinder increase with increasing R_i , because velocity near the bottom face of the cylinders increase which causes an increase in the heat transfer as shown in . Also Nusselt number for the top and bottom face are equal on forced convection case ($R_i=0$) because flow is symmetric, while in mixed convection cases Nusselt number for the bottom face is higher than the top face Nusselt number.

7 Conclusion

The aim of our work is to develop numerical code using C++ language to simulate two dimensional incompressible laminar flow over square cylinder. Some hypothesis is used to simplify the case like; incompressible flow, Newtonian fluid, constant physical properties, and radiation is neglected. Calculated parameters from this program are streamlines, temperature contours, velocity profile, pressure profile, drag coefficient, lift coefficient, and Strouhal number.

From software verification chapter it can be concluded that the developed code is reliable and works properly. It was further developed to model the case study in chapter five. The main finding from the case study are; for specific blockage ratio, in the steady cases, increasing Reynolds number lead to an increase in the recirculation length of the vortices behind the square and decrease in the drag coefficient due to decrease in pressure and viscous drag. For unsteady cases, drag coefficient decrease with increasing Reynolds number till it reaches local minimum than it starts to increase. Pressure drag is dominant in unsteady cases. Strouhal number increase with increasing Reynolds number till it reaches maximum value, then it starts to decrease. Also the variation in lift and drag coefficient increase with increasing Reynolds number. Increasing blockage ratio for specific Reynolds number, lead to increase in the drag coefficient, Strouhal number and enhancing heat transfer. For two square cylinder in tandem arrangement, the drag coefficient decreases with increasing Reynolds number for both cylinder. Moreover, Drag coefficient for upstream cylinder is higher compared to the downstream cylinder. Also recirculation length for both cylinder increase with increasing Reynolds number and recirculation length for upstream is higher than downstream cylinder. The heat transfer increase with increasing Reynolds number and heat transfer for the upstream cylinder is higher. Increasing Richardson number has slight effect on drag coefficient, but changes the lift coefficient from null in forced convection to value in case of mixed convection because the flow is no longer symmetric. Also heat transfer for upstream cylinder is not affect by increasing Richardson number, but for the downstream cylinder heat transfer increases slightly.

Future work

Future work can be developing the code to model 2D turbulent flows using LES model or $k - \varepsilon$ model. Also further step is modifying and upgrading the code to model 3D problem, so flow around short square cylinder can be modeled. Moreover another development can be using of unstructured mesh that will enable simulation of the flow around complex geometries.

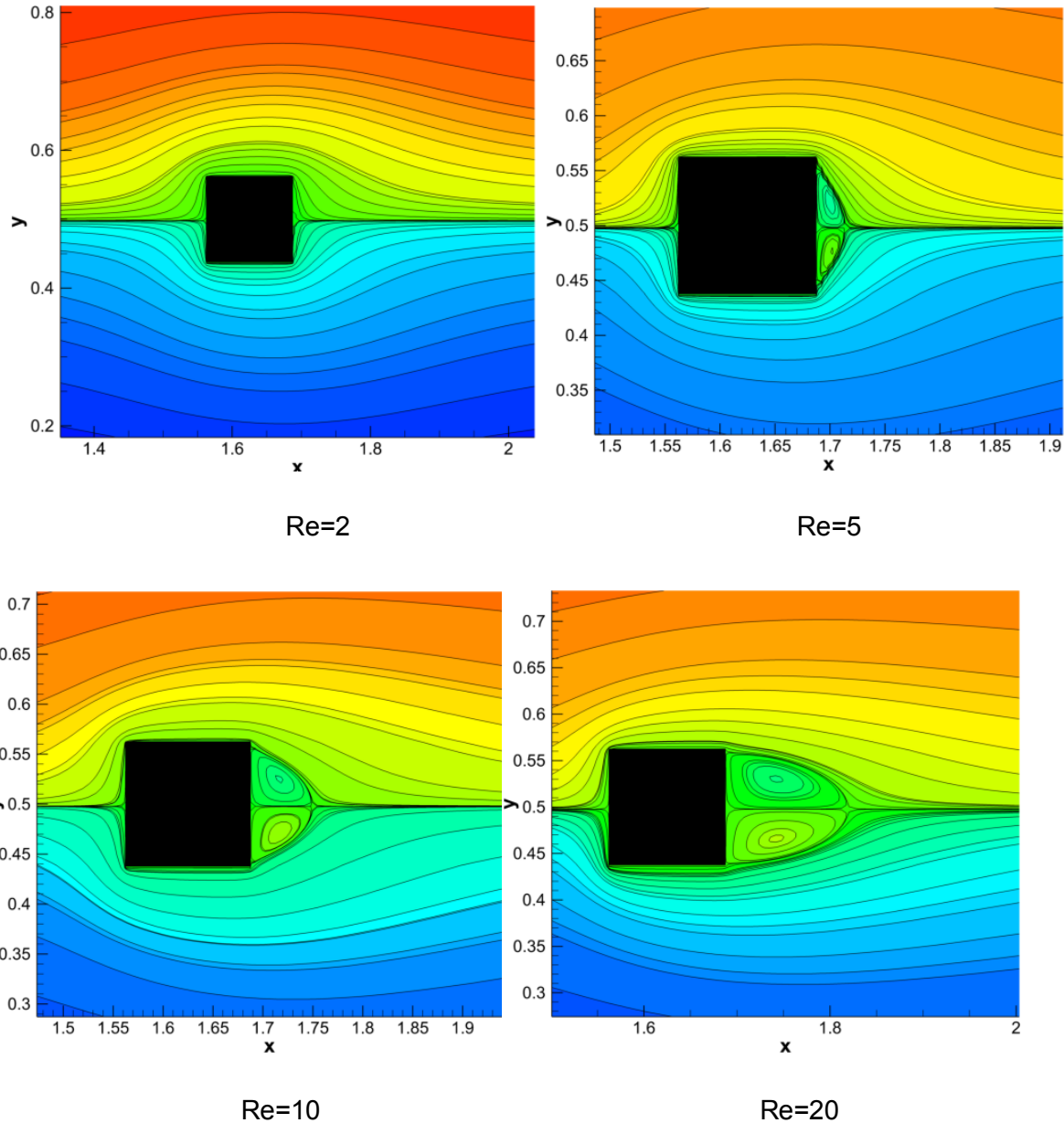
Reference

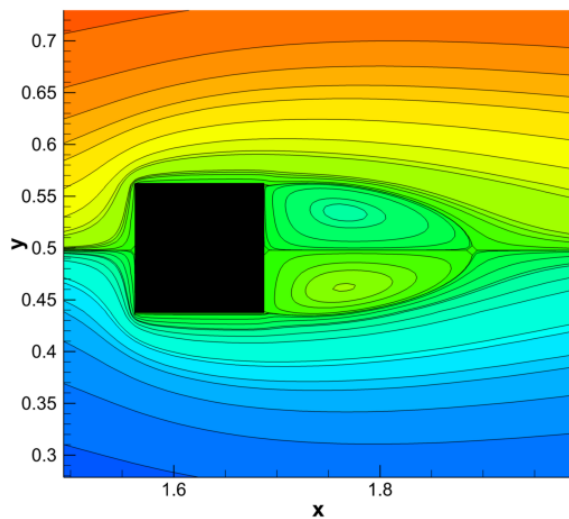
1. Whitaker, S., *Fundamental principles of heat transfer*. 2013: Elsevier.
2. CTTC, *Numerical solution of convection*. Heat and Mass Transfer Technological Center - POLYTECHNIC UNIVERSITY OF CATALONIA
3. Pepper, D.W., *The intermediate finite element method: Fluid flow and heat transfer applications*. 1999: CRC Press.
4. Perić, M., R. Kessler, and G. Scheuerer, *Comparison of finite-volume numerical methods with staggered and colocated grids*. Computers & Fluids, 1988. **16**(4): p. 389-403.
5. MIT, *Numerical Fluid Mechanics .Fall 2011 – Lecture 24*. MIT.
6. Oriol, *Fractional step Method, part1:Staggered Meshes*.
7. Darwish, M., *A new high-resolution scheme based on the normalized variable formulation*. Numerical Heat Transfer, Part B Fundamentals, 1993. **24**(3): p. 353-371.
8. Versteeg, H.K. and W. Malalasekera, *An introduction to computational fluid dynamics: the finite volume method*. 2007: Pearson Education.
9. Alves, M., P. Oliveira, and F. Pinho, *A convergent and universally bounded interpolation scheme for the treatment of advection*. International journal for numerical methods in fluids, 2003. **41**(1): p. 47-75.
10. CTTC, *Introduction to Fractional Step Method*. UNIVERSITAT POLITECNICA DE CATALUNYA.
11. MIT, *2.29 Numerical Fluid Mechanics – Lecture 10*. 2011.
12. Sohankar, A., C. Norberg, and L. Davidson, *Low-Reynolds-number flow around a square cylinder at incidence: study of blockage, onset of vortex shedding and outlet boundary condition*. International journal for numerical methods in fluids, 1998. **26**(1): p. 39-56.
13. Yoshida, T., I. Nakamura, and T. Watanabe. *Numerical analysis of open boundary conditions for an incompressible viscous flow past a square cylinder*. in *6th National Symposium on Computational Fluid Dynamics*. 1993.
14. Courant, R., K. Friedrichs, and H. Lewy, *Über die partiellen Differenzengleichungen der mathematischen Physik*. Mathematische Annalen, 1928. **100**(1): p. 32-74.
15. Simons, E., *An efficient multi-domain approach to large-eddy simulation of incompressible turbulent flows in complex geometries*. 2000.

-
16. Oberkampf, W.L. and T.G. Trucano, *Verification and validation in computational fluid dynamics*. Progress in Aerospace Sciences, 2002. **38**(3): p. 209-272.
 17. Ghia, U., K.N. Ghia, and C. Shin, *High-Re solutions for incompressible flow using the Navier-Stokes equations and a multigrid method*. Journal of computational physics, 1982. **48**(3): p. 387-411.
 18. de Vahl Davis, G. and I. Jones, *Natural convection in a square cavity: a comparison exercise*. International Journal for numerical methods in fluids, 1983. **3**(3): p. 227-248.
 19. Breuer, M., et al., *Accurate computations of the laminar flow past a square cylinder based on two different methods: lattice-Boltzmann and finite-volume*. International Journal of Heat and Fluid Flow, 2000. **21**(2): p. 186-196.
 20. Smith, B.L., J.J. Stepan, and D.M. McEligot, *Velocity and pressure measurements along a row of confined cylinders*. Journal of Fluids Engineering, 2007. **129**(10): p. 1314-1327.
 21. Shen, L., E.-S. Chan, and P. Lin, *Calculation of hydrodynamic forces acting on a submerged moving object using immersed boundary method*. Computers & Fluids, 2009. **38**(3): p. 691-702.
 22. Turki, S., H. Abbassi, and S.B. Nasrallah, *Effect of the blockage ratio on the flow in a channel with a built-in square cylinder*. Computational Mechanics, 2003. **33**(1): p. 22-29.
 23. Sharma, A. and V. Eswaran, *Effect of channel confinement on the two-dimensional laminar flow and heat transfer across a square cylinder*. 2004.
 24. Sohankar, A. and A. Etminan, *Forced-convection heat transfer from tandem square cylinders in cross flow at low Reynolds numbers*. International Journal for Numerical Methods in Fluids, 2009. **60**(7): p. 733-751.
 25. Chatterjee, D. and S. Amiroudine, *Two-dimensional mixed convection heat transfer from confined tandem square cylinders in cross-flow at low Reynolds numbers*. International Communications in Heat and Mass Transfer, 2010. **37**(1): p. 7-16.

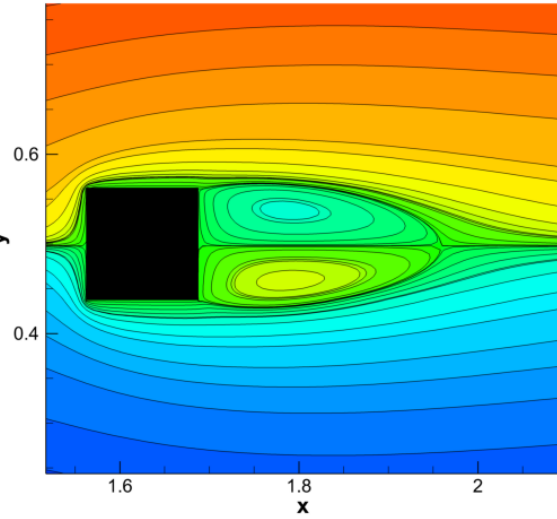
Appendix

A.1 Streamlines for different Reynolds number for square cylinder with blockage ratio of 12.5%

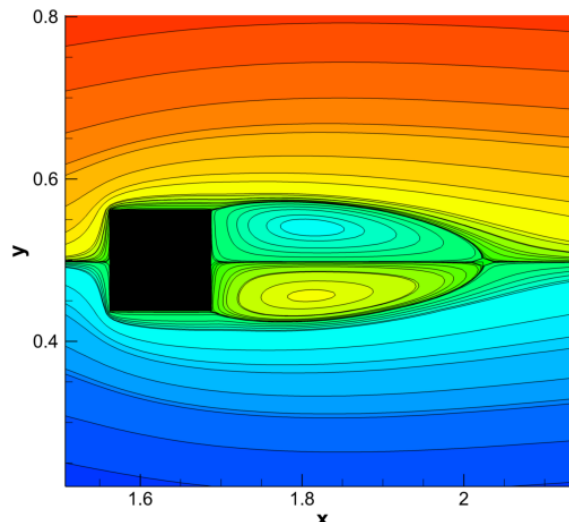




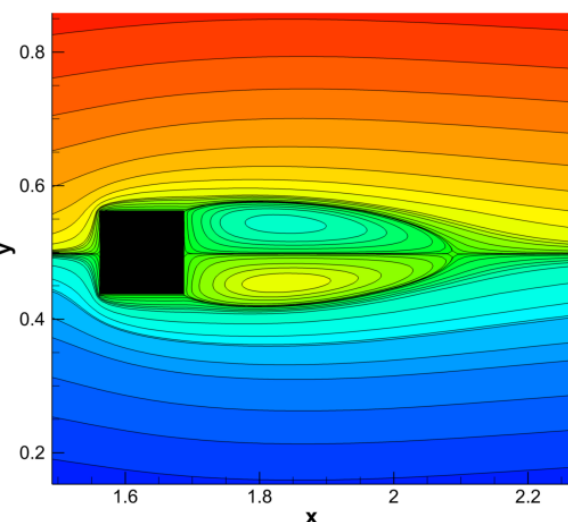
Re=30



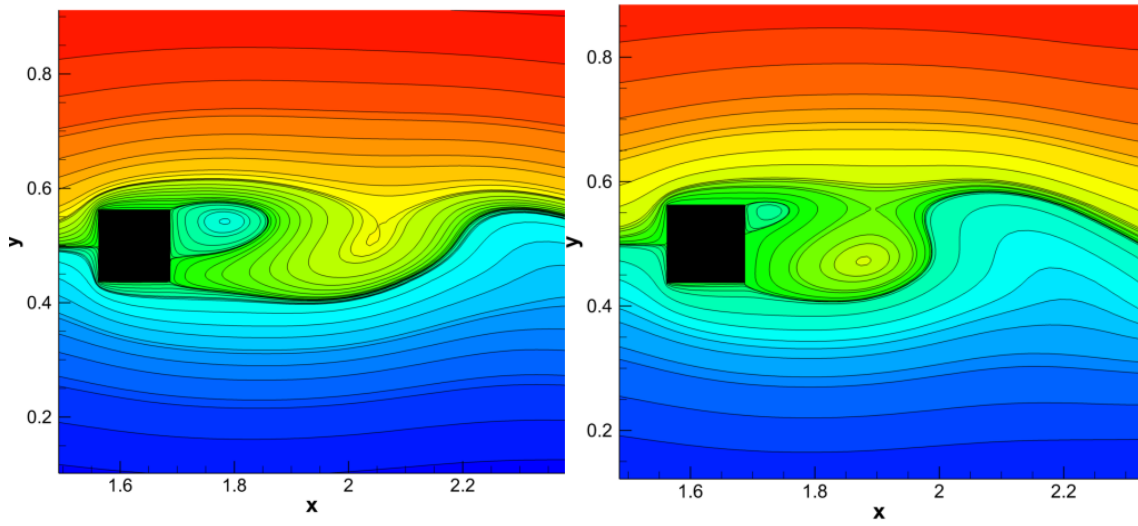
Re=40



Re=50

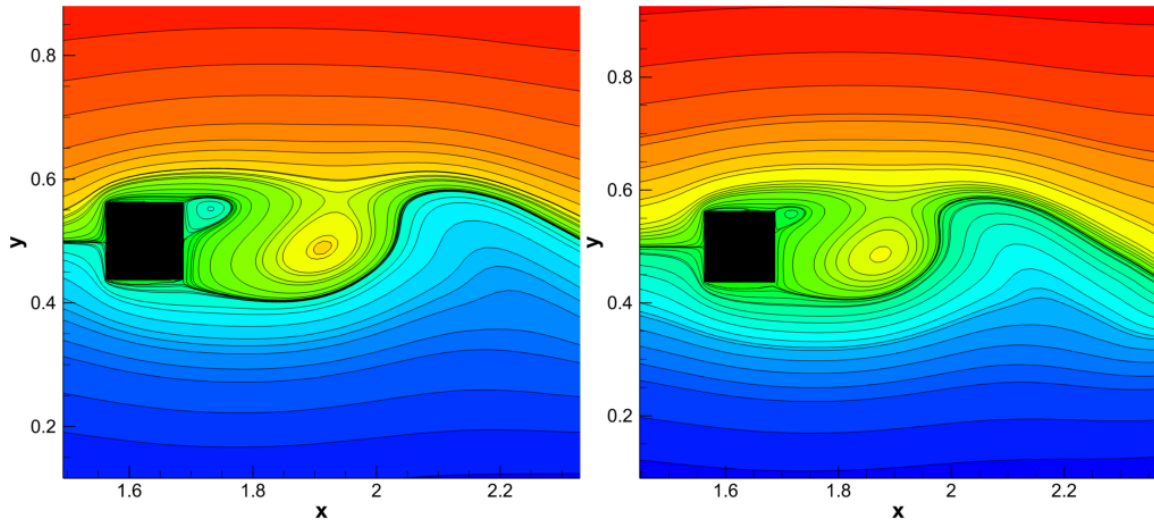


Re=60



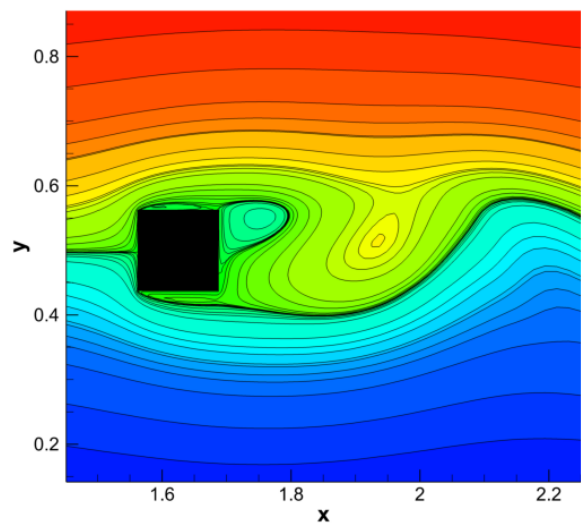
Re=70

Re=80

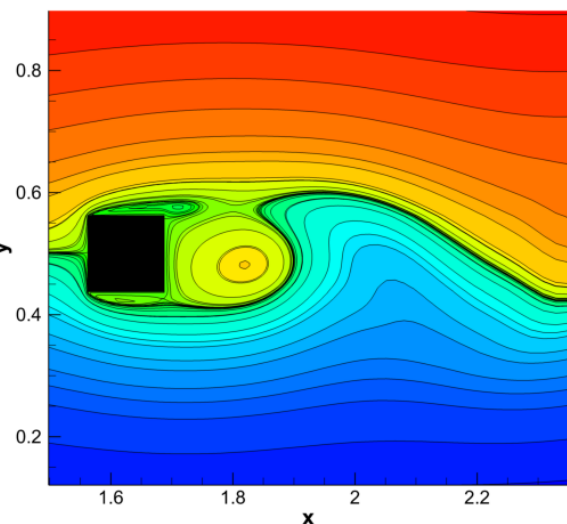


Re=100

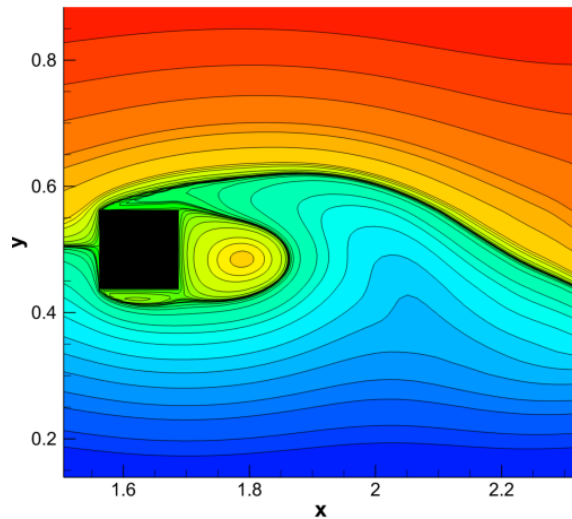
Re=120



Re=150



Re=180



Re=225

A.2 Result for effect of blockage ratio using coarser mesh

